Revealing Structure-Property Correlations in 2D Layered Materials Using Synergistic Combination of Electron Microscopy and Atomic-Scale Calculations

By

Junhao Lin

Dissertation

Submitted to the Faculty of the

Graduate School of Vanderbilt University

in partial fulfillment of the requirements

for the degree of

DOCTOR OF PHILOSOPHY

in

Physics

December, 2015

Nashville, Tennessee

Approved:

Prof. Sokrates T. Pantelides

Dr. Wu Zhou

Prof. Stephen J. Pennycook

Prof. Kirill I. Bolotin

Prof. Kálmán Varga

To my parents Yunxiang Lin (林允祥) and Bizhang Lin (林碧璋)

ACKNOWLEDGEMENTS

All the work would not be possible without the support from many people. I am grateful to my advisors, Prof. Sokrates T. Pantelides and Dr. Wu Zhou, who took me as a student and trained me in both theoretical calculations and electron microscopy. Their guidance, inspiration and advice are the most valuable gifts that I received in the training of PhD, and will continually benefit my future research career. I am also indebted to Prof. Stephen J. Pennycook, who gave me the chance to stay in the wonderful STEM group at Oak Ridge National Laboratory (ORNL) as a visiting student. The three year experience at ORNL working with numerous theorists and experimentalists was a precious memory in my life. I would also like to thank Prof. Kirill Bolotin and his student, Diraj Prasai, who taught me the sample preparation procedures on 2D materials and generously provided the lab facility for me to use. I also want to thank Prof. Kálmán Varga for his time serving as my PhD committee member and helpful advice.

I want to thank Dr. Ryo Ishikawa, Dr. Rohan Mishra, Dr. Juan Carlos Idrobo, Dr. Yuyang Zhang and Dr. Qian He at ORNL and Dr. Bin Wang, now at Oklahoma State University, for their frequent and helpful discussions where new ideas were generated. My special thanks go to Dr. Andrew R. Lupini, for his help in fixing the weird problems emerging on the microscopes and his patience and kindness in answering those "urgent" phone calls on the weekends. My PhD research would not be smooth and successful without interdisciplinary collaborations. I want to thank my collaborators, Mr. Yongji Gong and Dr. Ajayan Pulickel at Rice University, Mr. Xin Lu and Dr. Qihua Xiong at the National University of Singapore for their high quality samples, and Dr. Ovidiu Cretu and Dr. Kazu Suenaga at AIST-Japan for their amazing *in-situ* transport data in the

nanowire project. I also thank Dr. Jiaqiang Yan and Prof. David Mandrus at the University of Tennessee, Knoxville and Dr. Dave Caudel at Vanderbilt University for growing the bulk crystal used for the monolayer exfoliation. I also would like to thank Dr. Weidong He and Prof. James Dickerson for their supervision on nanoparticle synthesis during the first two years of my PhD study. Many thanks go to my dear friends in China and US.

At last, I want to express my deepest thanks to my family for their infinitive support during my PhD study oversea. Without their encouragement and tolerance, I would not have the courage to go through the whole PhD study. I want to thank them for their endless love without reserve, unconditional support for whatever decisions I made, and the willingness for offering me whatever they had.

TABLE OF CONTENTS

Page

LIST OF TABLES

Table Page

LIST OF FIGURES

Figure Page

CHAPTER I

INTRODUCTION TO THE SCANNING TRANSMISSION ELECTRON MICROSCOPE, DENSITY FUNCTIONAL THEORY AND 2D MATERIALS

It has been well-documented that the atomic structure, chemical composition and bonding of a material determine its physical properties [1-5]. Research in understanding the structure-property correlations in materials has been one of the main themes in condensed matter physics. Therefore, various techniques have been developed for characterizing the structure of materials. Recent developments in scanning transmission electron microscopes (STEMs) [6-8], especially the suceesfully realization of abberation correction [9], has enabled direct imaging of the atomic structure of a material at single-atom scale [10]. Combined with density funcitional theory (DFT), which enables first-principles atomic-scale calculations that can predict the ground state of a material with very high accuracy [11], the structure-property correlations in materials can now be understood at the atomic level. STEM and DFT are complementary to each other and the interplay of these two techniques serves as a powerful tool in material study. In this chapter, I will breifly review the principles of imaging in a STEM and some basic concepts in DFT. More details can be found in many well written text books that are cited in this chapter.

1.1 Scanning Transmission Electron Microscope

Similar to photons, when a beam of electrons strikes a material, the result is reflection, absorption and transmission, which depend on the electronic structure and thickness of the sample. Samples used in tranmission electron microscopes (TEMs) are usually very thin (several nanometers to several tens of nanometers) so that most of the incident electrons can tranmit through the sample and be collected by different detectors. The basic configuration of a TEM and scanning TEM (STEM) are provided in Fig. 1.1.

Traditional high-resolution TEM (HRTEM) uses a parallel illumination source to form images [12]. The transmitted and diffracted beams interfere with each other in either constructive or destructive ways which gives rise to the image intensity, as shown in Fig. 1.1 [13]. HRTEM imaging is also known as phase contrast imaging, where the intensity of the image depends on the contrast transfer function (CTF, $H(\mathbf{k}) = \sin \chi(\mathbf{k})$ where $\chi(\mathbf{k})$ is the abberation function) and defocus (defocus is the first-order term in the abberation function) [13]. In a given defocus, the image intensity oscillates between negative and positive values depending on the spatial frequecy $\mathbf{k}$. This feature makes HRTEM images hard to be interpreted. Therefore, simulations are always used to accompany HRTEM images to determine the accurate atomic structure of the material.

In contrast, a highly converged electron beam is used in a STEM to raster the sample pixel-by-pixel. The tiny electron probe interacts with the sample where the electrons remain undistributed or get scattered. The scattered electrons thus carry the structural and chemical information of the sample, which can be extracted via different detectors at the exit planes of the electrons. The scattered electrons have different angular distributions and are typically collected by detectors with annular shapes. Moreover, the center beam

(scattered angle <1˚) goes into the spectrometer which can be used to form electron energy loss spectrum (EELS) images.

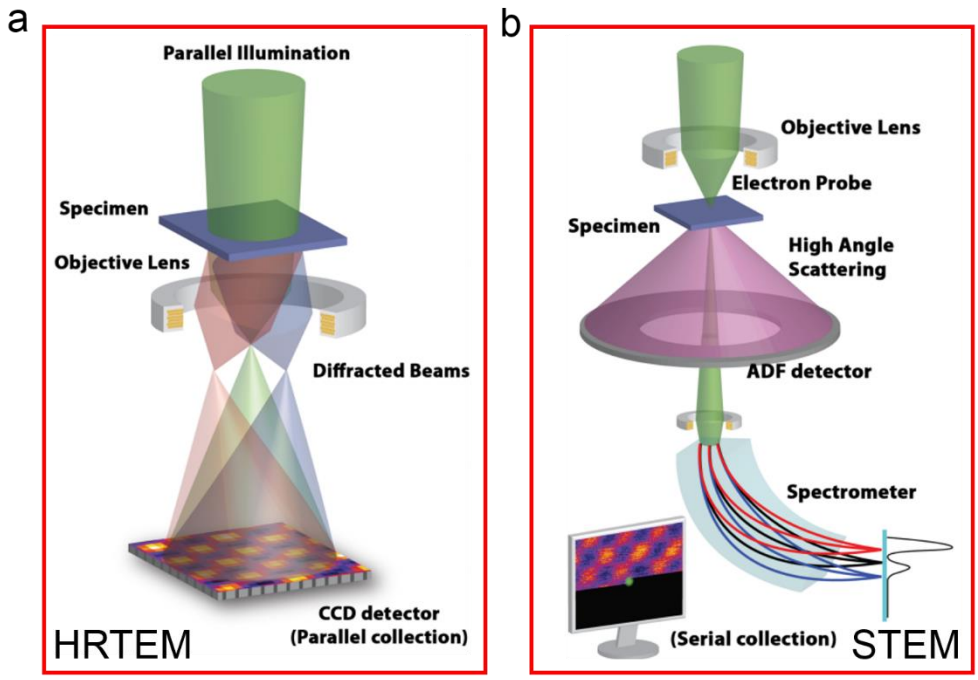

Figure 1.1: Comparison of the configuration of a TEM (a) and STEM (b). Adapted from Ref [14].

It is important to understand the elastic (also known as Rutherfold) and inelastic scattering when the electrons interact with the atoms in the sample. A schematic illustration of elastic scattering is provided in Fig. 1.2. When electrons travel through the electron cloud and approach the positively charge nucleus, they interact with the strong Coulomb potential from the nucleus which diverts their travelling paths. The kinetic energy of the electrons is conserved in this process. The Coulomb potential is strong enough to divert the electrons by a large angle from their original paths, even can revert their directions (back scattering electrons, BSE) [15]. Due to conservation of momentum, inelastic scatteing (eg., part of the energy from the incoming electron is lost to the

electrons around the nuclei) rarely occurs on electrons that are scattered into high angles. Thus, high-angle scattered electrons usually undergo elastic scattering. Moreover, it is straightforward to see that the heavier the atoms, the higher the propability that the electrons can be scattered into high angles due to the stronger Coulomb potential. Now it is easy to understand why STEM imaging using high-angle scattered electrons, i.e., HAADF-STEM imaging, is also called Z-contrast imaging, since the intensity of the images are directly related to the atomic number of the imaged species. Elastic scattering is the main source of the contrast in HRTEM and STEM images, and it also creates the intensity distribution in the diffraction patterns.

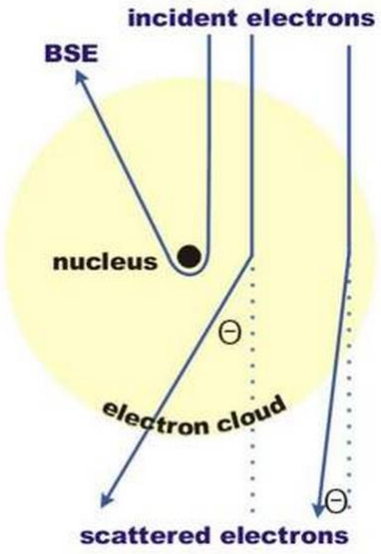

Figure 1.2: Schematic of the elastic scattering process of the incident electrons. Adapted from Ref [15].

Due to the wave nature of electrons, the distribution of the elastically scattered electrons form diffraction patterns and obey Bragg's law [16, 17]. We can simplify Bragg's law in the following statement: the difference of the scattered wave vector $\mathbf{k_n}$ and

the incident wave vector $\mathbf{k_0}$ has to be equal to a multiple of a reciprocal lattice vector $\mathbf{g}$ of the crystal:

$$\boldsymbol{k_n} - \boldsymbol{k_0} = \boldsymbol{n} \cdot \boldsymbol{g} \tag{1}$$

The reciprocal lattice vector $\mathbf{g}$ is determined by the lattice parameters of the sample in real space and varies along different orientations. Thus, the diffraction pattern records the structural information of the sample. Since a coherent covergent electron beam is used as the probe to illuminate the sample in STEM, the diffraction pattern is projected as disks. The contrast in a STEM image originates from the interference between these diffraction disks, as shown in Fig. 1.3a. An experimental image showing the interference of such diffraction disks is provided in Fig. 1.3b [18]. It is the inteference between the diffracted waves that gives the varying intensity across the STEM images. If one can collect a whole set of the diffraction disks during the scanning in a STEM, all sample infromation can be exctracted from this data set.

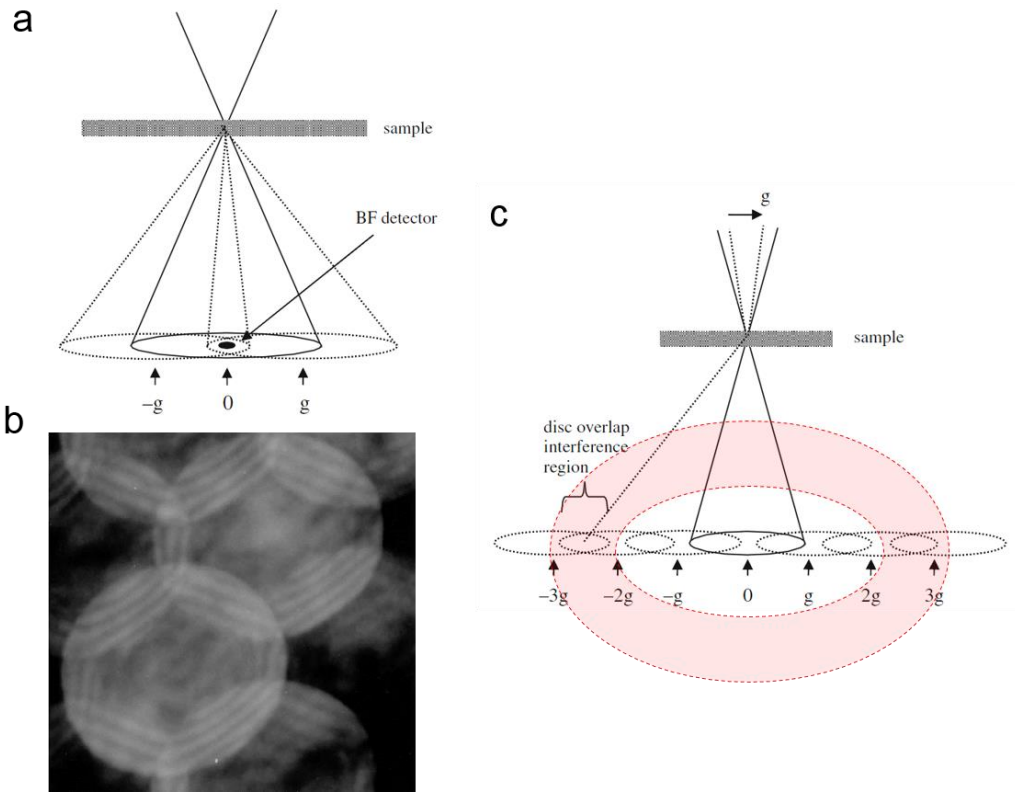

Figure 1.3: (a) Schematic of the overlapping between the diffracted beams. (b) Experimental image showing the interference between the diffraction disks. (c) Schematic showing the overlapping between diffraction disks for smaller lattice spacing (bigger reciprocal lattice vector). The red annular ring indicates the location of the integration region. Image adapted from Ref [18].

For smaller reciprocal lattice vectors **g** (large lattice spacing in the real space), the overlapping regions may consist of several diffraction disks. For simplicity, we consider a triple-overlapping model shown in Fig. 1.3a and just use these three beams to calculate the intensity behavior of the image. A detailed deduction of the intensity of the final image is available in the STEM text book written by Pennycook and Nellist [18]. Here we just show the key equations that demonstrate the concept of the process without any mathematical details.

We start with the wavefunction of electrons in quantum mechanics. One particular solution to the time-independent Schrödinger equation describing the wave nature of the electrons at the position of the front focal plane in reciprocal space is:

$$\varphi(\boldsymbol{K}) = C \cdot exp(i\boldsymbol{K} \cdot \boldsymbol{R}) \tag{2}$$

where C is the normalized constant, K is the wave vector and R is the coordinate of the particle in the 3D real space. The wavefront of the electron may be affected when the electrons travel through the aperature before reaching the sample. Moreover, abberation from the electronic lens also modifies the wave vector of the tavelling electrons. In order to incorporate both effects, we can write the wavefunction of the electron as:

$$T(\boldsymbol{K}) = A(\boldsymbol{K})exp[-i \cdot \chi(\boldsymbol{K})] \tag{3}$$

where A(**K**) sums up the contribution from the aperture, and χ(**K**) is the abberation function that affects the electron wave. The probe shape can now be described in real space by taking the inverse Fourier tranform of the wavefunction T(**K**):

$$P(\boldsymbol{R}) = \int T(\boldsymbol{K})\exp(i2\pi\boldsymbol{K} \cdot \boldsymbol{R})d\boldsymbol{K} \tag{4}$$

To indicate the scanning behavior of the probe, we can add a variable $\mathbf{R_0}$ in **R** to describe the electron wave behavior around the position $\mathbf{R_0}$:

$$P(\boldsymbol{R} - \boldsymbol{R_0}) = \int T(\boldsymbol{K})\exp[i2\pi\boldsymbol{K} \cdot (\boldsymbol{R} - \boldsymbol{R_0})]d\boldsymbol{K} \tag{5}$$

the next step is to decribe the interaction between the probe and the sample, i.e., electron diffraction in the sample. We can multiply a transmission function ϕ(R) to the probe to describe such interaction. Then the exit wavefunction has the general form:

$$\psi(\boldsymbol{R}, \boldsymbol{R_0}) = P(\boldsymbol{R} - \boldsymbol{R_0})\phi(\boldsymbol{R}) \tag{6}$$

since we are describing diffraction in the reciprocal plane, it is more convenient to convert the exit wavefunction back to reciprocal space by taking the Fourier transformation:

$$\psi(\boldsymbol{K}, \boldsymbol{R_0}) = \int P(\boldsymbol{R} - \boldsymbol{R_0})\phi(\boldsymbol{R})exp(-i2\pi \boldsymbol{K} \cdot \boldsymbol{R})\, d\boldsymbol{R} \tag{7}$$

finally, the above equation can be simplified into the following form:

$$\psi(\boldsymbol{K_f}, \boldsymbol{R_0}) = \int \phi(\boldsymbol{K_f} - \boldsymbol{K})T(\boldsymbol{K})\exp[-i2\pi \boldsymbol{K} \cdot \boldsymbol{R_0}]d\boldsymbol{K} \tag{8}$$

where $\mathbf{K_f}$ is the tranverse wave vector of the exit wave, **K** is the tranverse wave vector of each diffracted beams that is scattered to $\mathbf{K_f}$ in the diffraction plane. This gerneral equation describes that the final intensity at the point $\mathbf{R_0}$, corresponding to the tranverse wave vector $\mathbf{K_f}$, is the sum of all incident waves with wave vector **K** that are scattered by the sample to $\mathbf{K_f}$.

Now let us look at the simplest case which we only have three diffracted beams, as indicated in Fig.1.3. We are now calculating the point $\mathbf{R_0}$ corresponding to tranverse wave vector **K** with three diffraction disks located at 0, g and -g. Since there are only three diffraction disks, we can simplify the general equation from integral to addition:

$$\psi(\boldsymbol{K}, \boldsymbol{R_0}) = T(\boldsymbol{K})\exp[-i2\pi \boldsymbol{K} \cdot \boldsymbol{R_0}] + \phi_g T(\boldsymbol{K} - \boldsymbol{g})\exp[-i2\pi(\boldsymbol{K} - \boldsymbol{g}) \cdot \boldsymbol{R_0}] + \phi_{-g} T(\boldsymbol{K} + \boldsymbol{g})\exp[-i2\pi(\boldsymbol{K} + \boldsymbol{g}) \cdot \boldsymbol{R_0}] \tag{9}$$

Consider a simple case, K=0 (the center point), and neglect the aperature function, we get the expression of the intensity ($I=|\Psi|^2$) by assuming a weak-phase object [18]:

$$\phi_g = i\sigma V_g \tag{10}$$

$$I(\boldsymbol{R_0}) = 1 + 4\left|\sigma V_g\right| \cos\left(2\pi \boldsymbol{g} \cdot \boldsymbol{R_0} - \angle V_g\right) \sin\chi(\mathbf{g}) \tag{11}$$

Where $\angle V_g$ is the phase of the $\mathbf{g}^{\text{th}}$ Fourier component of the specimen potential. The interference between the diffraction disks contributes to the ocillation of the image

intensity indicated by the term of sinχ(**g**), where χ is the abberation function. This equation is similar to the CTF in phase contrast TEM imaging, whose standard form is H(**k**)=sinχ(**k**) [19, 20]. It is now obvious that if a small detector is used to form STEM images (only three interefered beams in this case), the image is coherent. This is also called bright-field (BF) imaging in STEM.

From the above concepts, it is now easy to understand the resolution limit in STEM imaging. The maximum resolution in STEM is defined by minmum overlap interference regions between two nearby diffraction disks (depends on reciprocal lattice vector **g**) which can form an image, as shown in Fig. 1.3c. If the reciprocal lattice vector **g** is too large (very small lattice spacing) that no diffraction disks overlap, no contrast can be obtained in the final image.

Coherent BF imaging in STEM is still not directly interpretable. Now consider the general case which uses the signals over the entire diffraction plane, as shown in Fig. 1.3c. For simplicity, we neglect the thermal vibration of the lattice so that all the diffraction disks are stable and have fixed locations. The deduction starts from taking the squared modulus of the general equation to get the intensity at each point $\mathbf{K_f}$, then integrate all the points with a detector function:

$$I(\boldsymbol{R_0}) = \int D_{detector}(\boldsymbol{K_f}) \times \left| \int \phi\left(\boldsymbol{K_f} - \boldsymbol{K}\right) T(\boldsymbol{K}) \exp(-i2\pi \boldsymbol{K} \cdot \boldsymbol{R_0}) d\boldsymbol{K} \right|^2 d\boldsymbol{K_f} \quad (12)$$

The detailed process of the deduction can be found in [18]. The final intensity at the position $\mathbf{R_0}$ is then written as:

$$I(\boldsymbol{R_0}) = |\psi(\boldsymbol{R_0})|^2 \otimes O(\boldsymbol{R_0}) \quad (13)$$

this is the definition of incoherent imaging, where the image intensity can be separated into two parts: the probe and the object function (determined by sample). The probe

function is the modulus of the electron wavefunction, which is a real-positive function without oscillating between the positive and negative values. Moreover, the image intensity can be interpreted as the convolution between them, both of which are functions of the probe position. This is called annular dark field (ADF) imaging.

The above theory suggests that ADF imaging can be regarded as incoherent imaging only if all electrons arriving at the detector are summed over. However, summing all electrons at the detectors results in no image contrast [21, 22]. To bring in image contrast, we can not use all the electrons but only part of them in an annular region of the diffraction plane, in which the signal is integrated inside this region, as indicated in Fig. 1.3c. In other words, a hole is needed inside the detector. The hole has an important parameter k_{inner} (the spatial frequency corresponding to the inner radius of the annular ring), and it can change the object function sustantially (detailed deduction can be found in [23]):

$$O(\boldsymbol{R_0}) = \int_{half\ plane} \frac{J_1(2\pi k_{inner}|\boldsymbol{R}|)}{2\pi|\boldsymbol{R}|} \times \left[\sigma V\left(\boldsymbol{R_0} + \frac{\boldsymbol{R}}{2}\right) - \sigma V\left(\boldsymbol{R_0} - \frac{\boldsymbol{R}}{2}\right)\right]^2 d\boldsymbol{R} \qquad (14)$$

where J_1 () is the first-order Bessel function of its first kind. The above mathematical description can be understood in a simple way: the integration of the annular ring region over the diffraction plane introduces a coherence envelope function (J_1) over the original object function. The width of this coherence envelope function is determined by the inner radius (k_{inner}) of the annular ring. The coherence envlope should modulate an optimized region of the scattering potential so that atoms in the sample is suffciently included inside the envelope while breaking the inter-atom coherence. In other words, if the envolope is too narrow, i.e., the hole is too large, to include enough variation of the scattering potential, the object function would be modulated within a small region and thus no

image contrast. However, if the envelope is too broad, i.e., the hole is too small, such that it includes the scattering potential of more than one atom in the sample, the obejective function may include coherence between atoms. Therefore, depending on the value of inner collection angle of the annular detector, the STEM image can either be partially coherent or incoherent [24].

On the other hand, inelastic scattering is more like an "absorption" effect [25]. Electrons can transfer a critical amount of energy to electrons in the electron cloud around the atom, leading to the electron being excited to an unoccupied state above the Fermi level [26]. Such process can occur to the weakly-bound and inner-shell electrons. Therefore, the incident electrons lose energy, i.e., the kinetic energy is not conserved. This energy transition process has bigger probability to happen when the direction of the wave vector of the incident electron is preserved. Therefore, low-angle electron scattering (scattered angle <1˚) is mostly inelastic. Moreover, the left-over hole, which comes from the exicitation of the inner shell electrons, can be filled up by another electron in a higher energy state. The relaxation of this process leads to the emission of element-specific characteristic X-rays or Auger electrons. The energy transferred to the inner shell electrons of the atom leads to an ionization energy edge in the EELS. Different element maintains distinct shape and onset energy of the ionization. Therefore, EELS can be used to distinguish the chemical identity of a sample with unknown chemical composition, as will be discussed later.

The electron gun is the source that generates electrons. Modern HRTEM and STEM equipped with a cold field emission gun which provides highly coherent electrons with less energy spread and three orders of magnitude more current than a conventional

thermionic filament. The specific working principle of field emission electrons can be found in the text book [13]. The gun is under ultra-high vacuum (typically 10^{-12} Torr), which is isolated from the main chamber of the microscope by the gun valve. After being extracted and accelerated, the electrons go through various electronic lenses (electromagnetic coils). A basic TEM usually consists of a condenser, objective and projector lenses for magnifying and demagnifying the electron beam in different stages [13]. These lenses mainly have two physical effects on the electrons: electromagenetic and electrostatic field that exert forces on the electrons, which manipulate their motions, such as deflecting the electrons to certain angle.

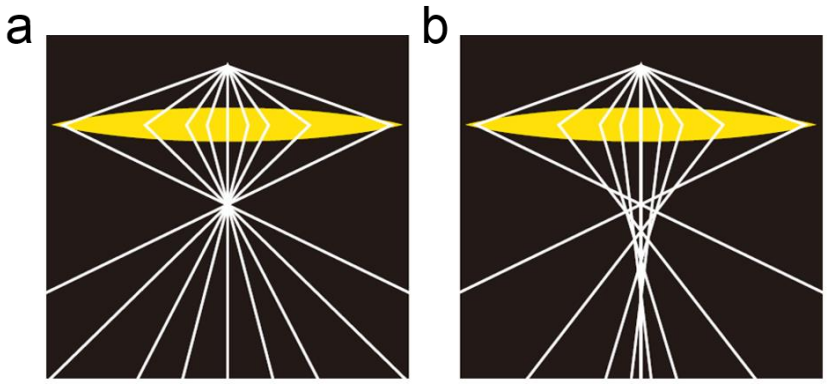

Figure 1.4: The convergence of rays in ideal lens (a) and realistic lens (b). The rays do not meet at the focal point after the lens, broadening the size of the focal spot. Image adapted from Ref [27].

The spatial resoltion in a STEM depends on how tiny the probe can be converged, since the abberation function is all included in the probe intensity function [10, 28], as described previously. Therefore, abberation in STEM is corrected before the converged beam hits the sample, which is dramatically different from TEM. In ideal optical electronic systems, all incident beams passing through the electron lens (similar as lens in the optical microscope which divert the rays) can be converged into a single point.

However, the electron beam that travels through the edge of the lens may be deflected more severely than the one through the center due to the imperfectness of the realistic coils, i.e., the beams do not meet in the focal point after the lens, as shown in Fig. 1.4. This is commonly known as spherical abberations which limits the probe size, making the spatial resolution far below the diffraction limit [9]. This effect can be seen clearly when the object of interest is underfocus or overfocus in the Ronchigram (a shadow image of the sample under a stationary converged beam [29]), where the image is distorted severely away from the center, as shown in Fig. 1.5. Before the invention of spherical abberation corrector, raising the acceleration voltage was a feasible way to shape the probe into smaller size. Nevertheless, it requires more sophisicated experimental setup and the large knock-on damage from the high-energy electrons limits the material systems that can be investigated.

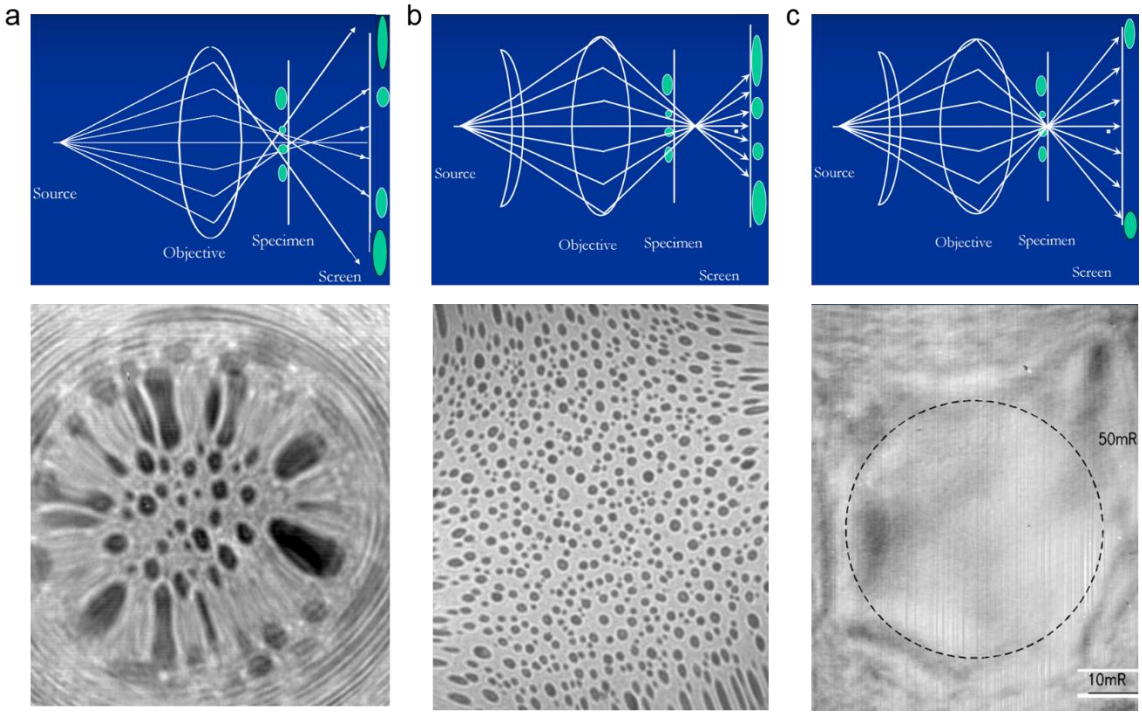

Figure 1.5: Schematic of Rochigram of Au nanoparticles illuminated by uncorrected electron beam underfocus (a) and corrected electron beam overfocus (b). Experimental

images are shown below. The imaged nanoparticles in (a) are elongated from their original sizes. (c) Rochigram of the same area when the defocus is zero. The magnification is infinite at the center. The size of the infinite region is an indication to the aperture size that we can open up. Image adapted from Ref [30].

Putting a small aperature after the lens is the simplest way to reduce spherical abberiation because it can block most of the beams that are deflected in high angles. However, the small aperature has a side effect to the probe: it reduces the intensity of the electron beam which lowers the signal-to-noise ratio in the formation of images, and also enlarges the Airy pattern which introduces a large probe tail. To open up the aperture, the nature of the abberation needs to be understood, where quantitative mathematical description of abberation is needed. Let us first look at a simple 1D model to quantify how much the abberated wave deviates from its ideal position. A schematic is shown in Fig. 1.6 [31].

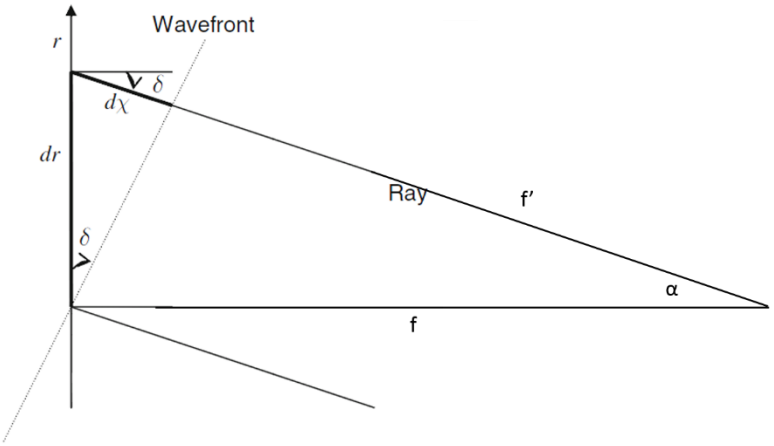

Figure 1.6: Schematic showing the difference between the spherical and abberated wavefront in 1D. Image adapted from Ref [31].

We define the distance from the focal point to the wavefront as **f**. Since we are dealing with rays that are near the focal point, **α** is a very small angle and f is approximately equal to **f'**. Then we can approximate **r** by:

$$r = f' \cdot sin\alpha \approx f \cdot \alpha \tag{15}$$

In order to get the relationship between the ideal spherical and abberated wavefront, we need to know the relationship between α and the difference angle δ. It is clearly from the schematic that sinδ is equal to dx/dr. Since δ is also a small angle, we can approximate δ as:

$$\delta(\alpha) \approx sin\delta = \frac{dx}{dr} = \frac{dx}{f \cdot d\alpha} \tag{16}$$

In conventional textbooks, the deflection distance x is expanded as power series as a function of α. Since δ should have mirror symmetry with α (the sign of α did not change δ), we can write the expanded series without the odd terms:

$$x(\alpha) = \frac{1}{2}C_1\alpha^2 + \frac{1}{4}C_3\alpha^4 + \frac{1}{6}C_5\alpha^6 + \frac{1}{8}C_7\alpha^8 + \cdots \tag{17}$$

Thus, the final relationship which decribes how much angle the path of the ray deviates from the ideal spherical wavefront as a function of α is:

$$\delta(\alpha) = C_1\alpha^1 + C_3\alpha^3 + C_5\alpha^5 + C_7\alpha^7 + \cdots \tag{18}$$

all the coefficients, including the focal length **f**, are merged into a single term in the above equation for simplicity. This is a simplified relationship of the spherical and abberated wavefront in 1D form. Since α is small, the lower order, such as the first and third order, have the most impact to the overall abberation in the system. The abberation function thus describes a set of plane waves whose phase is modified, which can now be taken into the mathematical desription of the plane waves. A more general mathematical expression of the abberation function is give as follows [32]:

$$\chi = \frac{2\pi}{\lambda} r = \pi \delta f \lambda \boldsymbol{K}^2 + \frac{\pi}{2} C_3 \lambda^3 \boldsymbol{K}^4 + \frac{\pi}{3} C_5 \lambda^5 \boldsymbol{K}^6 + \frac{\pi}{4} C_7 \lambda^7 \boldsymbol{K}^8 + \cdots \quad (19)$$

Such function describes the total phase error of the plane waves in reciprocal space in terms of the transverse wave vector **K,** which is induced by the imperfectness of the lens.

The abberation in the electron wave can now be expressed quantitatively. The best way to correct the abberation is to contrallably introduce a lens system that can counteract the coefficients in the abberation function. However, Scherzer has demonstrated that for all round lenses, the higher order coefficients, except defocus, are positive [31]. Negative coefficients can only be achieved by sets of non-rotationally symmetric lenses, such as the combination of quadrupoles, hexapoles and octopoles. This is the foundation of all abberation correctors nowadays.

After figuring out how to introduce negative terms in the abberation function, the next step is to measure the exact aberration of the electron waves in the microscope. This becomes possible only when fast computers and charge-coupled-devices (CCD) are equipped along with the microscope, since the measurements need iterative feedback and real-time diagnosis. Commercialized aberration correction technqiues are now available from Nion Co. and Corrected Electron Optical Systems (CEOS), respectively [33-35], who use different algorithms for aberration diagnosis and corrector configurations. The aberration diagnosis algorithm developed by Nion Co. relies on the analysis of the Ronchigram images, which fits the entire aberration function in an individual diagnosis.

As demonstrated before, aberration leads to heterogeneous magnification across the Ronchigram images, which are directly related to the coefficients in the aberration function. The algorithm developed by Nion Co. divides the Ronchigram into a square grid, and determines the local magnification of each segement in the Ronchigram grid by

cross-correlating a set of images taken by shifting the electron beam to an known amount of distance. The shifting distance is determined by the defocus value. All the coefficients in the abberation function can then be fitted based on the map of the magnification. The working flow of this algorithm follows iteration between diagnosis and correction, until the final measured abberation coefficients reach to desired value. The detail of the fitting algorithm can be found in the text book [23].

One of the advantages in STEM is the parallel collection of the elastic electrons for imaging the atomic structure and inelastic electrons for probing the electronic structure of the material, which is complementary to each other [36, 37]. EELS also benefits from abberation correction in STEM, since the smaller electron probe gives higher spatial resolution in spectrum imaging. Because EELS collects the penetrating electrons that excite the weakly-bonded and inner-shell electrons of the atoms, atom-resovled EEL spectrum can also be used to probe the bonding conditions and chemical enviroment of atoms being imaged. Since EELS is not extensively used in this thesis, other thorough review of EELS can be found in [18, 25, 38].

1.2 Density Functional Theory

The behavior of all particles (electrons, photons, etc) can be described by quantum mechanics. The essence of quantum mechanics is Schrödinger's equation, which describes the temporal evolution of the quantum states of a physical system [39]:

$$i\hbar\frac{\partial}{\partial t}\Psi(\mathbf{r},t) = \hat{H}\Psi(\mathbf{r},t) \tag{20}$$

where $\Psi(\mathbf{r}, t)$ is the wavefunction of the system, and $\hat{H}$ is the Hamiltonian of the physical system.

In calculations of the optimized atomic structure of the material, we generally consider that the structure is not changing with time, i.e., the Hamiltonian does not contain time-dependence. However, excited states are involved for most optical and transport properties of the materials, where the Hamiltonian of the system is time-dependent. Such topic is beyond the scope of this thesis, and I will only review the principles of DFT for atomic structural calculations in their ground state (the possible lowest energy state of a material).

Therefore, if considering the Hamiltonian of the system is time-independent, the time-independent Schrödinger's equation can be extracted:

$$\widehat{H}\Psi(\mathbf{r}) = E\Psi(\mathbf{r}) \tag{21}$$

where E is the eigenvalue (energy) of the Hamiltonian for the state described by wavefunction Ψ(r, t). For a single particle, the Hamiltonian only consists of kinetic and potential energy, which reads:

$$\widehat{H} = -\frac{\hbar^2}{2m}\nabla^2 + V(r) \tag{22}$$

The potential energy is normally described by Coulomb potential in a charged particle system, like atoms. For example, a hydrogen atom consist of an electron and a proton, which are negatively and positively charged, respectively. In a crystal that contains many atoms, we need to assign coordinates for each charged particle, and consider the Coulomb potential between them. The Hamiltonian and wavefunction becomes:

$$\widehat{H}_{many-body}\Psi(\mathbf{r_1}, \mathbf{r_2}, \cdots \mathbf{r_N}) = -\frac{\hbar^2}{2m}\sum^N {\nabla_r}^2\Psi(\mathbf{r_1}, \mathbf{r_2}, \cdots \mathbf{r_N}) +$$

$$\sum_{i=1}^{N}\sum_{j=1}^{N}\frac{Z_i Z_j}{|\mathbf{r}_i - \mathbf{r}_j|}\Psi(\mathbf{r_1}, \mathbf{r_2}, \cdots \mathbf{r_N}) \tag{23}$$

where $\Psi(\mathbf{r_1}, \mathbf{r_2}, \mathbf{r_3}\ldots)$ is the many-body wavefunction that describes the position of each charged particle, Z is the charge of each charged particle in the system.

The above many-body Hamiltonian is too complicated to be solved explicitly, except for the simple case like H or He that contain only a few charged particles. Assumptions are made to simplify the Hamiltonian to reduce the calculations without losing accuracy. The first attempt is called Born-Oppenheimer (BO) approximation. It is proposed based on the fact that the nucleus is much more massive than electrons, where the nucleus can be treated as "frozen" during the movement of the electrons. As a result, solving the Hamiltonian can be divided into two steps in the framework of BO approximation: (1) calculate the wavefunction that only depends on the coordinates of electrons (fixed coordinates of nucleus); (2) the calculated electronic wavefunction can then serve as a potential in the Schrödinger's equation containing only the nuclei. Therefore, the first step of the BO approximation can be written as:

$$\widehat{H}_{BO} = -\frac{\hbar^2}{2m_e}\nabla^2 + \frac{1}{4\pi\epsilon_0}\sum_{i=1}^{N_e}\sum_{j=i+1}^{N_e}\frac{e^2}{|\mathbf{r_i}-\mathbf{r_j}|} + \sum_{i=1}^{N_e}\sum_{k=1}^{N_i}\frac{eZ_k}{|\mathbf{r_i}-\mathbf{R_k}|} + \sum_{k=1}^{N_i}\sum_{l=k+1}^{N_i}\frac{Z_kZ_l}{|\mathbf{R_k}-\mathbf{R_l}|} \tag{24}$$

where the ion-ion interaction term is considered as a constant when sovling this Hamiltonian. The BO approximation significantly reduces the variables in the wavefunction, however, still far beyond the realistic computational capability that we can handle.

Based on the BO approximation, another assumption is proposed which is called Hartree approximation. In Hatree approximation, the many-body wavefunction of electrons is written as a linear combination of orthonormal single particle wavefunctions:

$$\Psi(\mathbf{r_1}, \mathbf{r_2}, \mathbf{r_3}\cdots) = \psi_1(\mathbf{r_1})\psi_2(\mathbf{r_2})\psi_3(\mathbf{r_3})\cdots \tag{25}$$

The physical meaning of the above equation is that electron correlation is neglected in order to simplify the calculation. Substituting the above wavefunction back into the Schrödinger's equation with BO Hamiltonian gives the Hartree equations:

$$\sum_i^N \hat{H}_i \, \Psi(\mathbf{r_1}, \mathbf{r_2}, \mathbf{r_3} \cdots) = \sum_i^N \varepsilon_i \, \Psi(\mathbf{r_1}, \mathbf{r_2}, \mathbf{r_3} \cdots) \tag{26}$$

where the Hamiltonian for the i[th] electron can be seperated from the above equation and written individually:

$$\left[-\frac{\hbar^2}{2m_e}\nabla^2 + {V_i}^H(\mathbf{r_i}) + V_{ions}(\mathbf{r_i})\right]\psi_i(\mathbf{r_i}) = \varepsilon_i \psi_i(\mathbf{r_i}) \tag{27}$$

$${V_i}^H(\mathbf{r_i}) = \sum_{i \neq j}^N \left\langle \psi_j \left| \frac{e^2}{|\mathbf{r_i} - \mathbf{r_j}|} \right| \psi_i \right\rangle \tag{28}$$

where the V_i^H is called the Hartree potential of the electrons.

The Hartree approximation breaks down the many-body wavefunction into a single-particle-like problem. However, the Hartree approximation ignores the fermionic nature of electrons, whose wavefunction is antisymmetric when exchanging the position of any two electrons in the system. A correction to the Hartree approximation is to write the many-body wavefunction as a determinant rather than a product of single particle wavefunctions. Such correction is called Hartree-Fock approximation:

$$\Psi(\mathbf{r_1}, \mathbf{r_2}, \mathbf{r_3} \cdots) = \begin{vmatrix} \psi_1(\mathbf{r_1}) & \cdots & \psi_1(\mathbf{r_N}) \\ \vdots & \ddots & \vdots \\ \psi_i(\mathbf{r_1}) & \cdots & \psi_N(\mathbf{r_N}) \end{vmatrix} \tag{29}$$

which gives the Hartree-Fock equations:

$$\left[-\frac{\hbar^2}{2m_e}\nabla^2 + {V_i}^H(\mathbf{r_i}) + V_{ions}(\mathbf{r_i})\right]\psi_i(\mathbf{r_i}) - \sum_{i \neq j}^N \left\langle \psi_j \left| \frac{e^2}{|\mathbf{r_i} - \mathbf{r_j}|} \right| \psi_i \right\rangle \psi_j = \varepsilon_i \psi_i(\mathbf{r_i}) \tag{30}$$

Even though the Hartree-Fock approximation has significantly reduced the calculational effort of the BO Hamiltonian and accurately describes the fermionic nature

of the electrons, it is still not practical to handle a system that includes several tens of electrons.

The Hartree-Fock approximation scales poorly due to the complexity of the wavefunction. For instance, in order to describe a system that has N electrons, 3N spatial coordiates in the wavefunction need to be calculated. If the necessary variables that describe the system can be reduced, the efficiency of the calculations may improve. DFT is a method of this kind. The essential concept in DFT is to work with the electron density n(**r**) instead of the wavefunction Ψ(**r**$_1$**,** **r**$_2$**,** **…r**$_N$) to describe the ground state of the system, which effectively reduces the calculated variables from 3N to 3.

The first fundamental concept in DFT is known as the Hohenberg-Kohn (H-K) theorem. The H-K theorem defines an energy functional for the ground state of a many-electron system and proves that the correct ground-state electron density n(**r**) uniquely minimizes this energy functional for given external potential [1]. The proof of this theorem is surprisingly simple. In the BO approximation, we have separated the Hamiltonian into electron-electron, ion-electron, ion-ion interactions. Since the ions are fixed in the BO approximation, the ion-electron and ion-ion interaction can be considered as an external potential that depends on the ion coordinates. The equation can be written as follow:

$$\hat{H}_{BO}\Psi(\mathbf{r_1}, \mathbf{r_2}, \cdots, \mathbf{r_N}) = \left[\hat{T} + \hat{U} + \hat{V}\right]\Psi(\mathbf{r_1}, \mathbf{r_2}, \cdots, \mathbf{r_N}) = E\Psi(\mathbf{r_1}, \mathbf{r_2}, \cdots, \mathbf{r_N}) \qquad (31)$$

where $\hat{T}$ is the operator for kinetic energy, $\hat{U}$ is the electron-electron interaction and V is the potential energy from the external field. The operators $\hat{T}$ and $\hat{U}$ are universal since they are the same for every system that have N electrons, while $\hat{V}$ depends on the system,

i.e., the locations of the positive charge nucleus. Now we define the electron density n(**r**) as:

$$n(\mathbf{r}) = N \int \Psi^*(\mathbf{r}, \mathbf{r_2}, \cdots, \mathbf{r_N}) \Psi(\mathbf{r}, \mathbf{r_2}, \cdots, \mathbf{r_N}) \, \mathrm{d}\mathbf{r_2} \cdots \mathrm{d}\mathbf{r_N} \tag{32}$$

Assume there is a ground state wavefunction Ψ_1 which corresponds to a ground state energy E_1 for a specific external potential $V_1(\mathbf{r})$:

$$E_1 = \langle \Psi_1 | \hat{H}_1 | \Psi_1 \rangle = \int V_1(\mathbf{r}) n(\mathbf{r}) d\mathbf{r} + \langle \Psi_1 | \hat{T} + \hat{U} | \Psi_1 \rangle \tag{33}$$

To verfify the H-K theorem, suppose that there is another external potential $V_2(\mathbf{r})$ not equal to $V_1(\mathbf{r})$ with a different ground state wavefunction as Ψ_2. The integration of such wavefunction also generates the same electron density n(**r**). Then we can write:

$$E_2 = \langle \Psi_2 | \hat{H}_2 | \Psi_2 \rangle = \int V_2(\mathbf{r}) n(\mathbf{r}) d\mathbf{r} + \langle \Psi_2 | \hat{T} + \hat{U} | \Psi_2 \rangle \tag{34}$$

Aussming non-degenerate wavefunctions, the Rayleigh-Ritz theorem suggests that the energy will be higher if the wavefunction used to sandwitch the Hamiltonian operator is not the ground state wavefunction. Thus we have:

$$E_1 < \langle \Psi_2 | \hat{H}_1 | \Psi_2 \rangle = \int V_1(\mathbf{r}) n(\mathbf{r}) d\mathbf{r} + \langle \Psi_2 | \hat{T} + \hat{U} | \Psi_2 \rangle = E_2 + \int [V_1(\mathbf{r}) - V_2(\mathbf{r})] n(\mathbf{r}) d\mathbf{r} \tag{35}$$

and similarly,

$$E_2 < \langle \Psi_1 | \hat{H}_2 | \Psi_1 \rangle = \int V_2(\mathbf{r}) n(\mathbf{r}) d\mathbf{r} + \langle \Psi_1 | \hat{T} + \hat{U} | \Psi_1 \rangle = E_1 + \int [V_2(\mathbf{r}) - V_1(\mathbf{r})] n(\mathbf{r}) d\mathbf{r} \tag{36}$$

adding these two equation on both side, we get:

$$E_1 + E_2 < E_2 + E_1 \tag{37}$$

which is a contradictory statement. Therefore, the assumption that different external potential $V_1(\mathbf{r})$ and $V_2(\mathbf{r})$ can give the same electron density is not valid. This proves that the electron density is uniquely determined by the external potential. That is said, given a

specific external potential, there is only one correct solution of the electron density that correponds to the ground state of the system.

It is important to realize why the above theorem can reduce the calculations. The previous effort in finding the ground state of the system can be summarized as finding the correct ground state wavefunction that has the mininum energy to the Hamiltonion:

$$E_{ground-state} = min\{\langle\Psi|\hat{H}|\Psi\rangle\} \tag{38}$$

since we have defined the electron density as the integration of the wavefunction, the above equation can be written as:

$$E_{ground-state} = min\{\int V_1(\mathbf{r})n(\mathbf{r})d\mathbf{r} + \langle\Psi|\hat{T} + \hat{U}|\Psi\rangle\} \tag{39}$$

since $\hat{T}$ and $\hat{U}$ are universal operators, we can define a universal functional as a function of the electron density to desribe the contribution from these two operators, without knowing any information from the external potential V(**r**):

$$F[n(\mathbf{r})] = \langle\Psi|\hat{T} + \hat{U}|\Psi\rangle \tag{40}$$

thus the energy of the ground state reads as:

$$E_{ground-state} = min\{E[n(\mathbf{r})]\} = min\{\int V_1(\mathbf{r})n(\mathbf{r})d\mathbf{r} + F[n(\mathbf{r})]\} \tag{41}$$

the ground state energy now becomes a function of the electron density. The above equation implies that, if the univeral functional F[n(**r**)] can be found and written without any input from the wavefunction, one can find the ground state of the system without knowing its exact many-body wavefunction! In other words, we have shifted the problem from solving for a complicated wavefunction with 3N coordinates to searching for the electron density with only 3 coordinates for a N-electron system.

Since the operators $\hat{T}$ and $\hat{U}$ are universal in the functional F[n(**r**)], i.e., it is not related to the actual configuration of the system, an auxillary system consisting of

fictitious non-interacting particles moving in an effective potential can be used to reproduce F[n(**r**)] in the real many-body system. Kohn and Sham have made a further step in working out the F[n(**r**)] [2], which is known as the Kohn-Sham equations. They start with defining F[n(**r**)] as:

$$F[n(\mathbf{r})] = T_s[\mathbf{r}] + \frac{e^2}{2}\int \frac{n(\mathbf{r})n(\mathbf{r}')}{|n(\mathbf{r})|} d\mathbf{r}d\mathbf{r}' + E_{xc}[n(\mathbf{r})] \tag{42}$$

where

$$T_s[\mathbf{r}] = \sum_i \left\langle \psi_i \middle| -\frac{\hbar^2}{2m_e}\nabla^2 \middle| \psi_i \right\rangle \tag{43}$$

T_s is the kinetic energy of the single particle, ψ_i is the wavefunction for individual particles, and the $E_{xc}[n(\mathbf{r})]$ is called the exchange-correlation energy functional. To find the electron density that gives the minimun total energy, they use the Euler-Lagrange equations with the constraint that the total number of the electrons is a constant:

$$\delta E[\tilde{n}(\mathbf{r})] = \int \delta\tilde{n}(\mathbf{r}) \left\{ V_{eff}(\mathbf{r}) + \frac{\delta}{\delta\tilde{n}(\mathbf{r})} T_s[\tilde{n}(\mathbf{r})]\Big|_{\tilde{n}(\mathbf{r})=n(\mathbf{r})} - \epsilon \right\} d\mathbf{r} = 0 \tag{44}$$

where

$$V_{eff}(\mathbf{r}) = V(r) + \int \frac{n(\mathbf{r}')}{|\mathbf{r}-\mathbf{r}'|} d\mathbf{r}' + V_{xc} \tag{45}$$

and the exchange-correlation potential

$$V_{xc} = \frac{\delta E_{xc}[n(\mathbf{r})]}{\delta n(\mathbf{r})} \tag{46}$$

Kohn and Sham found that the solution of the above Euler-Lagrange equation can be obtained by self-consistently solving the single particle equations

$$\left[-\frac{\hbar^2}{2m_e}\nabla^2 + + V_{eff}(\mathbf{r}) \right] \psi_i(\mathbf{r}) = \varepsilon_i \psi_i(\mathbf{r}) \tag{47}$$

with

$$n(\mathbf{r}) = \sum_{j=1}^{N} \left| \psi_j(\mathbf{r}) \right|^2 \tag{48}$$

These equations are the Kohn-Sham equations. In order to solve the Kohn-Sham equations, one still needs approximations on one or more terms in these equations. These approximations becomes different subjects in the development of DFT, producing fruitful choice of parameters in DFT calculations optimized for different systems. For instance, they are:

(1) How to approximate the exchange-correlation functional $E_{xc}[n(\mathbf{r})]$?

(2) What basis sets are used for the single particle wavefunction $\psi_i(\mathbf{r})$?

For the first question, since little is known on the exact form of the exchange-correlation functional E_{xc} for many systems of interest, we can only approximate the functional and assume that it has similar form to some well-known system. Among all, the simplest system where the functional can be calculated accurately is the homogeneous electron gas. The first approximation proposed by Kohn and Sham is the so-called local density approximation (LDA). In LDA, the exchange-correlation energy per electron is purely local and equal to an electron in a homogeneous electron gas with the same density. The interaction of electrons should be nonlocal, but LDA works very well for the weakly correlated materials and the exact reason still remains debatable [40]. Another approximation which is slightly less local is called generalized-gradient approximation (GGA). GGA considers the electron density and its gradients for the exchange-correlation energy. Readers can find the details in the review article for different approximation of the exchange-correlation energy [41].

However, both LDA and GGA fail dramatically in describing the ground state properties of strong-correlated material systems which is featured by a more pronounced localization of electrons. The exchange-correlation term is supposed to include all the

corrections needed to recover the many-body terms of electronic interactions. Nevertheless, it is intrinsically difficult to model the exact electron density dependence in the exchange-correlation term. LDA and GGA generally provide a poor representation of the many-body feature in the exchange-correlation functional, therefore lead to problematic predictions in correlated systems whose physical properties are often controlled by the many-body terms. Paradigmatic expamples of problematic systems are Mott insulators, whose electronic localization is missed by the approximation in LDA or GGA, leading to a wrong prediction that these materials are metallic. To correct the lack of the many-body representation in the exchange-correlated functional, LDA+U is developed, which is based on a corrective functional inspired by the Hubbard model. The idea of LDA+U is to use the Hubbard model to describe the "strongly correlated" electronic states of a system (typically, localized *d* or *f* orbitals), while the rest of valence electrons are treated at the level of "standard" DFT functionals. The total energy of a system under the framework of LDA+U can be written as:

$$E_{LDA+U}[n(r)] = E_{LDA}[n(r)] + E_{Hub}[\{n^{I\sigma}_{mm'}\}] - E_{dc}[\{n^{I\sigma}\}] \quad (49)$$

where the E_{LDA} term represents the DFT total energy functional, E_{Hub} is the term that contains the Hubbard Hamiltonian to model the correlated states, and E_{dc} is the "double counting" term which models the contribution of correlated electrons to the DFT energy as a mean-field approximation of E_{Hub}, which is used to eliminate the possible repeating part of energy from correlated electrons in the E_{LDA} term. Unfortunately, the E_{dc} term is not uniquely defined, and different formulations have been implemented and used in various circumstances. The results of the LDA+U method is sensitive to the numerical value of the effective on-site electronic interactions. Therefore, the Hubbard U functional

do not have a universal value and should be recomputed each time if the materials being investigated have changed. In-depth review of LDA+U can be found in Ref [42].

Another commonly known issue when using LDA approximation in DFT calculations is called “bandgap disaster”, i.e., LDA tends to underestimate the bandgap value compared to experiments. GW approximation gives more accurate description of the electronic band structure, which models the quasi particle energies (electron addition and removal) by the poles of the one-particle interacting Green’s function within the many body perturbation theory. However, due to the higher computational complexity of the theoretical framework of GW approximation, the time cost in GW calculations is much larger than standard DFT calculations, which limit its use in supercell calculations that consists of thousands of electrons [43].

For the second question, plane waves are frequently used as the basis set for approching the single particle wavefunction $\psi_i(\mathbf{r})$ in crystal. From Bloch’s theorem, the wavefunction can be expanded as a sum of plane waves:

$$\psi_i(\mathbf{r}) = \sum_{\mathbf{G}} c_{i,k+\mathbf{G}} \exp(i(\mathbf{k}+\mathbf{G})\cdot\mathbf{r}) \tag{50}$$

where **G** is the reciprocal lattice vector of the crystal. Plane waves are a complete set which can accurately decribe the wavefunction. However, the above expansion includes an infinite number of plane waves, but in reality we can only process the sum of finite plane waves. Therefore, a concept called “energy cut-off” is used in DFT calculations, in which the sum over **G** can be truncated at specific “energy” threshold but still provide adequate representation of the cell-periodic part of the wavefunction. The higher the energy cut-off, the more accurate the calculations is.

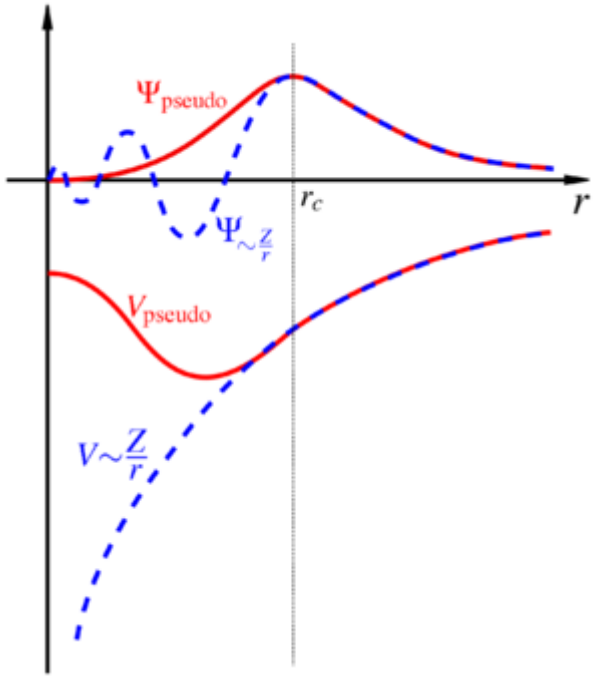

Figure 1.7: Schematic of the pesudopotential with a cut-off radius $\mathbf{r_c}$. Image adapted from Ref [44].

Another important concept is the pesudopotential when using the plane waves as the basis set. When approaching the nuclei of an atom, the Coulomb potential dramatically increases since it is inversely proportional to the distance **r**. Such change tends to make the wavefunction oscillate rapidly when it reaches the core electrons, as indicated in Fig. 1.7. The oscillation is difficult to be represented by the sum of the plane wave set. Since most of the bonding and chemical properties are related to the valence electrons rather than core electrons, the Coulomb potential from the core electrons can be modified in order to generate a smooth function for wavefunciton expansion under the plane wave set. The pesudopotential refers to a Coulomb potential that is matched with the full ionic potential outside a cut-off radius $\mathbf{r_c}$, and generate a smooth wavefuction inside that radius.

By using the pesudopotential, the calculation can be converged using a lower energy cut-off, which improves the efficiency of the DFT.

1.3 Introduction to 2D Materials

Are layered materials stable in their monolayer form? This is highly debatable before the successful demonstration of graphene in 2004, which is fabricated from mechanical exfoliation of its bulk form, graphite, via the "magic" scotch-tape method. After the discovery of graphene, more and more 2D materials are found through exfoliation from the bulk materials and chemical synthesis. Generally, 2D materials refer to layered materials in their single layer form, which maintain emerging physical properties different from their bulk due to the reduced interlayer screening. So far, a wide spread of novel physical properties are found in the family of 2D materials [45]. Figure 1.8 summarizes the current existing 2D materials and highlights their stability in ambient condition.

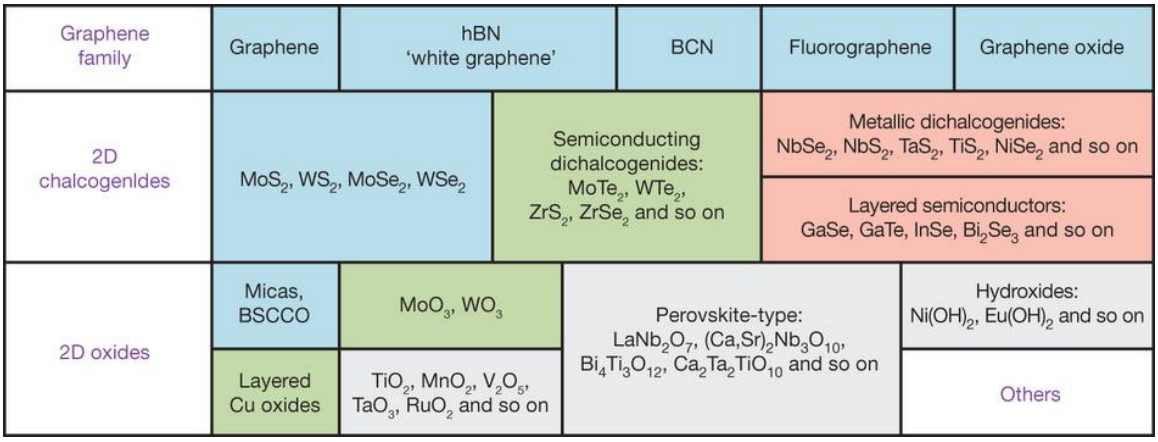

Figure 1.8: The family of the existing 2D materials. Blue-shaded, green-shaded and red-shaded blocks refer to the 2D materials that are stable, may stable and not stable in ambient condition. The grey-shaded blocks indicate 3D compounds that have been successfully exfoliated down to monolayers. Image adapted from Ref [45].

Extensive research interest in 2D materials begins with the successful exfoliation and identification of graphene on specific substrate [46]. The facile scotch-tape exfoliation method has provided a universal means to generate monolayer materials from their bulk form, facilitating and nourishing the extensive researches in every aspects of 2D materials. Among all 2D materials, graphene attracts tremendous attention. It is a unique carbon allotrope featuring a one-atom thickness. All carbon atoms sit in a honeycomb lattice and each atom bonds covalently to the nearest three neighbors in the plane to form a sp^2 structure. The remaining outer shell electron sits in the out-of-plane p_z orbital. Due to this special two-dimensional hexagonal structure, all p_z orbitals from the carbon atoms hybridize to form π and π^* bands, with crossings at two points (K and K`) of the Brillouin zone [47-50] (Fig. 1.9), which are called Dirac points. Therefore, graphene is a gapless semi-metallic material with a linear dispersion relation close to the Dirac point. Such electronic structure is a consequence of the symmetry between the sublattices and the hybridization of the p_z orbitals. The unique electronic structure of graphene is beneficial to electron transport, giving rise to interesting phenomena such as massless electrons near the Dirac point, ultrahigh electron mobility [51], and half-integer quantum Hall effect [52].

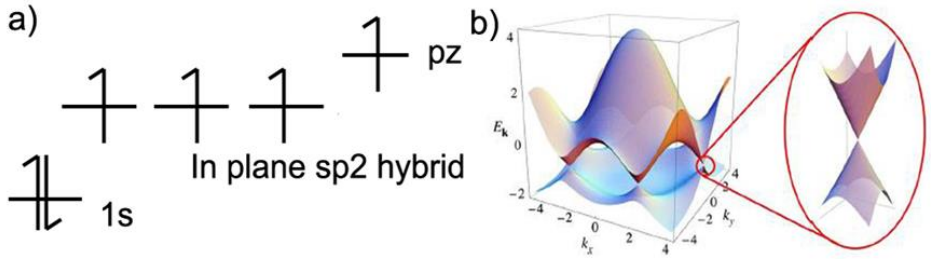

Figure 1.9: (a) A graph representing all orbitals of an individual carbon atom in graphene. (b) Electronic dispersion in the honeycomb lattice. Left: energy spectrum. Right: zoom in of the energy bands close to one of the Dirac points. Image adapted from Ref [50].

Besides graphene, another type of representative 2D materials are transition metal dichalcogenides (TMDs), which attracts tremendous attention for their unique optical and electronic properties [53]. Their monolayer forms are dramatically different from the bulk due to the quantum confinement effects [54-56]. For instance, bulk MoS_2 (a representative material in the family of TMDs) has an indirect band gap of 1.2 eV [57] whereas monolayer MoS_2 possesses a direct band gap of 1.8 eV [56, 58]. The attractive physical properties, including strong mechanical strength, high mobility and the lack of short channel effect in silicon field effect transistors (FET), make 2D TMDs a promising material for future electronic, optical and flexible devices. Current study has already demonstrates that FETs based on atomically thin MoS_2 exhibit high on/off ratio of $\sim 10^8$, steep subthreshold swing of ~70 $mv*dec^{-1}$ and carrier mobility of 1 – 480 $cm^2V^{-1}S^{-1}$ depending on the device configuration and dielectric environment [59]. High performance planar photodetectors are also demonstrated in monolayer MoS_2, with a photoresponsivity up to 840 AW^{-1} [60]. Additionally, monolayer TMDs can also be used for valley-electronics due to their broken inversion symmetry, which results in strong coupling of spin and valley degree of freedom [61]. Research interest is now focus on the TMDs heterostructures, in which different TMD layers are stacked vertically or interconnected laterally to achieve designed physical properties.

Due to the promising applications in 2D materials, it is essential to investigate the fundamental physics inside them. As mentioned in the beginning of this chapter, the structure and property in a material are strongly correlated. In the following chapters, I will show how to combine the STEM imaging with quantitative analysis and DFT calculations to investigate the atomic structures of various defects inside different 2D

materials, including their dynamical behaviors, and their effects to the properties of the original crystal.

CHAPTER II

AC/AB STACKING BOUNDARIES IN BILAYER GRAPHENE

Bernal stacked bilayer graphene (BLG) has been the subject of extensive research because of its tunable bandgap and promising application in optoelectronics and nanoelectronics [62, 63]. Besides the well-studied grain boundaries in each graphene layer, which have been shown to affect the mechanical properties and transport performance of monolayer graphene [64-67], unique stacking boundaries can be present in Bernal stacked BLG at the interfaces of domains with the same crystal orientation but different stacking, *i.e.* AB and AC stacking. Here, the terms AB and AC stacking refer to the shifting of one of the graphene layers to two opposite directions 1/3 of the way along the [1, 1] crystallographic vector, respectively, as schematically shown in Figure 2.1.

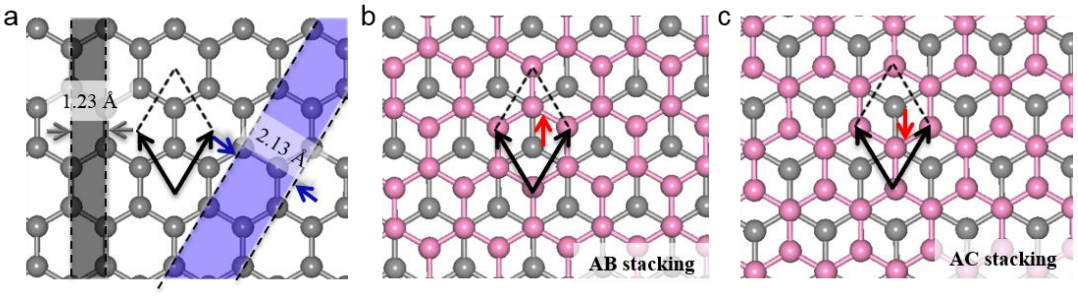

Figure 2.1: Schematic of AB and AC stackings in BLG. (a) Schematic of different lattice periodicities in monolayer graphene. (b, c) Schematics of AB stacking and AC stacking, respectively. The second layers are colored in pink. The dashed diamonds indicate the unit cells and black arrows are the unit cell vectors. The red arrow indicates the geometrical shift of the second layer with respect to the first layer.

Evidence for the co-existence of domains with mirrored AB and AC stackings was reported recently in BLG synthesized via silicon carbide (SiC) thermal decomposition

and chemical vapor deposition (CVD) growth [67, 68]. However, unlike grain boundaries, the presence of stacking boundaries in BLG does not seem to cause severe degradation of the transport performance of BLG-based devices [63, 69, 70]. Moreover, the detailed structure of such stacking boundaries has not been investigated. In particular, it is not known if the stacking boundaries are atomically sharp like grain boundaries. As an important step to reveal the contribution of the stacking boundaries to the properties of BLG, visualizing the morphology and identifying the atomic structure of these unique boundaries is necessary.

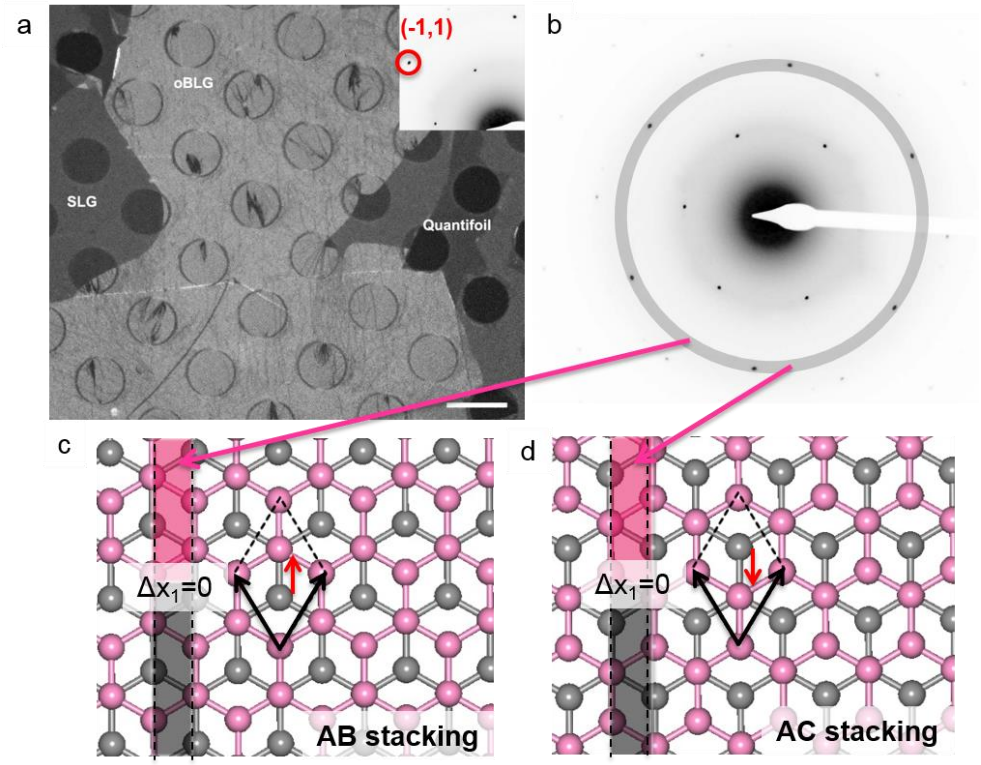

Figure 2.2: DF-TEM images of the stacking boundaries in oBLG. (a) DF-TEM image of a large flake of oBLG, acquired using the second order diffraction spot (-1,1) (red circle) at zero tilt. (b) Electron diffraction pattern of the oBLG region. Second order spots are highlighted by a gray ring. (c, d) Schematic of the lattice periodicity of the second order diffraction spots in oBLG. The pink strips indicate the lattice periodicity of 1.23 Å for the second layer, which is overlapped with the gray strip (lattice periodicity of 1.23 Å for first layer). Scale bars: 2 μm.

In order to identify the AB/AC stacking boundaries, I firstly performed tilted DF-TEM experiments [13] on high quality BLG grown on Cu foil via an optimized CVD method [71]. The sample was prepared by Fang in Massachusetts Institute of Technology. This experiment was performed on a FEI Tecnai 20T operated at 80 kV. No significant damage was observed on the bilayer graphene under this voltage. The DF-TEM images were recorded using specific diffraction spot which was picked out using the objective aperture, with a recording time of 60s -120s for each image.

A large flake of oriented bilayer graphene (oBLG) with a size over 10 μm is shown in Figure 2.2a. This image was taken using the second order diffraction spot (-1, 1), where AB and AC stacking had equivalent intensity regardless of tilting. The relationship between the DF-TEM image intensity and the tilting angle will be discussed later. The relative AB and AC stacking domains in this region are revealed by tilted DF-TEM images acquired using the first-order diffraction spot (0, 1) (Figure. 2.3a and 2.3b), based on their mirror-symmetrical intensity variations during tilting [67]. For better visibility, the AB and AC stacking domains were false-colored and reconstructed into a single image (Figure 2.3c). Noticeably, areas with densely packed AB and AC stacking domains can often be observed, as highlighted by the red rectangles.

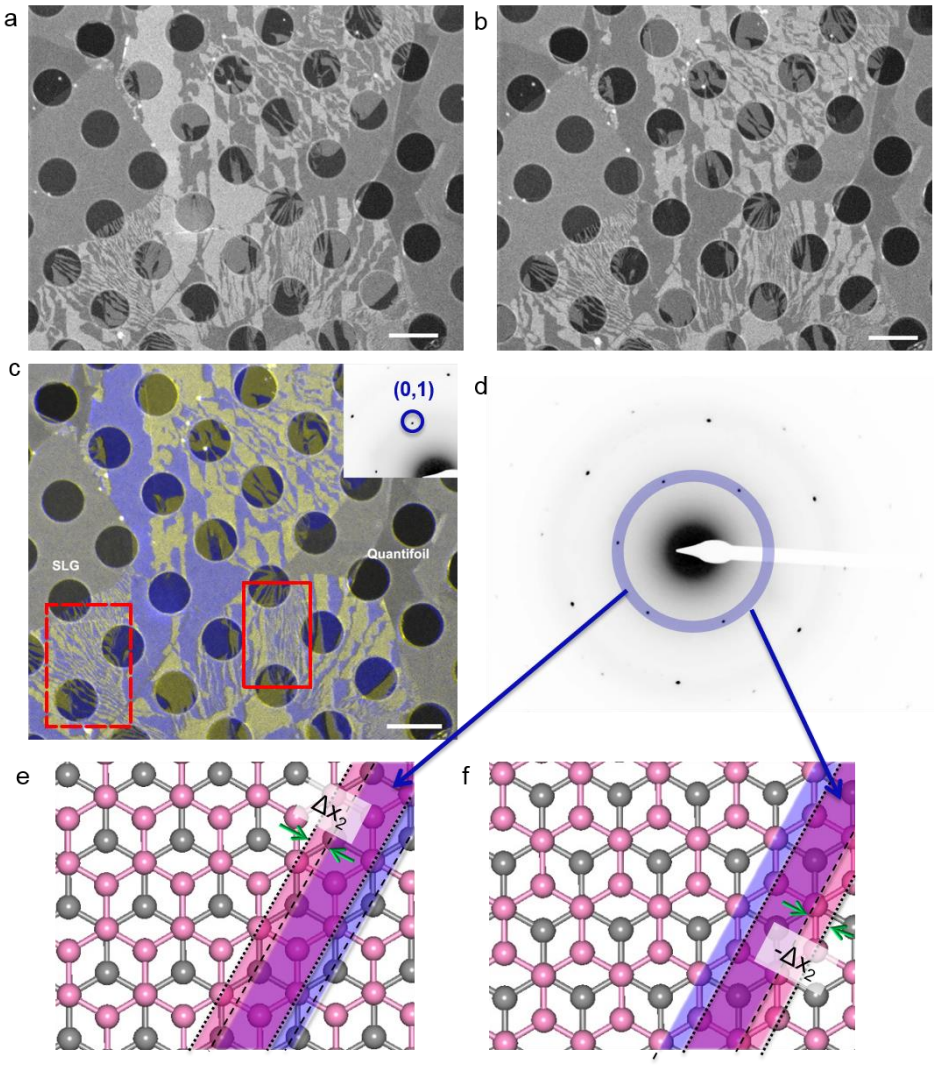

Figure 2.3: Highly-concentrated stacking boundaries in oBLG. DF-TEM images of the same oBLG flake using diffraction spot (0, 1) acquired at 10˚ (a) and -10˚ (b) tilting. (c) False color mapping of AB and AC stacking domains. The regions with highly-concentrated AB/AC stacking boundaries are highlighted by the red dashed rectangles. (d) Electron diffraction pattern of the oBLG region. First order diffraction spots are highlighted by the blue ring. (e, f) Schematic of the origin of mirrored intensity variation of AB/AC stacking domains during tilting. The blue strips in (e, f) indicate the lattice periodicity of 2.13 Å for the first layer while the pink ones are for the second layer. The relative shift Δx_2 is anti-symmetric in AB (e) and AC stacking (f) at zero tilt. Scale bars: 2 μm.

For perfect AB (or AC) stacking, a relative shift of Δx_2 between the two layers is induced for the 2.13 Å lattice periodicity (*i.e.* the first order diffraction peaks, blue rings,

Figure 2.3d), while no relative shift is present ($\Delta x_1 = 0$) for the 1.23 Å lattice periodicity (*i.e.* the second order diffraction peaks, gray circle, Figure 2.2b) during tilting. When tilted along the 2.13 Å lattice periodicity, the relative shift Δx_2 decreases for AB stacking (Figure 2.3e) but increases for AC stacking (Figure 2.3f), and vice versa, giving rise to the anti-symmetric intensity variation for AB and AC stackings during tilted DF-TEM imaging acquired using the first order diffraction peaks.

Magnified views of a selected oBLG region of Figure 3.2a are shown in Figure 2.4, where the relative AB and AC stacking domains obtained via tilted DF-TEM imaging are shown in Figure 2.4b and 2.4c. These ordered stacking domains are typically micrometer-long strips with widths of a few tens to a few hundred nanometers. Using the second order diffraction spot (-1,1), the boundaries between domains appear as dark lines in the DF-TEM image acquired at zero tilt (Figure 2.4a), while the AB and AC stacking regions are bright and indistinguishable under this imaging condition. The contrast indicates a decrease of the (-1, 1) diffraction intensity at the boundary regions as compared to ordered AB/AC stacking regions. The widths of the stacking boundaries are measured to be ~8 nm from the DF-TEM images (Figure 2e), suggesting the possible presence of nm-wide transition regions between the two stacking domains. Further, I notice that the stacking boundaries have overall random orientations and display a wide range of image contrast with some being darker than others, indicating that the stacking boundaries may have diverse morphologies depending on their precise formation conditions. These dark lines are absent in monolayer regions.

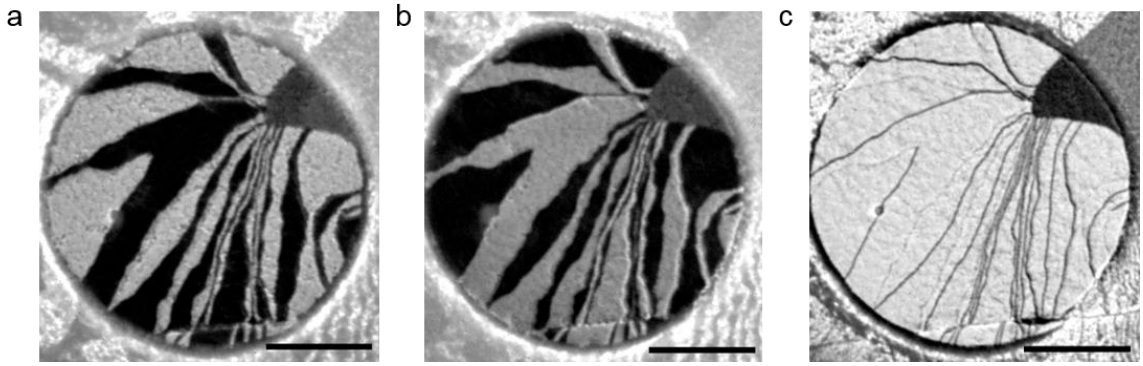

Figure 2.4: Higher magnification DF-TEM images of the stacking boundaries, acquired using diffraction spot (0, 1) at 10˚ (a) and -10˚ (b) tilt, and using diffraction spot (-1,1) at zero tilt (c). The boundaries between AB and AC stacking domains appear as dark lines in Figure c. Scale bars: 0.5 μm.

The structure-induced intensity decrease at stacking boundaries in DF-TEM images can be explained through the interference of the diffracted electron beam when transmitting through the BLG. DF-TEM images are formed by specific scattered electrons; therefore, the behavior of the image intensity mainly depends on the diffraction peak being used, corresponding to a specific lattice periodicity. The first- and second-order diffraction peaks for monolayer graphene correspond to lattice periodicities of 2.13 Å (Figure 2.3d) and 1.23 Å (Figure 2.2b), respectively, as schematically shown in Figure 2.1a. For oBLG where the two layers adopt the same crystal orientation, the diffraction from each layer interferes with each other. Therefore, the DF-TEM image intensity is controlled by the phase difference between the electron waves scattered by the two layers (or in other words, the relative shift of the lattice periodicity between the two layers) [13]. For example, the mirrored intensity variation of AB and AC stacking (Figure 2.4a & 2.4b) is due to the anti-symmetrical phase factor generated by the opposite relative shift of the 2.13 Å lattice periodicity during tilting.

For perfect AB and AC stackings, the interference of electrons scattered by the 1.23 Å lattice periodicities from both layers is fully constructive (Δx_1=0, see Figure 2.2c and 2.2d), making them indistinguishable in the DF-TEM image shown in Figure 2.2e. The reduced image contrast at the stacking boundaries (dark lines in Figure 2.2a), thus, indicates a phase difference (*i.e.* a non-zero Δx_1) at these transition regions. This phase shift could in principle be induced by: i) reconstruction along the AB and AC stacking domains due to the presence of sharp stacking boundaries; or ii) a continuous relative shift between the two layers by straining one of the two layers, as will be discussed. Furthermore, the variation in image contrast (Figure 2.4c) for the stacking boundaries suggests that different amount of shifts in lattice periodicity (Δx_1) can be present between the two layers at the transition regions, leading to different morphologies.

In order to resolve which of these two different classes of boundary accounts for the DF-TEM contrast, I further investigated the atomic structure of stacking boundaries using annular dark-field (ADF) imaging on an aberration-corrected Nion UltraSTEM^{tm} 100 operated at 60 kV [72]. The ADF images can be approximately interpreted as the convolution of the projected atomic positions in both graphene layers and the small electron probe. Figure 2.5b shows a Fourier filtered ADF image for a perfect AB stacking domain, with half of the carbon atoms overlapped. The brighter spots are the overlapping sites of two carbon atoms, illustrated by the atomic model shown in the upper inset. The lower inset of Figure 2.5b shows a simulated STEM image for perfect AB stacking which reproduces the regular pattern observed experimentally.

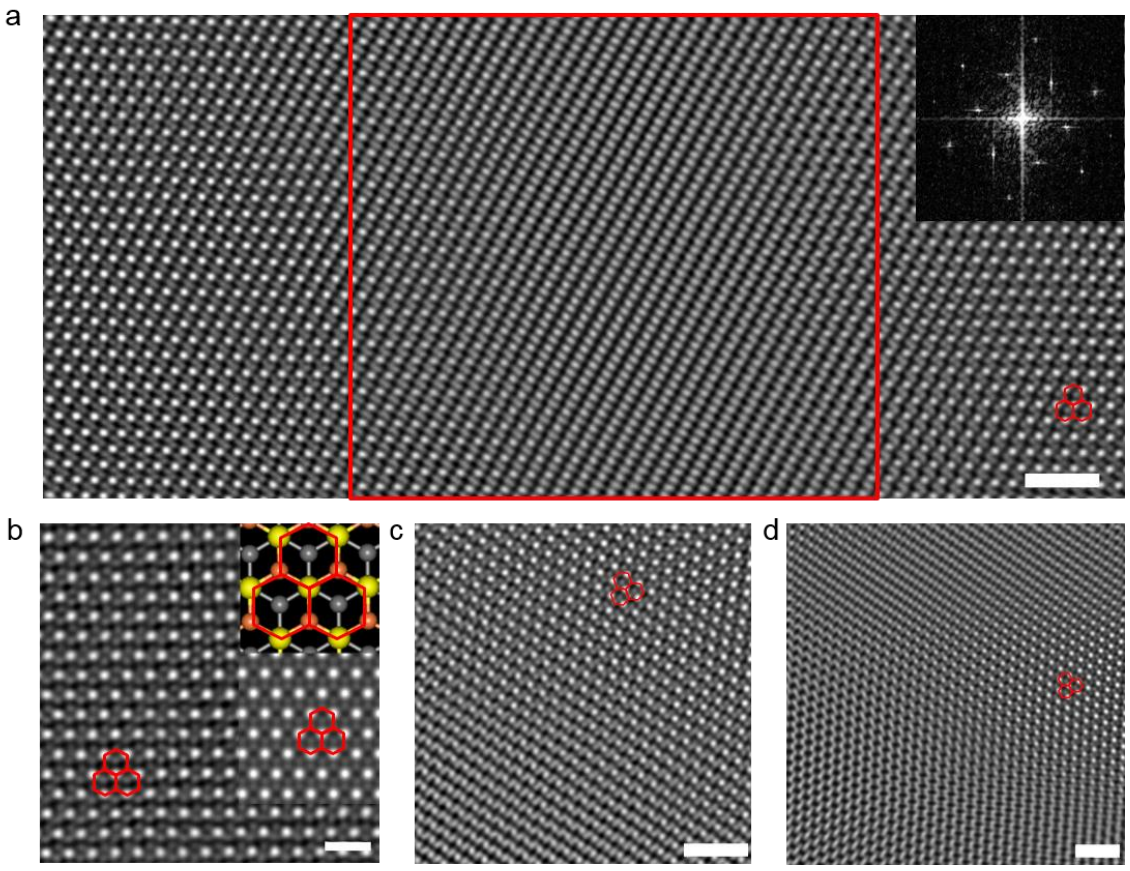

Figure 2.5: Atomic-resolution STEM-ADF imaging of stacking boundaries. (a) ADF image of a stacking boundary showing a full transition from AB to AC stacking. The transition region is highlighted by the red rectangle. Inset: FFT of the image. (b) ADF image of perfect AB stacking. Bright spots are the results of overlapping of two carbon atoms. Upper inset: Structural model of perfect AB stacking. The first layer is colored in gray and second in orange. The overlapping sites are highlighted by yellow. Lower inset: Simulated STEM image for perfect AB stacking. (c, d) ADF images showing irregular wiggle-like patterns (c) and square-like patterns (d) at the transition regions of stacking boundaries. Red hexagons represent the orientation of the graphene lattice in the AB stacking regions. Scale bars: 1 nm.

Besides the regular hexagonal AB (or AC) stacking pattern, irregular Moiré patterns are always observed at the transition regions of the stacking boundary. Figure 2.5a shows a Fourier filtered ADF image of a stacking boundary. AB and AC stacking domains can be seen on both ends, while the transition region displays continuously varying dot-like

Moiré pattern in the middle (red rectangle). Only one set of diffraction spots can be obtained from the Fourier transform of the whole image (inset in Figure 2.5a), suggesting that these irregular Moiré patterns are generated via a gradual shift between the two layers without a mis-orientation angle. Importantly, the irregular Moiré patterns continue over a width of several nanometers, which is consistent with the nanometer-wide dark lines (stacking boundaries) observed in DF-TEM images. Moreover, different types of irregular Moiré patterns can be found in the stacking boundary regions. For instance, Figure 2.5c & 2.5d show wiggle-like and square-like Moiré patterns with a gradual transition to regular AB/AC stacking regions. The observed irregular Moiré patterns can have a variety of different orientations with respect to the graphene lattice, as illustrated by the red hexagons in each figure.

The observation of gradually changing Moiré patterns over transition regions of a few nanometers demonstrates that the stacking boundaries are not atomically sharp, but are indeed continuous transitions from AB to AC stacking with gradual lattice deformation. The multitudinous irregular Moiré patterns can also be associated with the wide range of DF-TEM image contrast for these stacking boundaries, confirming their diverse morphologies.

In order to further visualize the detailed atomic structures of the stacking boundaries, I applied classical molecular dynamics (MD) to determine the structure based on experimental STEM-ADF images and compare their stabilities. While it is possible to interpret the position of each atom from regular ADF image patterns for perfect AB stacking, it is challenging to decipher the precise atomic structure from the irregular Moiré patterns such as those shown in Figure 2.5. Thus, I first construct a reasonable

model and relax it to generate the most energetically stable structure. The optimized structures are then used for STEM image simulation and compared to the experimental results.

The gradual and continuous transition from AB to AC stacking can be accomplished in three different scenarios, for stacking boundaries that are parallel to the zigzag direction, armchair direction or a random orientation, respectively: (i) by applying only tensile or compressive strain along the [1, 1] direction (Figure 2.6), (ii) by applying only shear strain along the [1, 1] direction (Figure 2.8), or (iii) by applying a combination of normal and shear strain (Figure 2.9) to the second layer over a transition region of a few nanometers wide.

Figure 2.6 shows two types of structural models for the zigzag-type stacking boundaries with applied normal strain. Specifically, the in-plane tensile strain stretches the second layer in the transition region (Figure 2.6a), whereas compressive strain raises the second layer as ripples (Figure 2.6b), which is energetically more favorable than condensing all the carbon atoms in the same plane, as shown by my DFT calculations detailed in Figure 2.7. The width of the transition stacking boundary region is set to be 8 nm (as measured from TEM and STEM images), and the AB and AC stacking regions are anchored on both sides. I apply a minimum tensile strain of 1.6% in the stretching model, while the compressive strain is mostly released by the ripple. Both models result in an additional shift of 1.42 Å along the [1, 1] direction in the second layer, and generate a relative shift (*i.e.* a non-zero Δx_1) for the 1.23 Å lattice periodicities between the two graphene layers at the transition region. After MD relaxation, both models generate similar dot-like Moiré patterns in the simulated ADF images (insets), similar to those

observed experimentally. Moreover, the total energies for both structures are almost the same (the ripple model is only 2 meV per carbon atom higher than the stretching model).

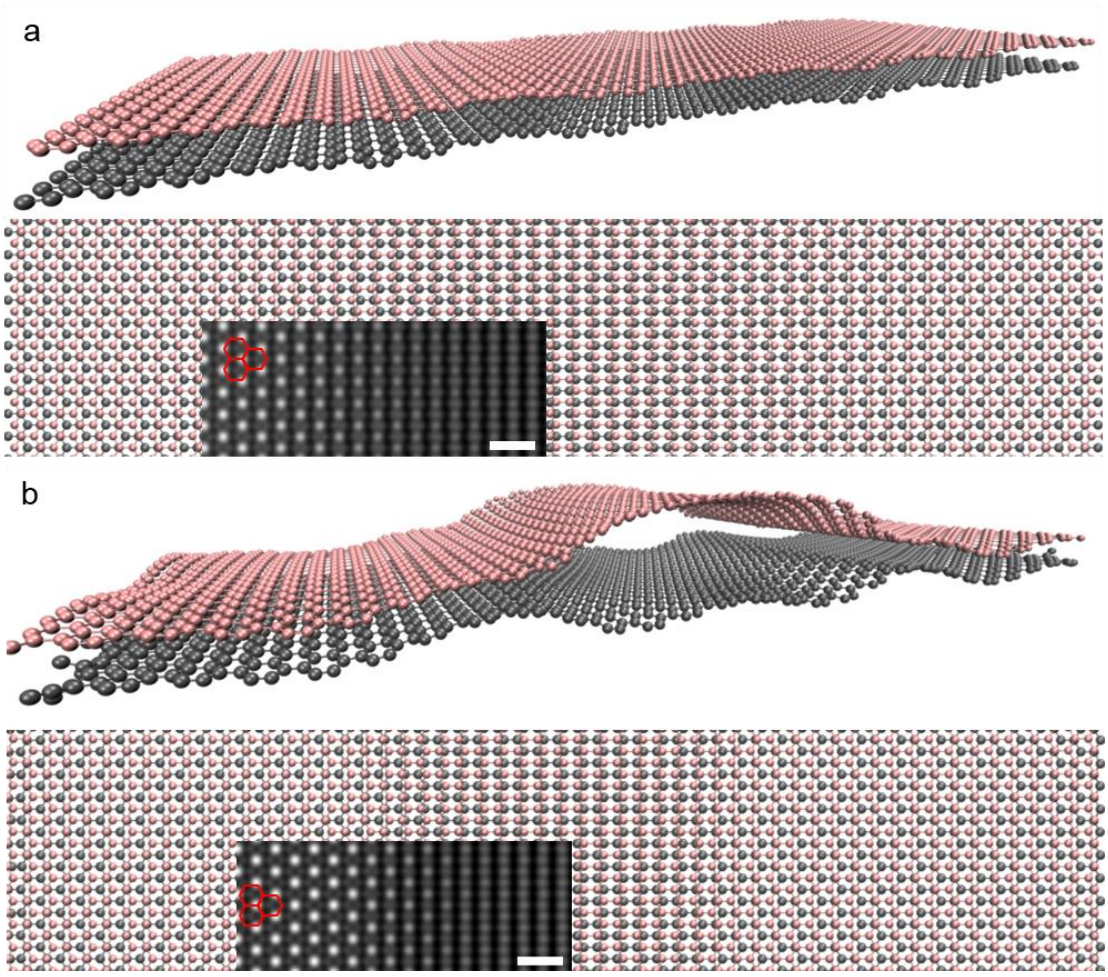

Figure 2.6: Structural models for stacking boundaries along the zigzag direction with applied normal strain. (a) Side view and top view of the MD optimized in-plane stretching model with AB and AC stacking domains anchored on both sides. 1.6% tensile strain is applied in the transition region with a width of 8 nm. (b) Relaxed structural model of a ripple with the same width and anchored sides, containing compressive strain. The height of the ripple is ~ 7 Å. Inset in both images: simulated ADF images in the corresponding regions. Both models generate similar irregular Moiré patterns to those observed in experiments. Red hexagons represent the orientation of graphene lattice in the ordered AB stacking regions. Scale bars: 0.5 nm.

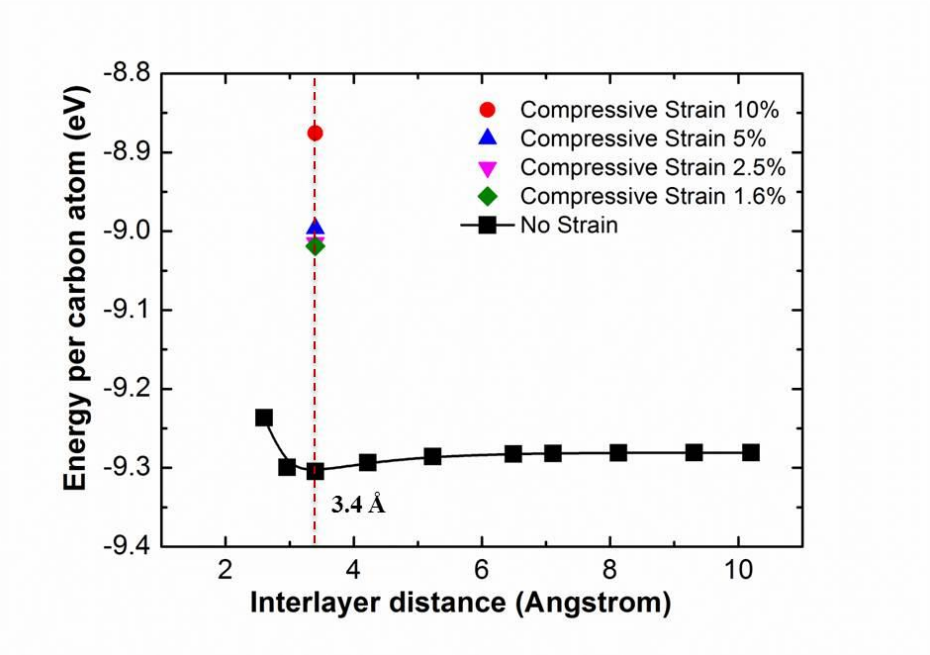

Figure 2.7: Comparison of oBLG structural models with in-plane compressive strain and ripples. When the C-C bonds of the second layer are compressive in plane with the equilibrium interlayer distance (3.4 Å), even at the smallest strain I have tested (~ 1.6%), the energy per carbon atom is much higher, ~ 0.28 eV per carbon atom higher than the equilibrium state. This indicates the effect of in-plane compressive strain is much stronger than the Van der Waals interaction between layers.

However, MD calculations show that the tensile force induced by the strain in the stretching model (Figure 2.6a) is nearly 30 times larger than the force in the ripple models (Figure 2.6b). Therefore, when the constraint of the anchored AB/AC stacking regions is removed in the MD simulation, the second layer in the stretching model tends to shrink to the center in order to release the in-layer tensile force. In contrast, the unanchored AB/AC stacking domains remain stable during MD relaxation when ripples are present in the transition regions. Given the large tensile force present in the in-plane tensile strained stacking boundaries (Figure 2.6a), this type of structure may only exist when the materials are grown under highly nonequilibrium conditions and when there are strong constraints to maintain the AB/AC stacking domains. Therefore, the AB/AC

stacking boundaries are more likely to exist in the form of smooth low-energy ripples, especially in regions with a high concentration of stacking boundaries (such as the red rectangular region in Figure 2.3c) where the accumulation of large tensile forces is energetically undesirable.

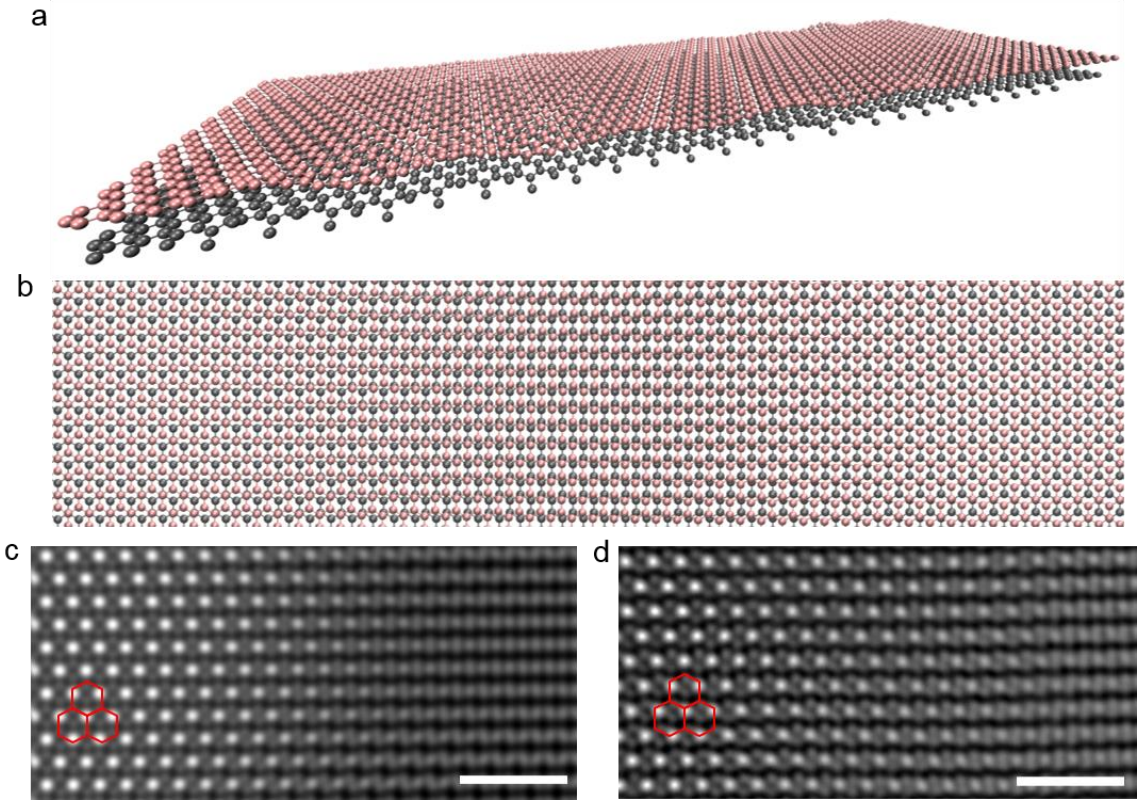

Figure 2.8: Structural model for stacking boundaries along the armchair direction with minimum shear strain. (a, b) Side and top view of the MD optimized model with shear strain along the [1, 1] direction. (c) Corresponding simulated ADF image. Note that only the stacking boundaries parallel to the armchair direction can be constructed by applying shear strain alone. (d) ADF image of experimentally observed stacking boundary with shear strain. Scale bars: 1 nm.

Structure models for the armchair-type stacking boundaries with shear strain are shown in Figure 2.8. In this model, a minimum amount of shear strain (~ 1.2%) is applied

to the second layer, inducing a 1.42 Å shear along the [1, 1] direction over a transition region of 8 nm. After MD relaxation, the force generated by the shear strain is relatively small, and the AB/AC stacking region can be maintained without anchoring the two sides, suggesting that this small amount of shear strain can be easily accommodated at the stacking boundaries. The simulated ADF image (Figure 2.8c) based on the minimum shear strain model also reproduces the dot-like irregular Moiré patterns in the transition region, as have been observed experimentally (Figure 2.8d).

Although the AB to AC stacking transition can be achieved by applying solely normal or shear strain along specific directions (either zigzag or armchair direction), the randomly oriented stacking boundaries with diverse irregular Moiré patterns require that both types of strains are jointly present in the transition regions. A general structural model, aiming to model the stacking boundary observed experimentally in Figure 2.5a, is shown in Figure 2.9a & 2.9b, containing both types of strains and optimized by MD calculations. Here the first layer is set to be relatively flat with thermal vibration on the order of ~1 Å [73]. A small amount of in-plane shear strain is applied to the second layer along the [1, 1] direction (in this case, a 0.71 Å shear over a 8 nm transition region, inducing ~0.6% shear strain), and a ripple of 7 Å in height shifts the second layer 1.23 Å along the [1, -1] direction and releases most of the compressive strain. The simulated ADF image, based on the optimized structural model (Figure 2.9c), matches well with the experimental ADF image (Figure 2.9d) extracted from the boundary region in Figure 2.5a. Moreover, by adjusting the width and the strain profile in the ripple model, a variety of ripple morphologies can be obtained for the stacking boundaries, and the simulated STEM images from these models can well reproduce the irregular Moiré patterns

observed experimentally at the stacking boundaries (such as those shown in Figure 2.5c & 2.5d). For instance, I modified the model shown in Figure 2.9a by keeping the same width but increasing the strain on the ripple (shift 2.84 Å along the [1, 1] direction through the ripple via shear strain), with a height of ~ 10 Å shifting the second layer by 2.46 Å along [1, -1] direction. The optimized structure and the corresponding ADF image simulation are shown in Figure 2.10. Square-like and wiggle-like Moiré patterns can be obtained from this model, coinciding with the experimental images shown in the inset. The results from classical molecular dynamics simulation also suggest that in-plane compressive and shear strains are consistently present in the ripple-like stacking boundaries in order to accomplish the stacking transitions. These results confirm that the AB/AC stacking boundaries can be generally described as nm-wide strained ripples with diverse morphologies and strain levels.

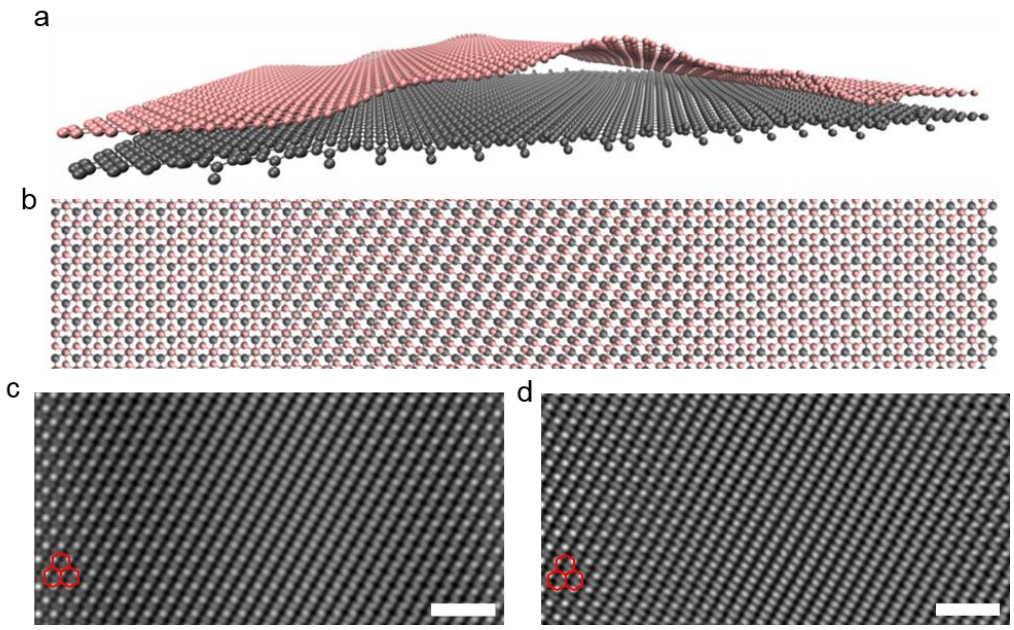

Figure 2.9: Stacking boundaries as strained nm-wide ripples containing both normal and shear strain. (a) Structural model of strained ripples bridging AB and AC stacking domains, optimized by classical molecular dynamics. (b) Top view of the optimized structural model. (c) Simulated STEM-ADF images based on the structural model in

Figure a. (d) Similar Moiré patterns observed in experimental STEM images. Red hexagons represent the orientation of graphene lattice in the ordered AB stacking regions. Scale bars: 1 nm.

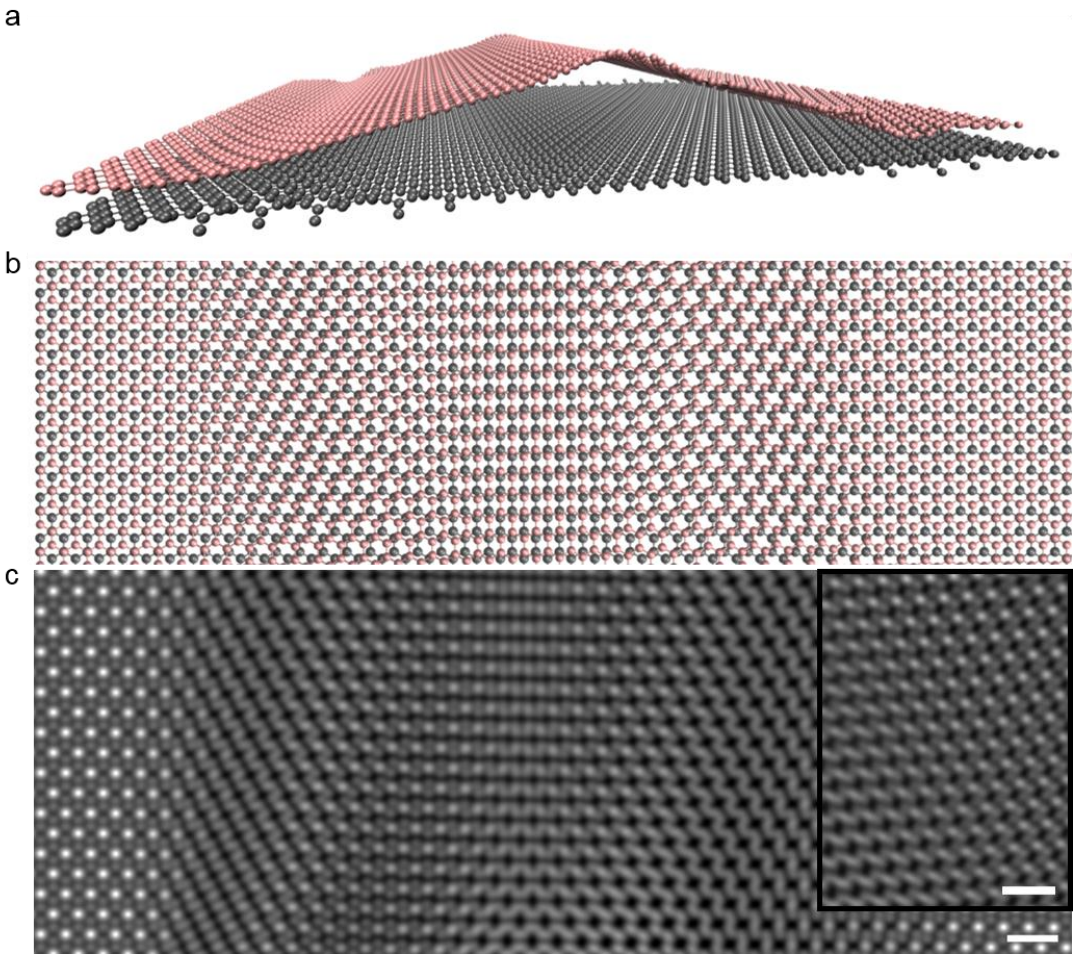

Figure 2.10: Structural model for stacking boundaries with larger compressive and shear strain. (a, b) Optimized ripple model along the armchair-type direction with larger strain level. The width of the ripple is 8 nm, with an optimized height increased to 10 Å. (c) Simulated ADF image using the model in (a), reproducing most of the wiggle-like and square-like patterns observed in experiments (Inset). Scale bars: 0.5 nm.

In conclusion, by combining high resolution electron microscopy imaging and molecular dynamics simulations, I have shown that the unique AB/AC stacking boundaries in Bernal stacked bilayer graphene are not atomically sharp, but nanometer-

wide strained channels, most likely in the form of ripples, with diverse profiles of strain and morphologies. Strain engineering of graphene has been a long sought-after goal for device applications [74, 75]. The omnipresent strained stacking boundaries can, thus, serve as a reservoir to explore the strain effect on the electronic properties of bilayer graphene, and may provide new functional building blocks for future device fabrication.

CHAPTER III

VERTICAL AND IN-PLANE HETEROSTRUCTURES FROM WS_2/MoS_2 MONOLAYERS

Heterostructures have been the essential elements in modern semiconductor industry, and play a crucial role in high-speed electronics and opto-electronic devices [76, 77]. Beyond conventional semiconductors, two-dimensional (2D) materials provide a wide range of basic building blocks with distinct optical and electrical properties, including graphene [78], hexagonal boron nitride [79, 80], and transition-metal dichalcogenides (TMDs) [56, 81-83]. These atomic monolayers could also be combined to create van der Waals heterostructures, where monolayers of multiple 2D materials are stacked vertically layer-by-layer, or stitched together seamlessly in plane to form lateral heterojunctions. Many novel physical properties have been explored on such van der Waals heterostructures, and devices with improved performance have been demonstrated [45, 84-87]. The lateral heterojunctions could also lead to exciting new physics and applications. For example, the semiconducting monolayer TMDs can serve as building blocks for p-n junctions and other opto-electronic devices [88-90].

However, the fabrication of 2D heterostructures with clean and sharp interfaces, essential for preserving opto-electronic properties driven by the interlayer or intralayer coupling, remains challenging. Van der Waals heterostructures could be created by stacking different 2D materials using mechanical transfer techniques [45]. Nevertheless, the stacking orientation cannot be precisely controlled, and the interface between layers can be easily contaminated [91, 92], not to mention the challenge for massive production

of the samples. Lateral heterostructures, in contrast, can only be created via growth. Both vertical and in-plane heterostructures of semimetallic graphene and insulating h-BN have been recently demonstrated via chemical vapor deposition (CVD) [92-96]; however, direct growth of heterostructures consisting of different semiconducting monolayers has not been achieved.

In order to fully develop 2D heterostructures that consist of semiconducting monolayers, I collaborated with Dr. Ajayan's group in Rice University, who developed a scalable single-step vapor phase growth process for the creation of highly crystalline vertical stacked bilayers and in-plane interconnected WS_2/MoS_2 heterostructures, respectively, under different growth temperature. In this project, I performed quantitative atomic resolution Z-contrast STEM imaging to reveal that high temperature growth yields predominantly vertically stacked bilayers with WS_2 epitaxially grown on top of the MoS_2 monolayer, following the preferred 2H stacking. In contrast, the low temperature growth creates mostly lateral heterostructures of WS_2 and MoS_2 within single hexagonal monolayer lattice, with atomically sharp heterojunctions along both the zigzag and armchair directions.

Figure 3.1i shows the scheme for the growth of WS_2/MoS_2 heterostructures. Molybdenum trioxide (MoO_3) powder is placed in front of the bare SiO_2/Si wafer for the growth of MoS_2, while mixed power of tungsten and tellurium is scattered on the wafer for the growth of WS_2. The addition of tellurium helps to accelerate the melting of tungsten powder during the growth. Sulfur powder is put upstream within the low temperature zone. Argon is used to protect the system from oxygen and carry sulfur vapor from the upstream of the tube during the reaction. The difference in their

nucleation and growth rate gives rise to sequential growth of MoS_2 and WS_2, instead of $Mo_xW_{1-x}S_2$ alloy, and the precise reaction temperature determines the structure of the final product: vertical stacked bilayers are preferred at ~850 ˚C, while in-plane lateral heterojunctions dominate when the synthesis was carried out at ~650˚C.

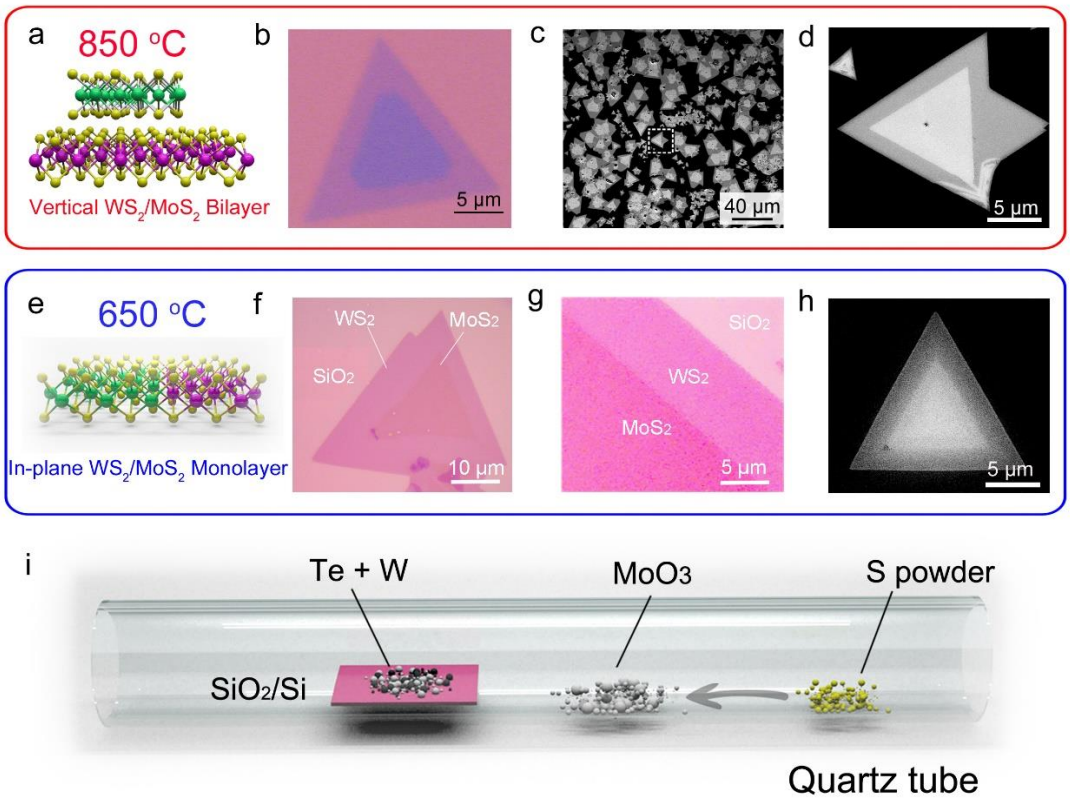

Figure 3.1: Schematic of the synthesis and the overall morphologies of the vertical stacked and in-plane WS_2/MoS_2 heterostructures. (a-d) Schematic, optical and SEM images of the vertical stacked WS_2/MoS_2 heterostructures synthesized at 850 ˚C, showing the bilayer feature and the high yield of the triangular heterostructures. (e-h) Schematic, optical and SEM images of the WS_2/MoS_2 in-plane heterojunctions grown at 650 ˚C. (g) is an optical image of the interface between WS_2 and MoS_2 with enhanced color contrast, showing the abrupt change of contrast at the interface. SEM images are presented in reverse contrast. The green, purple and yellow spheres in (a) and (e) represent W, Mo and S atoms, respectively. (i) Schematic of the synthesis process for both heterostructures.

The growth of the WS_2/Mos_2 heterostructures is proposed to follow the chemical reaction equations below:

$$2MoO_3+7S \xrightarrow{650\,℃} 2MoS_2+3SO_2 \quad (1)$$

$$MoS_2(edge)+W(Te)+2S \xrightarrow{650\,℃} WS_2/MoS_2(lateral)+Te \quad (2)$$

$$2MoO_3+7S \xrightarrow{850\,℃} 2MoS_2+3SO_2 \quad (3)$$

$$MoS_2(Surface)+W(Te)+2S \xrightarrow{850\,℃} WS_2/MoS_2(vertical)+Te \quad (4)$$

According to the chemical reaction equations in such growth conditions, MoS_2 always grows first as the bottom layers or at the center (chemical reaction equation (1) or (3)) because of its high nucleation and growth rate during vapor phase reaction. On the other hand, WS_2 nucleation and growth is much slower, due to the low vapor pressure of W and low solubility of W in liquid Te under the 650 - 850 ℃ reaction temperature.

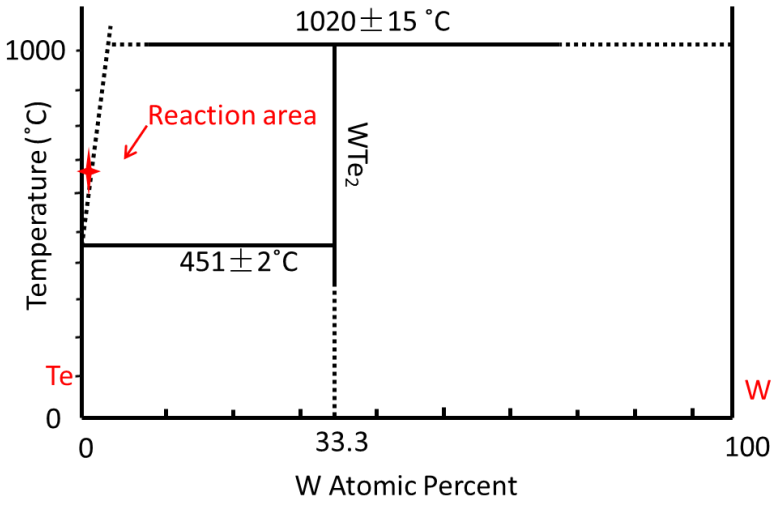

Figure 3.2: Binary phase diagram of W-Te [97]. The area marked by red arrow shows that W is a little soluble in liquid Te above 450 ℃.

Phase diagram (Figure 3.2) shows that Te accelerates the melting of tungsten, which then reacts with S to form WS_2 atomic layers. Because of the ultrahigh melting temperature of W on its own, the growth of WS_2 with W-Te mixed powder as precursor should be a liquid reaction rather than a vapor reaction. This is the reason why the W-Te mixed powder is placed on the growth substrate directly. The growth under similar synthesis conditions without using Te results in only MoS_2 atomic layers and bulk WS_2 particles. The large difference in reaction rate gives rise to the vertical stacked or in-plane WS_2/MoS_2 heterostructure rather than the random $Mo_xW_{1-x}S_2$ alloy. For comparison, if WO_3 ,instead of W-Te, is used as precursor for the growth, only random $Mo_xW_{1-x}S_2$ alloy is obtained, presumably due to the similar sublimation rate of WO_3 and MoO_3. Therefore, this simple, scalable growth process creates clean interfaces between the two monolayer components, which is advantageous over mechanical transfer of layers.

The morphology of the WS_2/MoS_2 vertical and in-plane heterostructures was examined by optical microscopy, scanning electron microscopy (SEM), and atomic force microscopy (AFM). Figures 3.1a – 3.1d are the schematic and typical optical and SEM images of the vertical stacked heterostructures, showing individual WS_2/MoS_2 bilayer triangles and high yield of heterostructures. The bilayers can be easily distinguished from monolayers via optical contrast (Figure 3.1b), with MoS_2 monolayers showing light purple color and the bilayer regions in much darker purple. The domain size of the bottom MoS_2 layer is typically larger than 10 μm. Both totally covered and partially covered WS_2/MoS_2 bilayer can be found, providing different geometries for device fabrication. The schematic and morphology of WS_2/MoS_2 in-plane heterostructures is

shown in Figures 3.1e – 3.1h, where the lateral interface between monolayer MoS_2 and WS_2 can be easily distinguished by the contrast difference.

Preliminary results on the vertical stacked WS_2/MoS_2 bilayers were obtained by my colleague via Z-contrast imaging and elemental mapping in an aberration-corrected STEM. Figure 3.3a shows the morphology of the as-transferred stacked WS_2/MoS_2 heterostructure in a low-magnified Z-contrast image, where the image intensity is directly related to the averaged atomic number and the thickness of the sample [72, 98, 99]. A WS_2 monolayer would, therefore, display higher image contrast than a MoS_2 monolayer, while the image intensity from the bilayer heterostructure is roughly the sum of that from its two monolayer components. In order to highlight the different regions in the sample, the image in Figure 3.3a is shown in a false color scale. Most of the sample is covered by continuous bilayer heterostructure (orange region), while at some intentionally induced broken edges both of the individual monolayers can be identified (with MoS_2 shown in blue and WS_2 shown in green). Figure 3.3b shows a magnified image of the region highlighted in Figure 3.3a. The obvious contrast step across the two individual layers, as shown by the image intensity line profile in Figure 3.3c, demonstrates the presence of separated MoS_2 and WS_2 monolayers instead of a homogenous $Mo_xW_{1-x}S_2$ alloy.

Elemental mapping of Mo, W and S on the same region were shown in Figure 3.3b. EEL spectra of the individual MoS_2 and WS_2 monolayer regions shows distinct feature for Mo and W (Figure 3.4), from which the chemical composition of the bilayer region can be mapped out. Figure 3.3d shows the elemental mapping of Mo, W and S, confirming that MoS_2 and WS_2 are well separated into two atomic layers, forming vertical bilayer heterostructures.

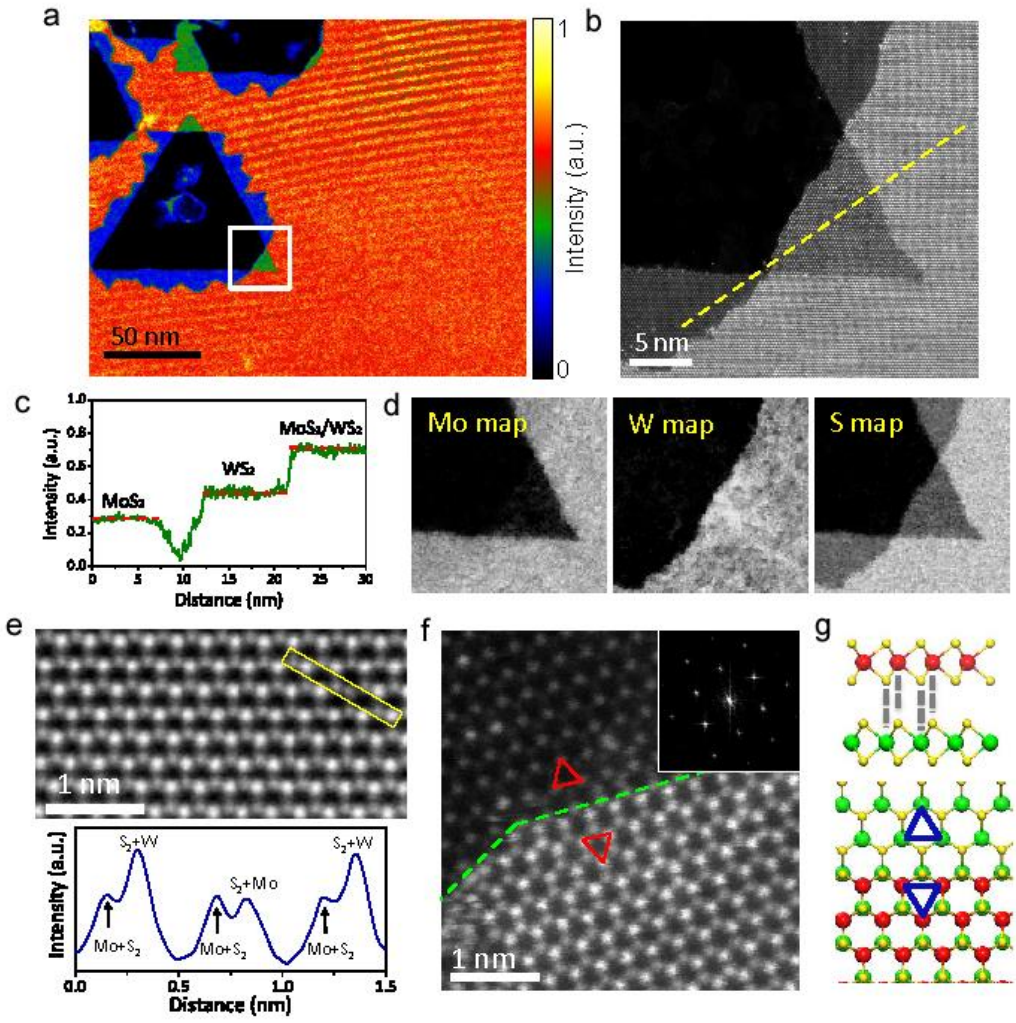

Figure 3.3: STEM-Z-contrast imaging and elemental mapping of the stacked WS_2/MoS_2 heterostructures. (a) Low-magnified false-colored Z-contrast image of the sample, where monolayer MoS_2 is shown in blue, monolayer WS_2 in green, and WS_2/MoS_2 bilayer in orange. (b) Zoom in view of the region highlighted in (a). (c) Z-contrast image intensity profile along the highlighted dashed line in (b), showing the distinct contrast variation among the different monolayers and bilayer region. (d) Elemental mapping of Mo, W, and S from the whole area shown in (b). (e) Z-contrast image of the bilayer region with 2H stacking orientation. The brighter columns are overlapping columns of W and S_2, while the less bright columns are overlapping of S_2 and Mo. The green arrow points to the atomic positions where W atom is replaced by Mo in the WS_2 layer, which has similar intensity to its neighboring site. Below: Image intensity profile acquired along the yellow rectangle in (e). (f) Z-contrast image of the step edge of the WS_2/MoS_2 bilayer. The green dash line highlights the step edge, and the two triangles highlight the orientation of the MoS_2 and WS_2 layer, respectively. Inset: FFT of the Z-contrast image showing only one set of diffraction pattern. (g) Schematic of the 2H stacking in the stacked WS_2/MoS_2 heterostructure.

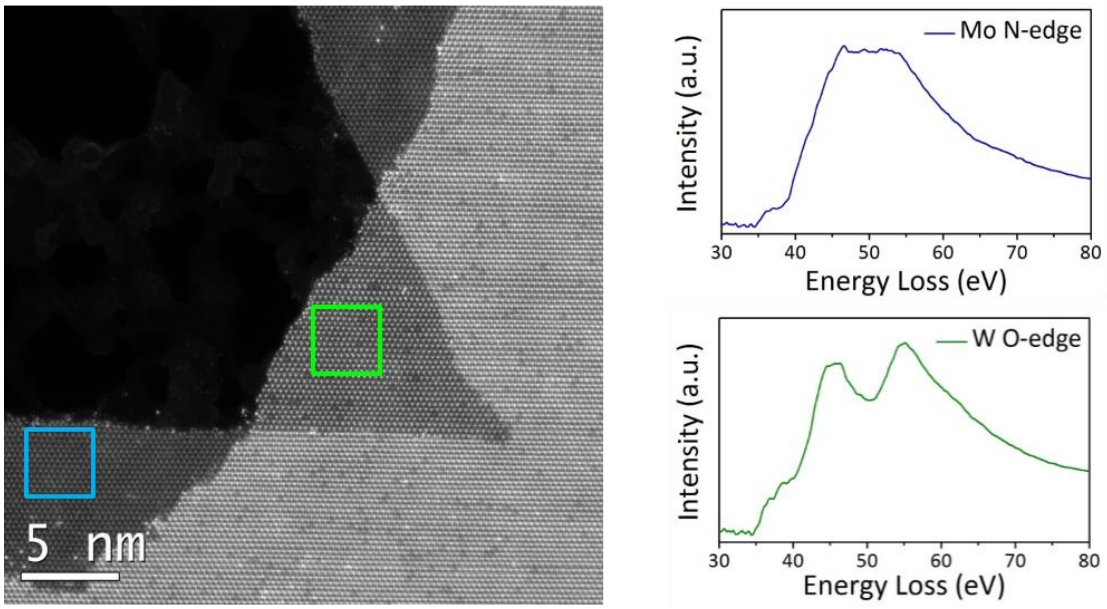

Figure 3.4: Chemical identity of the two monolayers in the WS_2/MoS_2 vertical stacked bilayer. The chemical identity of each individual layer is confirmed by EELS. EELS spectra (right) collected from the individual MoS_2 and WS_2 monolayers (green and blue squares in the Z-contrast image shown in the left, respectively) show distinct fine structures for Mo N-edge in MoS_2 and W O-edge in WS_2, confirming the presence of the well-separated MoS_2 and WS_2 monolayer.

Figures 3.3e and 3.3f show atomic resolution Z-contrast images from the bilayer region and a step edge of the WS_2/MoS_2 heterostructure, respectively. The alternative bright and dark atomic column arranging in the hexagonal lattice suggests the as-grown stacked WS_2/MoS_2 heterostructure preserves the 2H stacking, where the bright and dark columns are W and Mo atom aligned with a S_2 column, respectively, as illustrated in Figure 3.3g. The WS_2/MoS_2 heterostructure grown by this one-step growth method is found to have predominantly the 2H stacking, which exemplifies the advantage of this direct growth method over mechanical transfer method where the stacking orientation of the heterostructure cannot be well controlled. As a side note, Mo substitution in the WS_2 layer can be occasionally observed, as indicated by the reduced contrast at the W atomic

sites (green arrows in Figure 3.3e and the associated intensity line profile). Similarly, some trace amount of W atoms is also found to substitute into the MoS_2 layer (Figure 3.3f). By mapping out individual W atoms within the MoS_2 lattice, the substitution was estimated and found to be at a fairly low concentration (~ 3%), as indicated by Figure 3.5. This result suggests that W impurities would only have minimum effect on the properties of the MoS_2 monolayers.

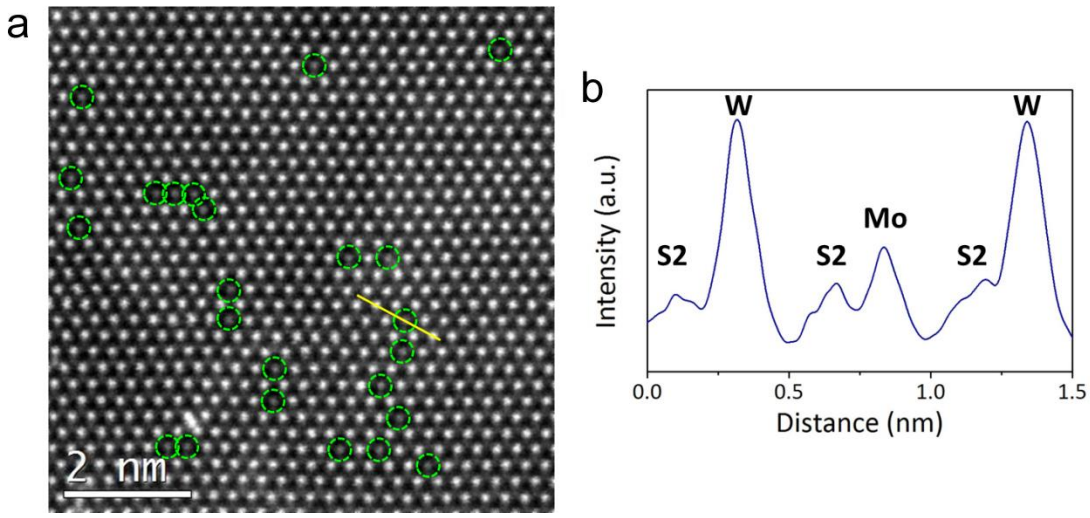

Figure 3.5: STEM-Z-contrast image analysis of WS_2 monolayer with Mo substitution. (A) Z-contrast image showing some of the metal sites in the monolayer WS_2 having weaker image intensity. (B) Image intensity profile acquired along the yellow line in A, showing the change in image contrast due to substitution of Mo at W site. Using the site-separated histogram analysis method discussed in literature [100], the location of the substituted Mo atoms can be mapped out, as highlighted by the dash green circles, and the local Mo concentration is about 3%.

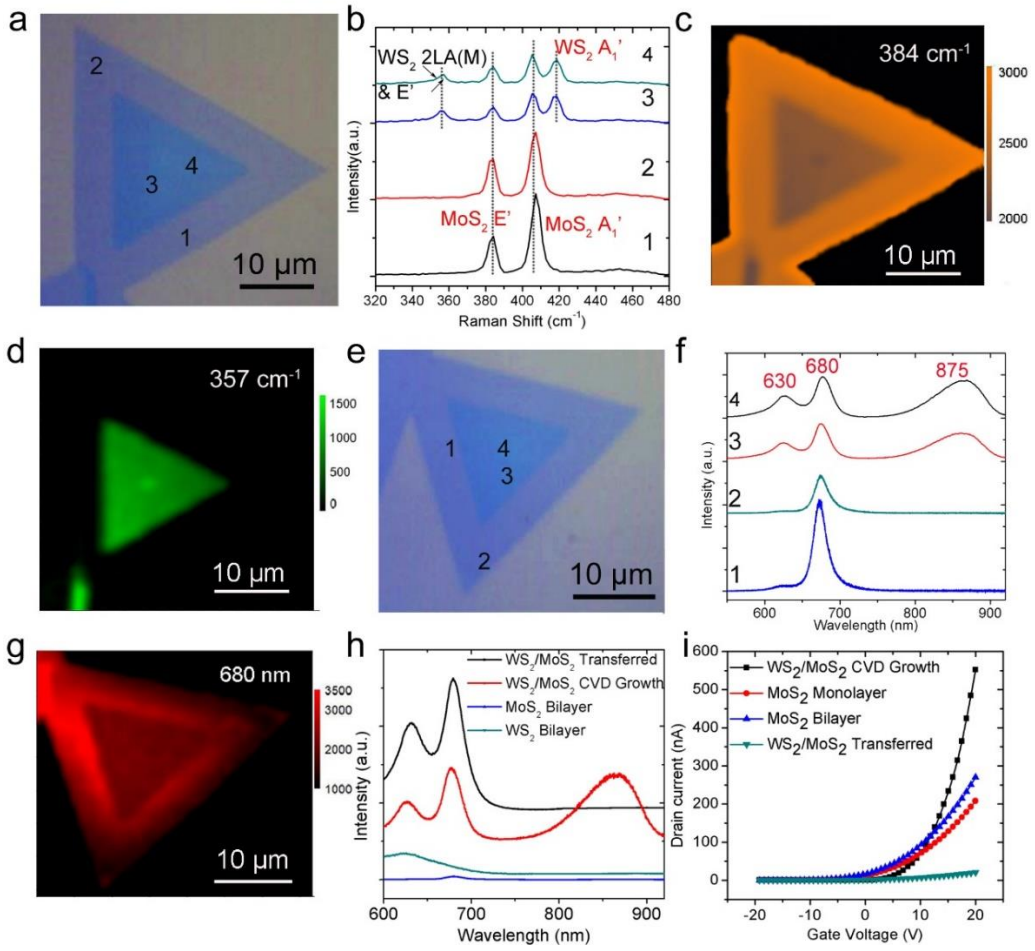

Figure 3.6: Raman and PL characterization of the WS_2/MoS_2 vertical heterostructure. (a) Optical image of a WS_2/MoS_2 heterostructure used for Raman characterization. (b) Raman spectra taken from the four points marked in (a), showing that the monolayer region is pure MoS_2, while the double layer area is the superposition of MoS_2 and WS_2 monolayers. (c, d) Raman intensity mapping at 384 cm^{-1} and 357 cm^{-1}, respectively. The lower Raman intensity at the center of the triangle in (c) is due to the coverage of WS_2. (e) Optical image of a WS_2/MoS_2 heterostructure used for PL characterization. (f) PL Spectra taken from the four points marked in (e), showing the characteristic MoS_2 PL peak at the monolayer region and three peaks at the bilayer region. (g) PL intensity mapping at 680 nm shows localized PL enhancement around the step edge of the bilayer region. (h) PL spectra of CVD-grown WS_2/MoS_2 bilayer, WS_2/MoS_2 bilayer made by mechanical transfer, and CVD-grown MoS_2 and WS_2 bilayers, respectively. All spectra were taken at the same laser intensity and plotted to the same scale. The PL peak at 875 nm is absent at the mechanically transferred bilayer sample, and the bilayer MoS_2 and WS_2 have very weak PL response due to their indirect bandgap. (i) Typical plot of gating voltage versus source/drain current of CVD-grown WS_2/MoS_2 bilayer, mechanically transferred WS_2/MoS_2 bilayer, MoS_2 bilayer, and monolayer MoS_2, respectively, demonstrating that the CVD-grown WS_2/MoS_2 bilayer has the best performance.

Raman and PL spectroscopy performed by collaborators in Rice and Penn State University were used to further characterize the vertical bilayer heterostructure. As shown in Figures 3.6a and 3.6b, Raman spectra collected from the light purple area (points 1 and 2) show only the $E^{'}$ (at 383.9 cm^{-1}) and $A_1^{'}$ (at 405.3 cm^{-1}) peaks of MoS_2 monolayer [82, 83], confirming the bottom layer is MoS_2 [99]. In the bilayer region (point 3 and 4 in the dark purple area), however, two additional peaks located at 356.8 cm^{-1} and 418.5 cm^{-1} are observed, which can be assigned to the overlapping 2LA(M) & $E^{'}$ and $A_1^{'}$ modes, respectively, of the top WS_2 monolayer [81, 100]. Raman intensity mapping using the MoS_2 $E^{'}$ mode at 384cm^{-1} and the WS_2 $E^{'}$ mode at 357cm^{-1} further demonstrate the formation of WS_2/MoS_2 bilayer stacks, as shown in Figures 3.6c and 4.6d. The PL spectra (Figure 3.6f) acquired from the monolayer region (points 1 and 2 in Figure 3.6e) show only a strong peak at the wavelength of 680 nm, corresponding to the 1.82 eV direct excitonic transition energy in monolayer MoS_2. However, on the bilayer region (points 3 and 4), three prominent peaks are observed at the wavelength of 630 nm, 680 nm, and 875 nm, corresponding to the excitonic transition energy of 1.97 eV, 1.82 eV, and 1.42 eV, respectively. The peaks at 630 nm (1.97 eV) and 680 nm (1.82 eV) can be attributed to the direct excitonic transition energy in the top WS_2 and bottom MoS_2 monolayer, respectively. It has been reported that the increased indirect excitonic transition in multilayer WS_2 and MoS_2 [56, 101] can generate small peaks at similar lower transition energy range. The intensity of such indirect excitonic peaks, however, is more than three orders of magnitude lower than the direct excitonic peak from monolayers. The comparable intensity of the peak at 875 nm to that of its individual monolayer components observed in the bilayer sample, as shown in Figure 3.6f, indicates

a possible direct excitonic transition at this energy range. Such strong direct excitonic peak at 875 nm (1.42 eV) is indeed observed for the first time in this bilayer heterostructure. This experimental observation is consistent with previous theoretical calculations, which suggest the coupling between the WS_2 and MoS_2 layers leads to a new direct bandgap with reduced energy [102, 103].

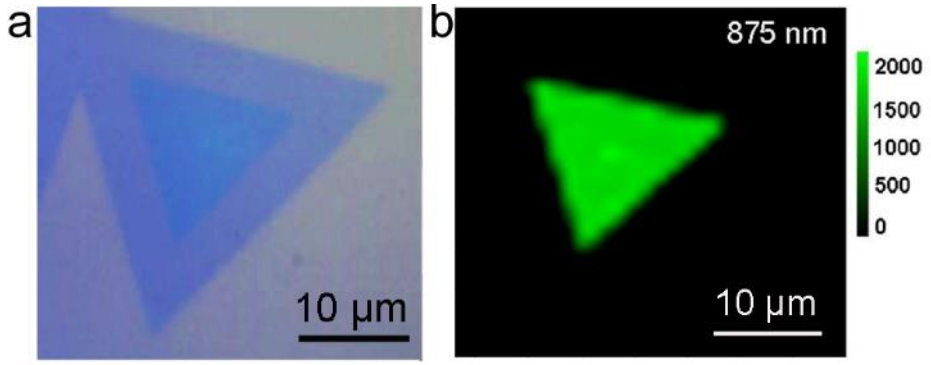

Figure 3.7: The PL intensity mapping at 875 nm of WS_2/MoS_2 stacked bilayer, confirming the intensity is localized at the bilayer region.

Figure 3.7 shows the PL intensity mapping at 875 nm, confirming the intensity are localized at the bilayer region. Notably, the PL signal from MoS_2 at 680 nm shows a localized enhancement near the step edges between the monolayer and bilayer region, as shown in Figure 3.6g. The PL enhancement is also demonstrated by analyzing the PL spectra extracted from the step edge region (point 1) and the edge of the MoS_2 monolayer (point 2 in Figure 3.6e), showing almost twice difference in intensity. This step-edge enhancement is distinctly different from the previous reported edge-enhanced [81] or homogeneous [104] PL response in monolayer TMDs, and may be caused by the interaction between the MoS_2 and WS_2 layers.

As a comparison, PL measurements were also performed on stacked WS_2/MoS_2 heterostructure, made by the commonly-used mechanical transfer method, and on CVD grown MoS_2 and WS_2 bilayer (Figure 3.6h). The additional PL peak at 875 nm, originated from interlayer excitonic transition [102, 103], is absent in the PL spectra from the mechanically transfer stacked bilayer sample, presumably due to contaminations at the interface during the mechanical transfer of the two layers. This new 875 nm peak should also be observable in transferred layers if a contamination-free interface could be achieved. These results highlight the advantage of using the CVD method for the direct growth of crystalline heterostructures, in which layer transfers are not needed and clean interface could be readily obtained. In addition, the 1.82 eV (680 nm) and 1.97 eV (630 nm) PL peaks observed in the stacked WS_2/MoS_2 bilayer are almost vanished in CVD-grown MoS_2 bilayer and WS_2 bilayer [56]. This observation suggests that the MoS_2 and WS_2 layers in the bilayer heterostructure, on one hand, behave as individual monolayers, and, on the other hand, generate new functionalities (a new direct band gap) of WS_2/MoS_2 heterostructure via interlayer coupling owing to the clean interface.

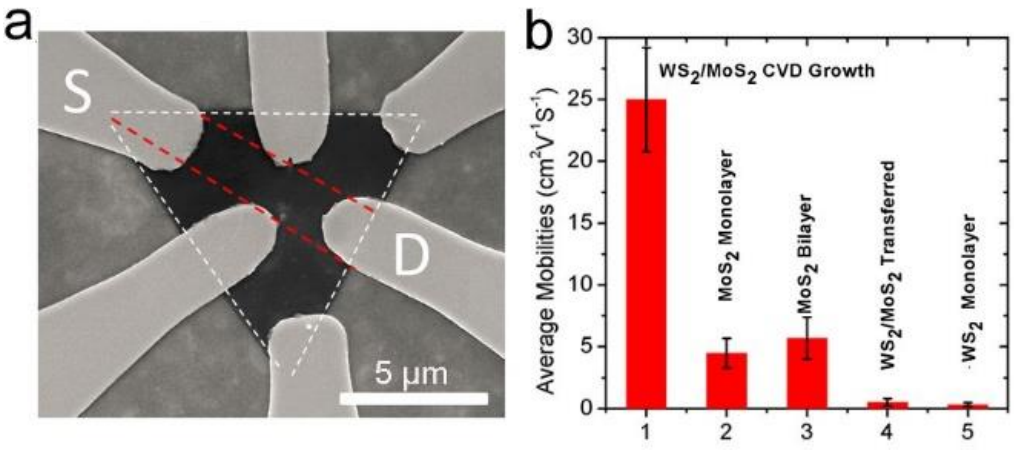

Figure 3.8: Field-effect transistor (FET) characterization of the vertical stacked WS_2/MoS_2 bilayer. (a) A typical SEM image of FET device from WS_2/MoS_2 bilayer

stacks. (b) Histogram of the average mobility of CVD-grown WS_2/MoS_2 bilayer, mechanically transferred WS_2/MoS_2 bilayer, MoS_2 bilayer, and monolayer MoS_2, respectively. 10 devices are used to calculate the average mobility in each case.

My collaborators also demonstrated high-mobility back-gating field-effect transistors (FETs) made by these vertically stacked WS_2/MoS_2 heterostructures as shown in Figure 3.6i and Figure 3.8, which is the evidence of the high quality of these CVD-grown film. As FETs, the ON/OFF ratio is larger than 10^6, and the estimated mobility ranges from 15 to 34 $cm^2V^{-1}s^{-1}$, which is much higher than the average mobility of the monolayer MoS_2 (4.5 $cm^2V^{-1}s^{-1}$) [82, 83], MoS_2 bilayer (5.7 $cm^2V^{-1}s^{-1}$) and WS_2/MoS_2 bilayer made by transfer method (0.51 $cm^2V^{-1}s^{-1}$), thus suggesting that the clean interface between WS_2 and MoS_2 is important for achieving a high device performance. The poor FET performance WS_2/MoS_2 bilayer made by transfer method is possibly due to the presence of unwanted species trapped between layers.

I continue to perform high resolution STEM Z-contrast imaging to study the atomic structure of the lateral interface in the in-plane WS_2/MoS_2 heterojunction. The lateral interface between WS_2 and MoS_2 within the in-plane connected heterostructure appears as straight lines in triangular shape in the optical images (Figures 3.1e-3.1h), thus suggesting that the lateral epitaxy of WS_2 on MoS_2 edge occurs preferentially along the zigzag direction. Figure 3.9a shows an atomic resolution Z-contrast image of the lateral interface, where W atoms display much higher image intensity than the Mo atoms. A series of sharp zigzag step interfaces can be easily identified along the overall-straight WS_2/MoS_2 lateral junction. An atomically sharp interface is consistently observed.

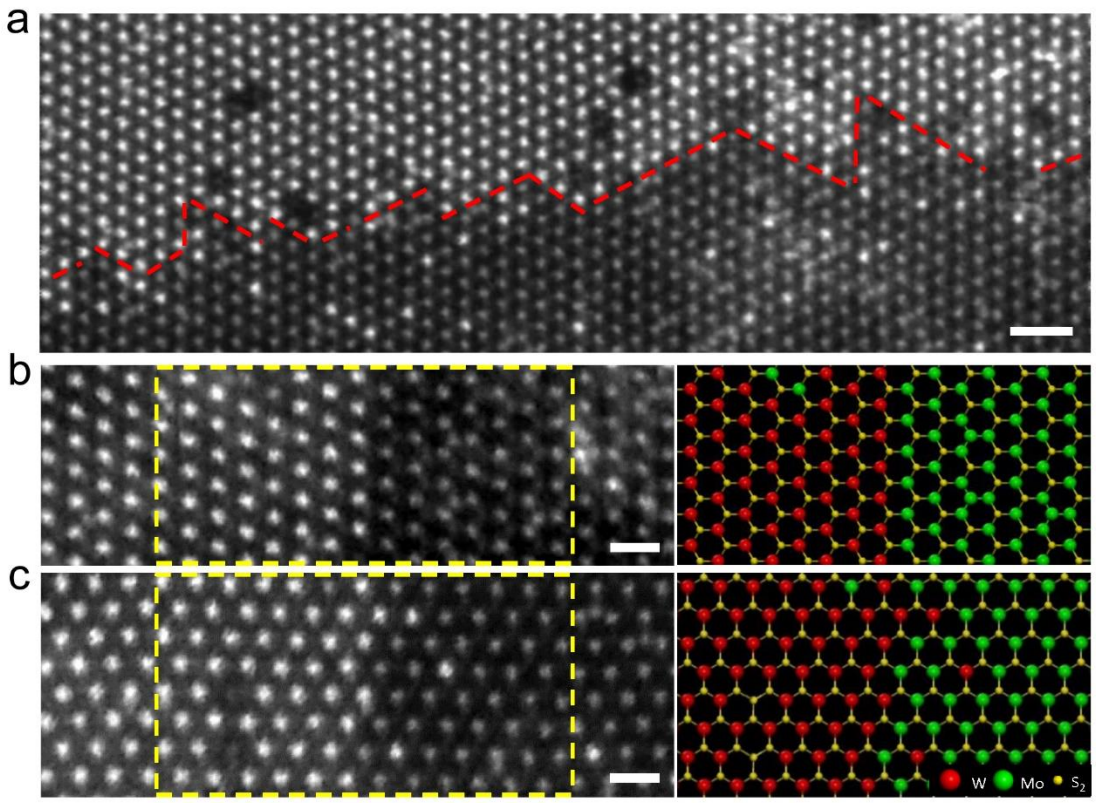

Figure 3.9: Atomic structure of the lateral heterojunctions between WS_2 and MoS_2 monolayers. (a) Atomic resolution Z-contrast STEM images of the in-plane interface between WS_2 and MoS_2 domains. Small roughness resulting from interfacial steps can be seen in (a). The red dashed lines highlight the atomically sharp interface along the zigzag-edge direction. (b, c) Atomic resolution Z-contrast images of the atomically sharp lateral interfaces along the zigzag (b) and armchair (c) directions. The atomic models on the right correspond to the structure in the highlighted regions. Scale bars: (a) 1 nm; (b-c) 0.5 nm.

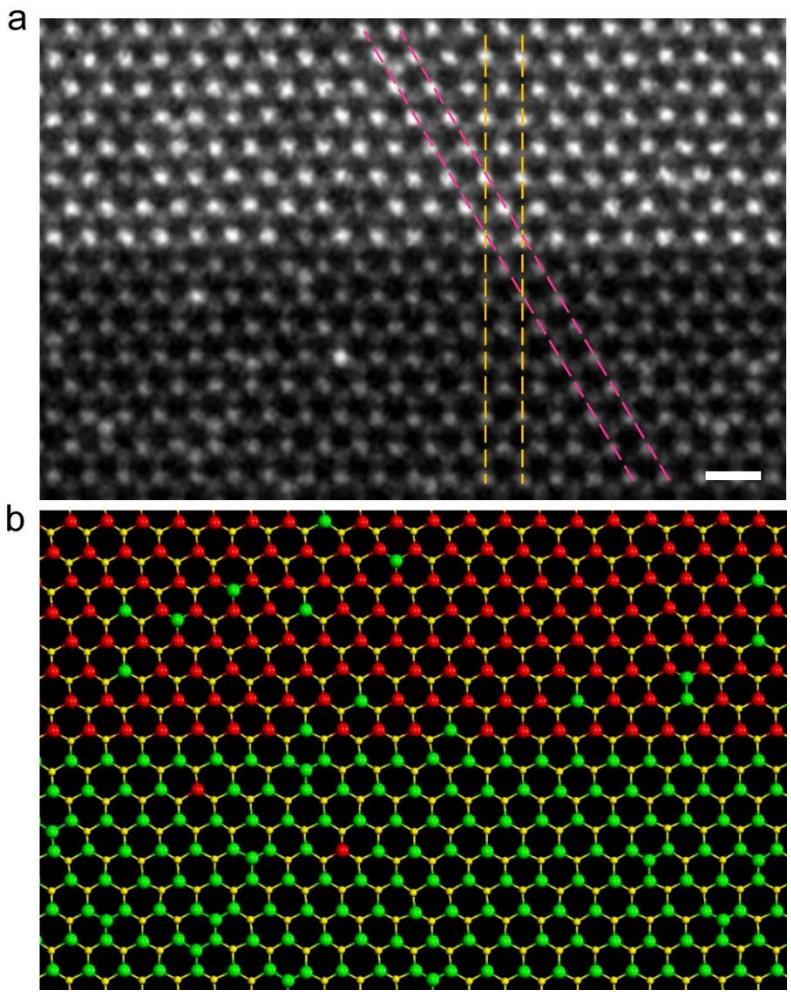

Figure 3.10: Seamless connection of the MoS_2 and WS_2 at the interface. (a) High resolution STEM Z-contrast image of the lateral interface where all atoms are clearly visible. The orange and pink dashed lines depict the atomic planes along the arm-chair and zigzag directions, respectively, which further illustrate that the WS_2 and MoS_2 regions share the same crystal orientation. (b) Atom-by-atom mapping of (a). Green: Mo; Red: W; Yellow: S. Scale bar: 0.5 nm.

Figure 3.10a shows another atomically sharp interface along the zigzag direction, where all atomic columns are directly visible. Careful examination of this STEM image reveals that the WS_2 and MoS_2 domains connect seamlessly at the interface into a single hexagonal monolayer lattice and share the same crystal orientation, as demonstrated in Figure 3.10a with the atomic model in Figure 3.10b. The formation of

such atomically coherent interface is a strong indication of lateral expitaxy growth in which the WS_2 monolayer grows directly from the fresh MoS_2 edges with atomic lattice coherence. Lateral expitaxy is also supported by the electron diffraction pattern as shown in Figure 3.11.

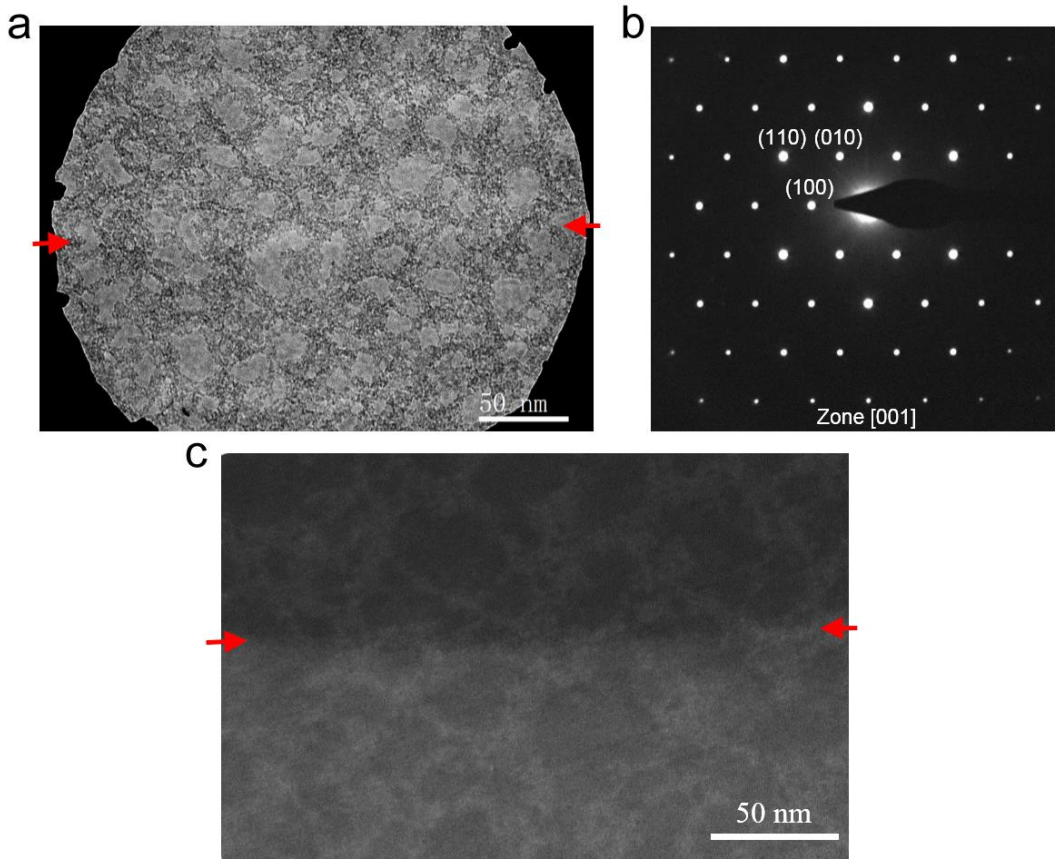

Figure 3.11: Electron diffraction pattern of a 300 nm region containing a lateral interface. (a) TEM bright field image with selected area aperture. (b) Electron diffraction pattern taken from (a) showing only one set of diffraction. (c) Low magnification STEM Z-contrast image of the same area. The position of the interface is indicated by the red arrows.

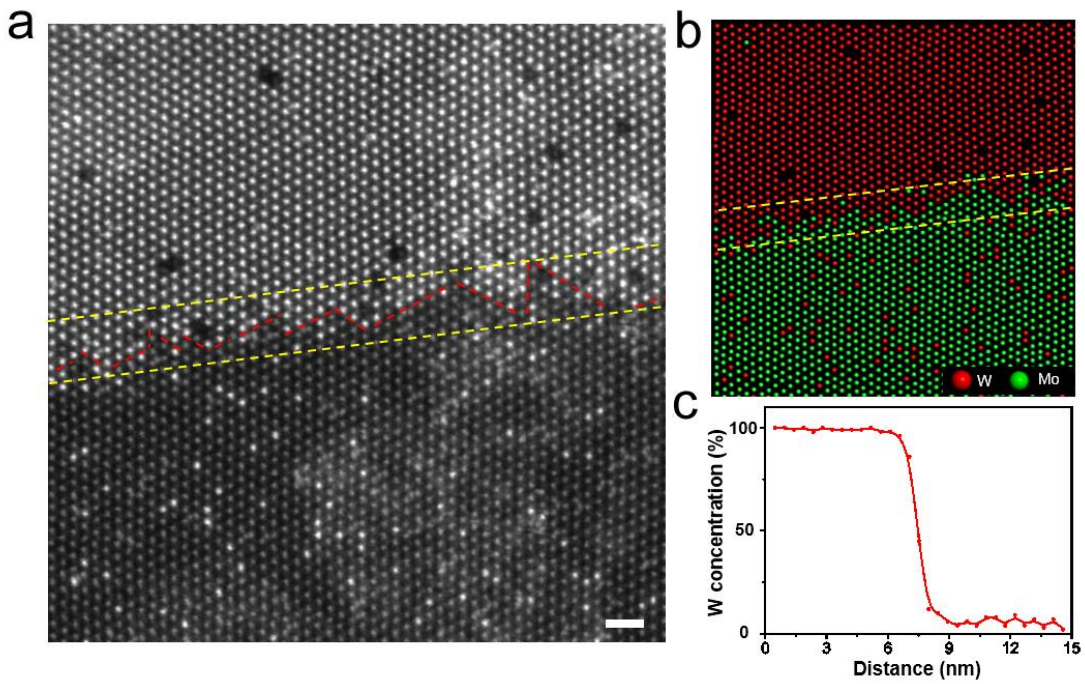

Figure 3.12: Atom-by-atom analysis of the lateral WS_2-MoS_2 interface. (a) Z-contrast STEM image of the in-plane boundary between MoS_2 and WS_2 domains as shown in Fig. 4A (main text), with a larger view. The yellow dashed lines indicate the roughness of the interface. (b) Atomic mapping of the Mo and W atoms distribution in (a). (c) W concentration estimated along the axis perpendicular to the yellow dashed line (the overall direction of the interface), which averages the W concentration in each individual atomic plane. The width of the boundary is estimated to be within 4 unit cells. The Mo concentration in the WS_2 side is ~ 0.2%, while the W in the MoS_2 side is ~ 7.4%. Scale bar: 1 nm.

The interfacial steps most likely originate from small fluctuations of the MoS_2 growth rate at the nm-scale, and their presence contributes to the overall roughness of the lateral WS_2/MoS_2 interface. I estimated the overall roughness of the WS_2/MoS_2 interface by the evolution of the local W concentration, integrated along individual atomic planes parallel to the overall interface, as presented in Figure 3.12. The overall roughness of the lateral interface is estimated to be ~4 unit cells over a width of 15 nm (Figure 3.12), which could be further reduced by optimizing the CVD growth conditions.

Despite the small overall roughness due to interfacial steps, each individual WS_2/MoS_2 heterojunction along the zigzag direction is found to be atomically abrupt, as shown by the high magnification STEM Z-contrast images in Figures 3.9b and 3.10. The corresponding atomic model, obtained via atom-by-atom image quantification, clearly indicates the seamless connection and abrupt transition between the MoS_2 and WS_2 lattice within a single atomic row. This is the first demonstration and direct visualization of an atomically abrupt lateral interface between two different 2D materials with atomic resolution. Besides the preferred zigzag interface, lateral junctions along the armchair direction are also occasionally observed in the sample, as shown in Figure 3.9c. Slight inter-diffusion of transition metal elements is often observed along such armchair interfaces, typically over a width of 1-3 unit cells, presumably due to the relative low stability of the fresh armchair MoS_2 edges during the epitaxial growth of the WS_2 layer [105]. Nevertheless, this growth method produces the highest quality 2D in-plane heterostructures reported so far, with atomically coherent sharp interfaces, providing an excellent platform for studying intralayer coupling effect.

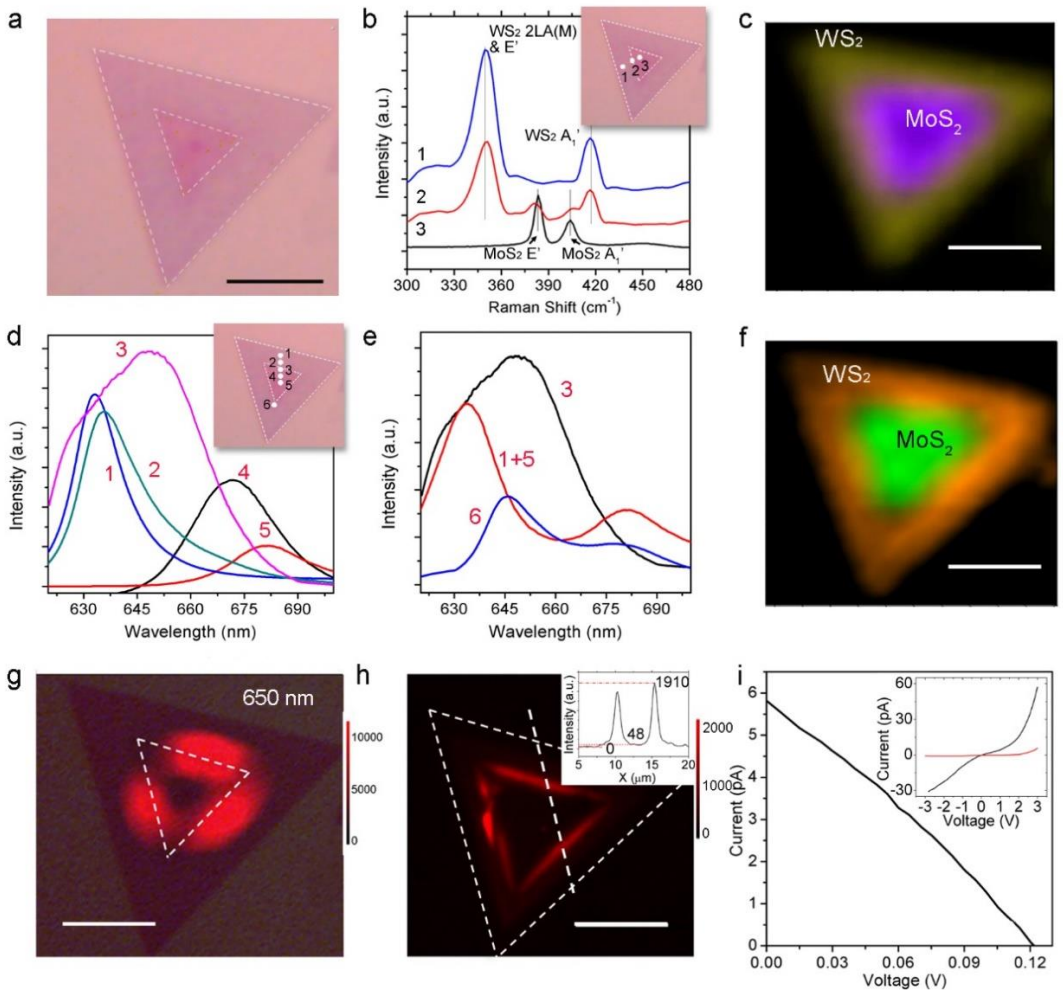

Figure 3.13: Raman and PL characterizations of in-plane WS_2/MoS_2 heterojunction. (a) Optical microscopy image of a triangular in-plane WS_2/MoS_2 heterojunction for Raman and PL characterization. (b) Raman spectra taken from the points marked by 1-3 in its inset. (c) Combined Raman intensity mapping at 351 cm^{-1} (yellow) and 381 cm^{-1} (purple), showing the core-shell structure with WS_2 as the shell and MoS_2 as the core. (d) PL spectra of the points marked by 1-5 in its inset. The peak positions for spectra 1 and 5 are 630 nm and 680 nm, respectively. (e) PL spectra at the interface (point 3), at the intersection of interface (point 6) and the superposition of spectra from pure MoS_2 (point 5) and pure WS_2 (point 1). (f) Combined PL intensity mapping at 630 nm (orange) and 680 nm (green). (g) PL intensity mapping at 650 nm, showing localized response around the interface. The optical image with interface highlighted is overlaid in (g). (h) PL microscope image of the same region in (g) in false color, showing strong localized PL enhancement at the interface. Inset is the corresponding intensity profile along the marked dash line, and the corresponding intensities of interface, pristine MoS_2 and back ground are marked. (i) Photo-voltaic effect of the in-plane heterojunction. Inset is the typical I-V curve of the junction with (black) and without (red) illumination, showing the p-n junction behavior. Scale bar: (a, c, f, g, h) 10 μm.

The lateral WS_2/MoS_2 interface was further studied by Raman and PL spectroscopy. Figure 3.13a shows an optical image of the WS_2/MoS_2 in-plane heterojunction used for Raman and PL characterization. Raman spectra (Figure 3.13b) and mapping (Figure 3.13c) at 351 cm^{-1} (yellow) and 381 cm^{-1} (purple) both confirm the formation of in-plane WS_2/MoS_2 heterostructure, with triangular monolayer MoS_2 domain as the core and WS_2 being the shell layer. Similarly, PL spectra acquired from the outer layer (point 1 in Figure 3.13d) and inner layer (point 5 in Figure 3.13d) show characteristic PL peaks of pristine monolayer WS_2 and MoS_2, respectively, and the PL intensity mapping using these two peaks also reveals the core-shell structure of this unique lateral heterostructure (Figure 3.13f). Note that due to the large laser spot size (~1 μm) used in the experiment, the lateral interface in the Raman and PL mappings appears a bit diffuse, and the Raman spectrum from the interface area correspond to signals from both sides of the atomically abrupt heterojunction.

Even though the lateral heterostructure has been revealed by my STEM imaging to have sharp interfaces with very limited inter-diffusion, the PL peak position shifts continuously across the interface from 630 nm (for WS_2) to 680 nm (for MoS_2), as shown by the spectra presented in Figure 3.13d. Noticeably, the PL spectrum acquired at the interface (point 3) shows a broad and strong peak at 650 nm (1.91 eV). The observed shift in peak position and changes in peak shape cannot be simply due to the large laser spot size that picks up averaged information from an ~1 μm^2 area, as illustrated by the distinct difference between the PL spectrum acquired at the interface (point 3) and the superposition of spectra from pure MoS_2 and pure WS_2 (Figure 3.13e). Furthermore, PL intensity mapping at 650 nm (Figure 3.13g) reveals that this strong PL response is

localized at the lateral interface, and the intensity drops significantly at the intersections of these interfaces, which is consistent with the PL spectra presented in Figure 3.13e. The shift of the PL peak to intermediate energies near the interface can be explained as follows. Excitons near the interface have wavefunctions that overlap the other side, which causes a shift that gradually evolves to the excitonic peak on the other side. When the laser spot is focused on the interface, it generates excitons in the intermediate energies, resulting in the observed broad peak between the two pristine excitonic peaks. This observed peak contains contributions from excitons that have an electron predominantly on one side and the hole predominantly on the other side.

To further assess the localized interfacial effect, high-resolution PL microscope image from the heterostructure is acquired as shown in Figure 3.13h. Strong (around 40 times enhancement comparing to the pristine MoS_2 or WS_2) and highly localized (within 250 nm of FWHM) PL enhancement is clearly shown along the lateral interfaces. In comparison, the PL signals from pristine MoS_2 or WS_2 area are close to the background level from the SiO_2/Si substrate.

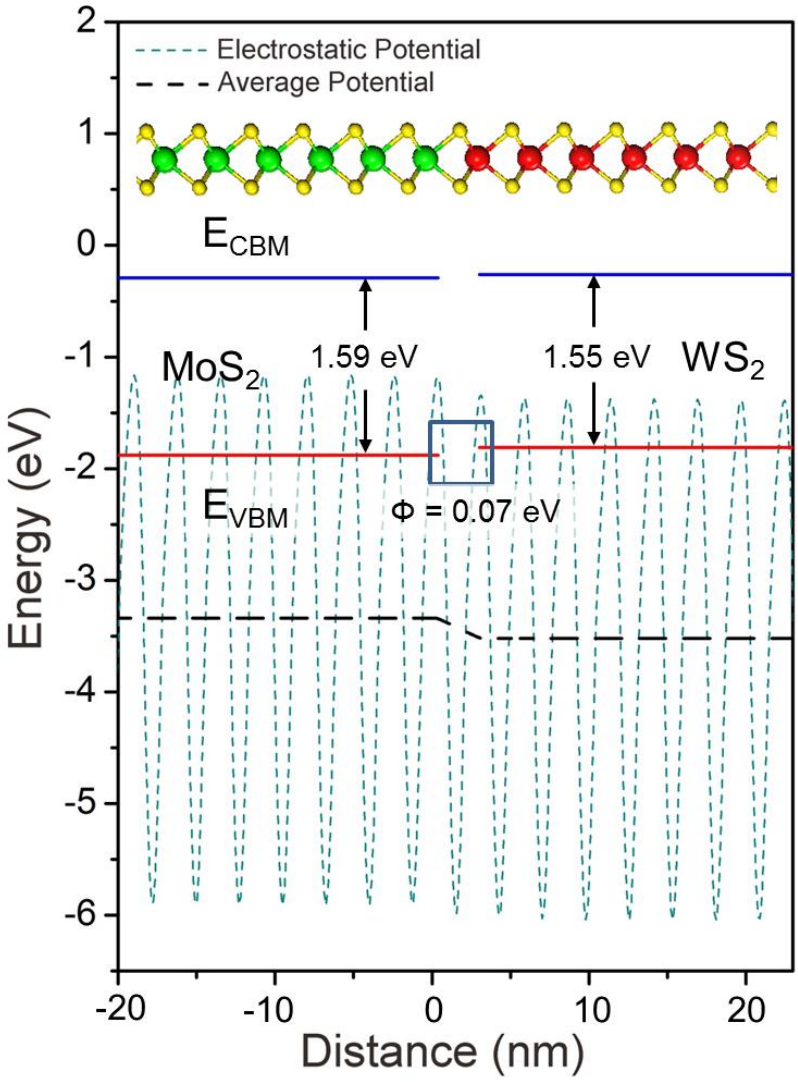

Figure 3.14: Band alignment in the lateral WS_2-MoS_2 heterojunction using electrostatic potential calculated by DFT. The band alignment was calculated using the electrostatic potential as a reference, where the change of the average electrostatic potential through the interface is calculated using a WS_2-MoS_2 heterojunction, and the valence-band-maximum (E_{VBM}) of the two semiconductors with respect to the electrostatic potential are calculated using the individual monolayer unit cell [106].

To explain such localized interfacial excitonic enhancement, I performed DFT calculations on the band alignment of the atomically sharp interface. The results are shown in as shown in Figure. 3.14. The band alignment is found to be a type II

heterojunction (staggered gap), similar to the result reported by in literature [107]. Although the bandgap mismatch is small, such small change of the bandgap occurs in a single atomic row (~ 3 Å in width), which gives a strong built-in electric field of over 2×10^8 N/C. Such strong built-in electric field at the atomically sharp interface may drive the free electrons and holes generated in the vicinity of the interface to recombine preferentially at the interface. Therefore, the interface serves as an enhanced excitonic recombination center, where the strong built-in electric field breaks the coherence of the electron-hole pairs generated in the vicinity of the interface, leading to their preferential recombination at the interface. In contrast, in the areas of "bulk" monolayer MoS_2 or WS_2, radiative recombination of excitons may be suppressed by non-radiative channels.

The lateral WS_2/MoS_2 heterostructures is further demonstrated to serve as intrinsic monolayer p-n junctions (Figure 3.13i and Figure 3.15) without external electrical tuning. The forward biased current is two orders of magnitude higher than the reversed one, implying a good rectification character unique in 2D electronics. Furthermore, under illumination, the lateral heterostructure shows clear photo-voltaic effect, which is also a solid evidence for the existence of a *p-n* junction. Such photo-voltaic effect is consistent with the band alignment calculations presented in Figure 3.14, where the bandgap is found to mismatch by a value of 0.07 eV, which is enough for the separation of electron-hole pairs and the occurrence of photo-voltaic effect in room temperature. An open loop voltage of 0.12 V and close loop current of 5.7 pA is obtained. This is the first time that the *p-n* junction and photo-voltaic effect are achieved in monolayer materials without external gating [88-90].

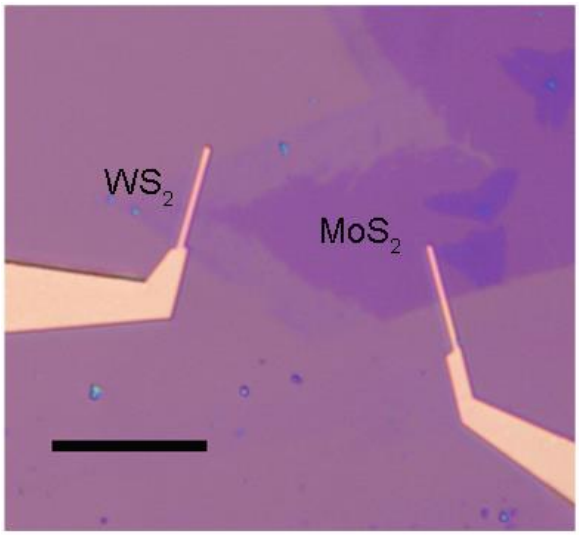

Figure 3.15: A typical optical image of device based on WS_2-MoS_2 in-plane heterojunction, where one electrode is on the outer layer WS_2 and the other one is placed on the inner layer MoS2. Scale bar: 10 μm.

In summary, this work have demonstrated the growth of high-quality vertical and lateral WS_2/MoS_2 heterostructures with clean and atomically sharp interfaces. The well-defined, sharp and clean interfaces in these heterostructure enable the capacity to explore new and controlled designs for 2D materials. The specific orientation relationships and ordering between the individual monolayer domains can lead to specific interface electronic properties which cannot be obtained in randomly assembled van der Waals hetero-materials. Such scalable methods to grow engineered 2D heterostructures could lead to interesting applications such as vertically stacked FET devices and planar monolayer devices. Combining both vertical and lateral 2D heterostructures opens up new possibilities to create novel architectures using 2D atomic layer building blocks.

CHAPTER IV

VACANCY-INDUCED FORMATION AND GROWTH OF INVERSION DOMAINS IN TRANSITION-METAL DICHALCOGENIDE MONOLAYERS

Transition-metal dichalcogenide (TMDC) monolayers are promising candidates for nanoelectronic and optoelectronic applications due to their direct-bandgap semiconducting nature and strong photoluminescence [45, 108-110]. TMDC monolayers in the 2H phase consist of two distinct elements alternating in the hexagonal honeycomb lattice, which leads to a 3-fold rotational symmetry. Therefore, domains of mirror symmetry, *i.e.,* inversion domains, emerge when the lattice is rotated by 60˚, which equivalently swaps the positions of the metal and chalcogen atoms in the hexagons [100, 111-113]. These inversion domains are connected by 60˚ grain boundaries (GB) that have been observed as intrinsic defects in CVD-grown TMDC monolayers [100, 111-113]. Such 60˚ GBs are predicted to be metallic [100, 112], acting as conductive channels inside the semiconducting monolayer and affect both the transport properties and exciton behaviors.

Experimental studies have shown that a single 60˚ GB can enhance the in-plane electrical conductivity and drastically quench the local photoluminescence [113, 114]. In order to fully develop the potential of TMDC monolayers for device applications, it is important to recognize the possible presence and the dynamics of these metallic 60˚ GBs in the monolayers. Furthermore, engineering such functional defects within the TMDC monolayer can help to tailor the performance of TMDC monolayers. A recent study

showed that 60˚ GBs in the 2H phase and phase boundaries between 1T/2H phases can be artificially created in a MoS_2 monolayer *via* the synergetic effect of electron irradiation and *in-situ* heating [115]. The *in-situ* heating generates thermal instability within the lattice and the high-energy electrons were used to trigger the phase transition *via* electron accumulating [115, 116].

However, I found that thermal annealing an exfoliated free-standing MoS_2 monolayer at 700 ˚C without simultaneous electron irradiations can induce high density of triangular inversion domains with size up to 40 nm^2, as shown in Figure 4.1a and 4.1b. The *ex situ* thermal annealing experiment was performed on a monolayer MoS_2 prepared by mechanical exfoliation from its bulk form. Before thermal annealing, I examined the sample in the electron microscope under low-dose imaging conditions to ensure its single crystal nature. The sample was then taken out for thermal annealing and put back into the microscope after thermal annealing. A high density of large triangular inversion domains was observed throughout the whole monolayer. Imaging on this sample before and after annealing was done at low-dose settings, where special care was paid in order to prevent any structural damage to the sample during imaging.

Importantly, these triangular inversion domains have the same 60˚ GB structures as the intrinsic 60˚ GBs observed in CVD-grown TMDC monolayers, as shown in Figure 4.1c and 4.1d [100, 111]. A small amount of oxygen was present during the annealing procedure, which facilitates the formation of sulfur vacancies by decreasing their formation energy and was found to be important for the creation of inversion domains. I noticed that the 60˚ GB structures generated during the annealing experiment are slightly different from those reported in the previous literature *via* the combination of *in-situ*

heating and electron irradiation [115], where no massive loss of atoms was observed during the dynamical process. This indicates that the dynamics and formation mechanism of the 60˚ GBs and the inversion domain *via* thermal annealing alone may be different from the previous study [115, 116].

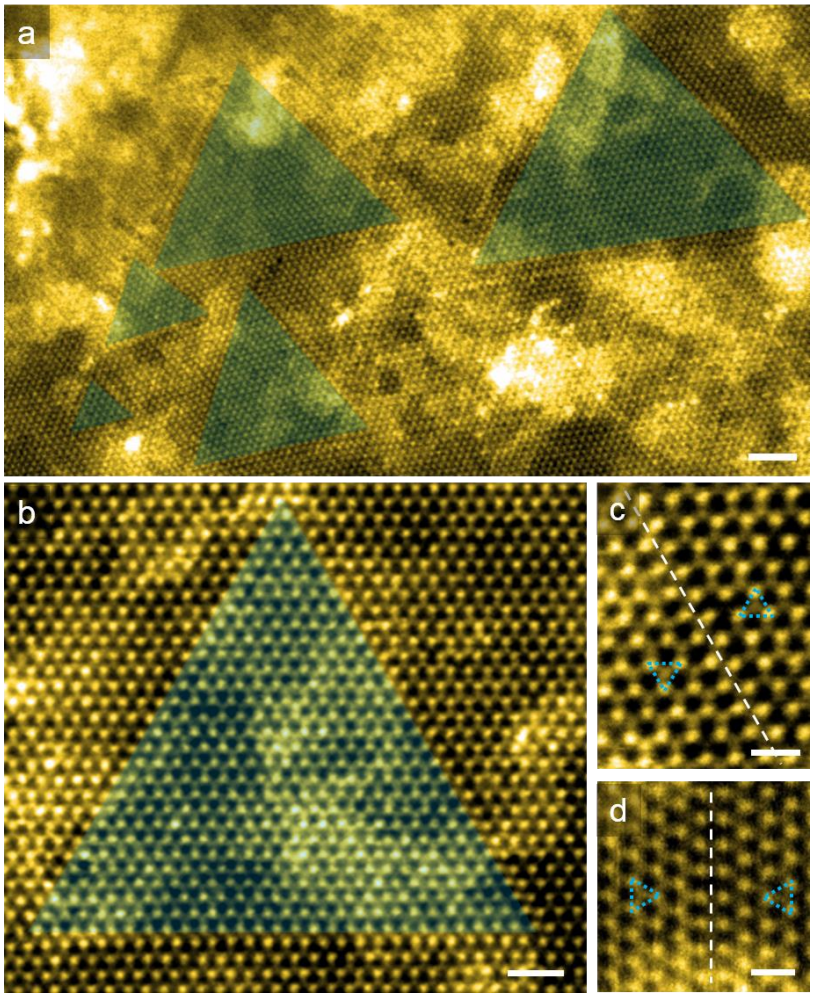

Figure 4.1: Formation of inversion domains in monolayer MoS_2 *via* thermal annealing. (a) Large scale Z-contrast image of the *post-annealed* monolayer MoS_2 sample. A large amount of inversion domains with various sizes is found, as highlighted by the semi-transparent triangles. The image is taken at a dose rate of 1.2×10^5 e/nm^2• s with a total dose of 2.0×10^6 e/nm^2. (b) Enlarged Z-contrast image showing the atomic structure of the triangular inversion domain. The size of this inversion domain is ~ 40 nm^2. No severe damage is found in the lattice except for S vacancies. The imaging dose rate is approximately 4.8×10^5 e/nm^2• s with a total dose of 8.0×10^6 e/nm^2. (c, d) Z-contrast images of the 60˚ grain boundaries in the large triangles, with the same atomic structure as those described in the main text. The dash triangles indicate the orientations of the

domains while the dashed lines point out the location of the 60˚ grain boundaries. Scale bars: (a) 2 nm; (b) 1 nm; (c, d) 0.5 nm.

Electron irradiation at room temperature on TMDC monolayers generates chalcogen vacancies and provides energy for them to undergo structural evolutions. Structural evolution induced by electron irradiation has been demonstrated as an effective means to explore dynamical processes that span large time scales under typical thermodynamic conditions [107, 115, 117-124]. In order to study the formation mechanism of the inversion domain and 60˚ GBs, I performed STEM sequential Z-contrast imaging with high electron dose at room temperature on a pristine monolayer $MoSe_2$ sample that has not been annealed at high-temperature, as the second experiment. Such sequential imaging direct track the dynamical motions of the defects generated by the electron beam. Monolayer $MoSe_2$ was chosen as a representative material of the TMDC family for this study mainly because it has higher threshold against knock-on damage and better image visibility of Se vacancies, which allows for better tracking of the dynamical behavior of Se vacancies.

The intensity in Z-contrast imaging is related to the atomic number of the imaged species [72], with the Se_2 columns brighter than the Mo atoms in a pristine monolayer $MoSe_2$ (Figure 4.2a). Mono-selenium vacancies (V_{Se}), as shown in Figure 4.2a, and di-selenium vacancies (V_{Se2}) can be distinguished based on their image intensity. This enables us to directly track the dynamical motions of Se vacancies with single atom sensitivity. As will be shown later, electron irradiation generates the same inversion domains as those obtained by thermal annealing, which suggests that the primary role of the electron beam is to provide energy to overcome the activation barriers, *i.e.* possible

charging does not play a significant role as it does in the case of the H-to-T phase transition discussed in Ref. 99.

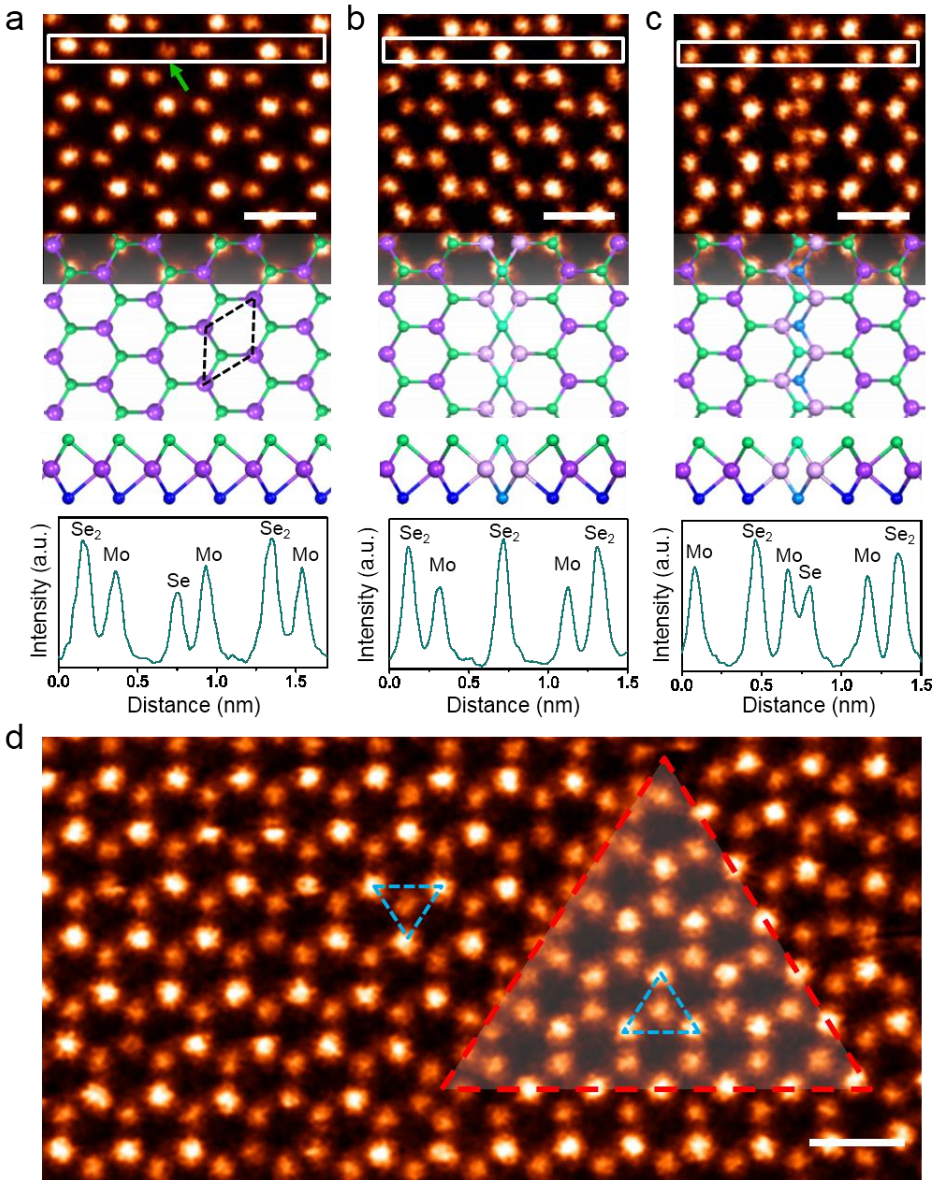

Figure 4.2: Atomic structure of mono-selenium vacancy, 60˚ grain boundaries and inversion domain embedded in pristine monolayer $MoSe_2$. (a) High resolution Z-contrast image of the pristine lattice of monolayer $MoSe_2$ with atomic model overlaid. The green arrow points to a mono-selenium vacancy that can be directly identified by its lower contrast than the Se_2 column. The black dashed diamond indicates the unit cell of the pristine lattice. (b, c) Z-contrast image and the corresponding structural model of the 4|4P (b) and 4|4E (c) 60˚ grain boundaries. The side views of all the models are provided below. The line intensity profiles of the mono-selenium vacancy and the grain boundaries

are provided at the bottom of each panel, respectively. The atoms in the grain boundary regions are highlighted in a slightly different color. (d) A typical triangular inversion domain embedded within the $MoSe_2$ monolayer. Scale bars: 0.5 nm.

A close examination of the atomic structure of the 60˚ GBs reveals a slight change in chemical stoichiometry as compared to the pristine lattice, suggesting the creation of such 60˚ GBs may involve complex motions of vacancies. Figure 4.2b shows the Z-contrast image of a 60˚ GB containing 4-fold rings that share points at Se_2 sites, denoted as 4|4P [100], where the inversion domain is mirror-symmetric with the original lattice along the GB. Figure 4.2c shows another type of 60˚ GB which includes strings of 4-fold rings with edge sharing at Mo-Se bonds, denoted as 4|4E [100], where the inversion domain is shifted by half of the primitive lattice vector along the GB away from the mirror-symmetric positions. At the 4|4P 60˚ GBs, the Mo atoms retain the 6-fold coordination as in a pristine lattice, whereas the coordination of Se atoms with Mo atoms changes from 3-fold to 4-fold. Similarly, at the 4|4E 60˚ GBs, the Mo atoms have 5-fold coordination instead of 6-fold as in the pristine lattice, while Se atoms maintain the same 3-fold coordination. The change in coordination alters the local chemical stoichiometry at GB regions, with Mo_4Se_6 ($MoSe_{1.5}$) along the 4|4P 60˚ GBs and Mo_3Se_5 ($MoSe_{1.67}$) along the 4|4E 60˚ GBs, when only atoms along the GB with changed bonding conditions are considered. Both GBs show Se deficiency as compared to the pristine $MoSe_2$ stoichiometry. This feature indicates that the formation and expansion of such GBs within the pristine lattice inevitably involve the presence of Se vacancies [125]. Due to the 3-fold symmetry of the lattice in $MoSe_2$, the 60˚ GBs always appear in triangular shapes when created within the pristine monolayer. Ideally, two mono-selenium vacancies are needed if the 60˚ GB expands by one unit cell, since the GB could increase

by 4 unit cells in length (due to the two edges around the corners in the triangle) during the expansion, as shown in Figure 4.3. I note that the GBs participating in the growth of inversion domains have different structure from the ones observed in the previous literature [126].

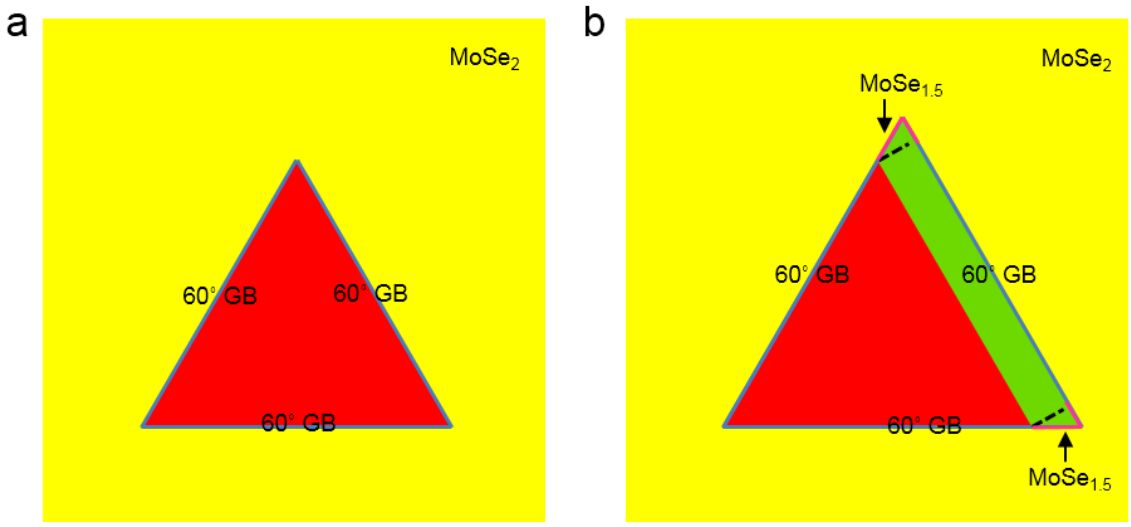

Figure 4.3: Stoichiometric analysis of a 4|4P 60° GB migrating by one unit cell. (a) Schematic of a triangular inversion domain embedded in the $MoSe_2$ lattice with three 60° GBs. The GBs are highlighted by blue lines. The triangular inversion domain is highlighted in red. Note that the chemical stoichiometry for the 4|4P 60° GB is different from the pristine lattice, which is Mo_4Se_6 ($MoSe_{1.5}$). (b) Schematic of the inversion domain after one of the GBs migrates by one unit cell. The increased region of the inversion domain and the increased length of the GB is highlighted in green and pink, respectively.

Figure 4.2d shows an inversion domain, produced by prolonged electron irradiation, which contains the two types of 60° GBs described above. The inversion domain is formed from the agglomeration of Se vacancies activated by electron irradiation. Prolonged exposure of the $MoSe_2$ monolayer to electron irradiation generates new Se vacancies [119, 127, 128], while the existing ones can also be activated to evolve. Se vacancies are generated mainly *via* ionization damage under my experimental conditions,

as the knock-on damage threshold for Se atoms in monolayer $MoSe_2$ is ~190 kV [119, 128]. I found that the formation rate of Se vacancy is proportional to the total electron dose and insensitive to the electron dose rate, as shown in Figure 4.4.

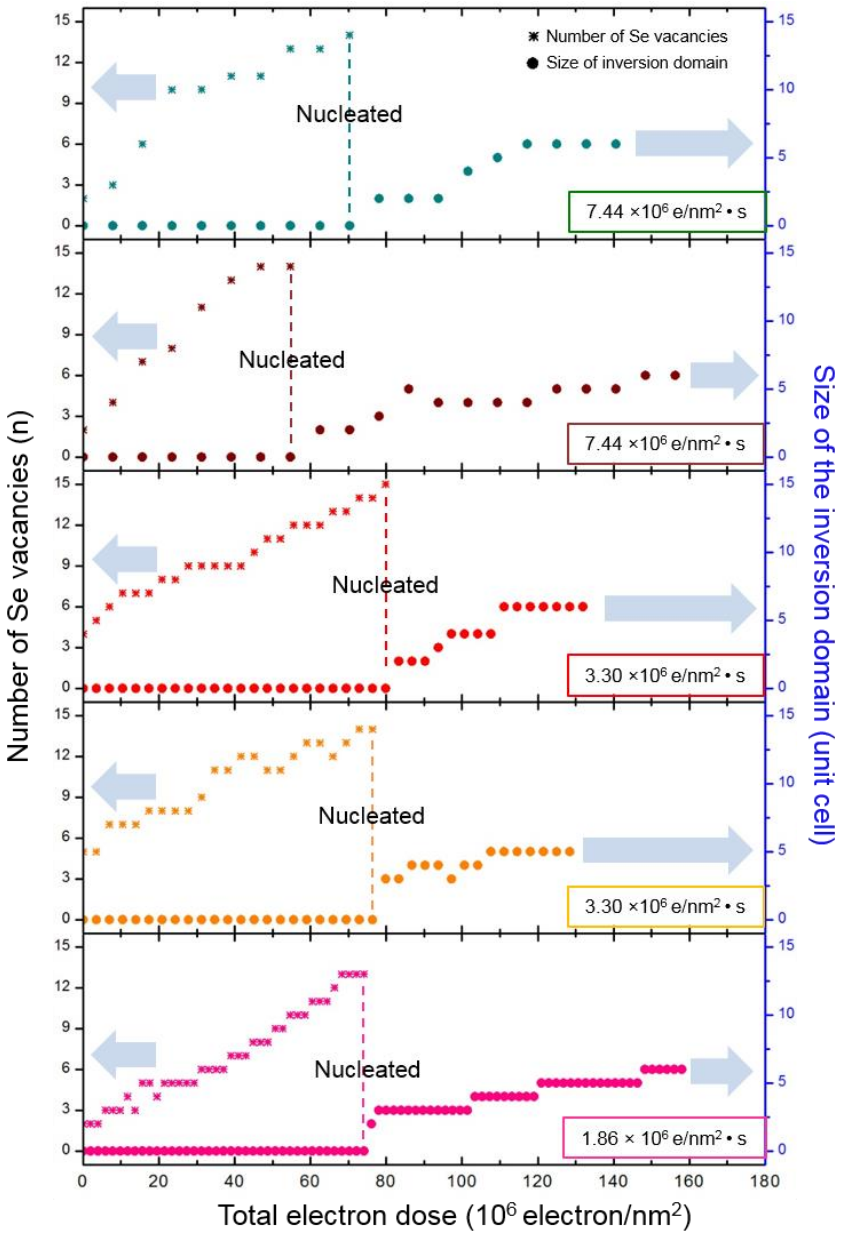

Figure 4.4: Relationship among the creation of Se vacancies, electron dose and the formation of the inversion domain. Data from five different experiments are presented. The number of Se vacancies and the size of inversion domain as a function of the total electron dose are plotted in asterisk and solid circles, respectively. The electron dose rate is controlled by the pixel size while keeping the same dwell time. The Se vacancies are

counted within a 2.5×2.5 nm^2 square containing the nucleation site as the center. The arrows indicate the corresponding vertical axis for each data set.

I find that the randomly located Se vacancies can migrate over a few unit cells under the electron excitation. My DFT calculations show that the migration barrier for Se vacancy is relatively low (~ 2eV, as shown in Figure 4.5), which can be easily overcome by the energy transferred from the electron beam [117, 128]. Previous study have shown that electron irradiation of monolayer MoS_2 drove sulphur vacancies to form extended line defects [129]. Such phenomenon is also observed in my experiment on $MoSe_2$. Detailed atom-by-atom tracking of the migration process of multiple Se vacancies (Figure 4.6) reveals that they preferentially agglomerate into lines and reconstruct rather than undergo random walks [130], as shown in Figure 4.7a. Such agglomeration of Se vacancies *via* atomic migration also leads to the formation of an extended line defect with a single row of Se atoms missing (such structure is abbreviated as SL below), which lowers the energy of the system [129]. Both the experimental image and DFT calculations indicate that the missing Se atoms induce contraction between the remaining Mo atoms along the SL defect due to their unsaturated bonds.

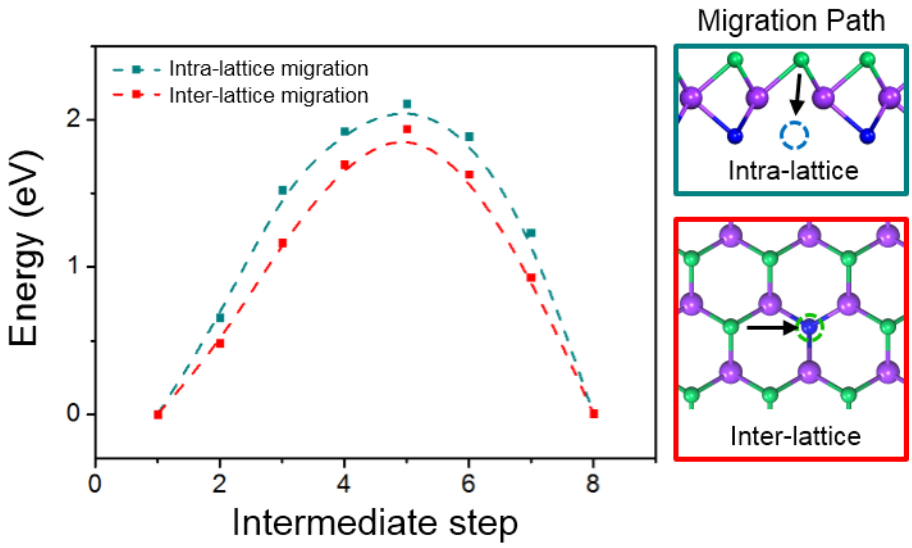

Figure 4.5: Energy barrier for the intra- and inter-lattice migration of a mono-selenium vacancy in monolayer $MoSe_2$. Both of the barriers are estimated to be around 2 eV, which can be excited by electron irradiations.

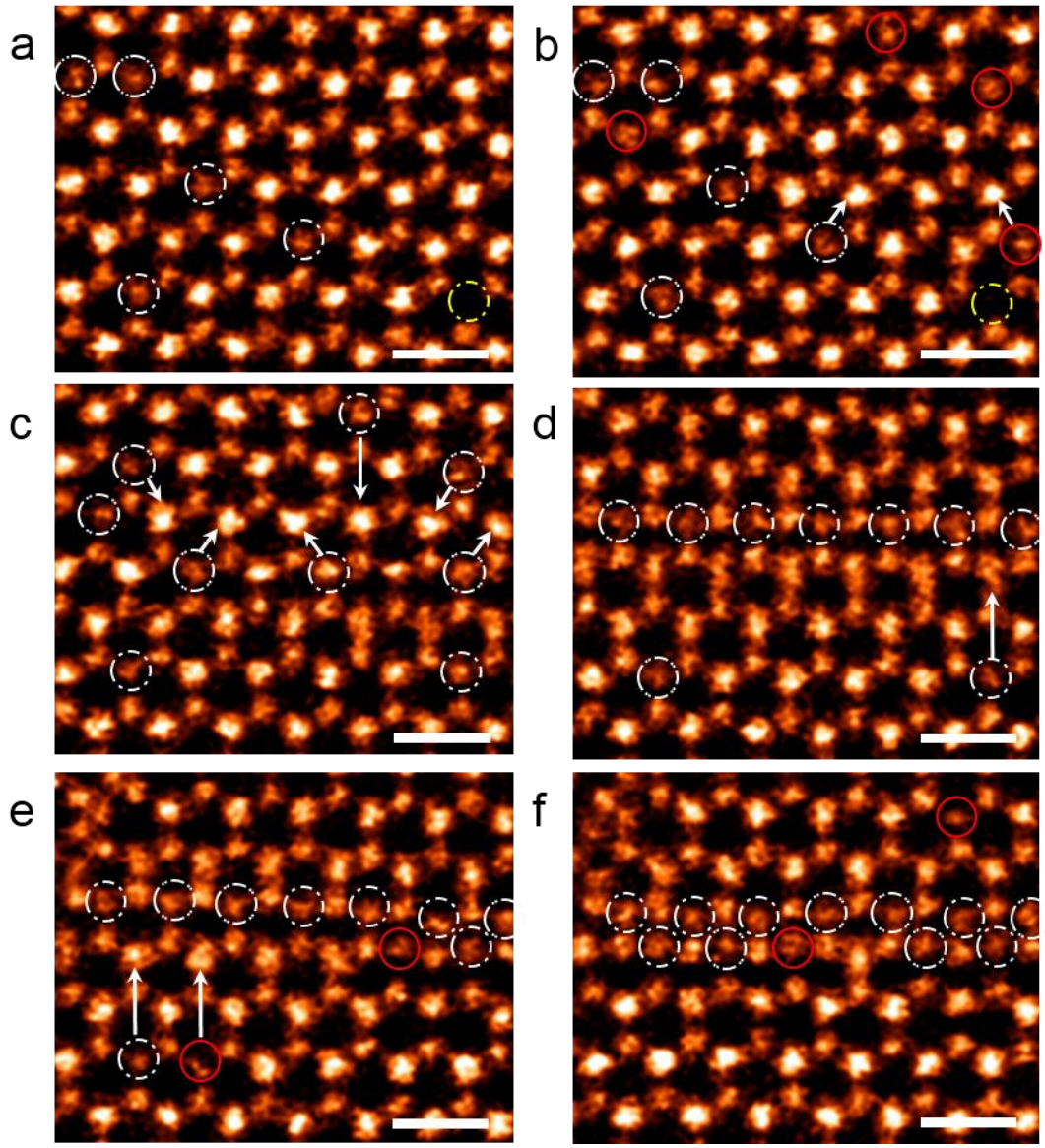

Figure 4.6: Formation of SL and 4|4E GB-like line defects in monolayer $MoSe_2$ *via* migration under electron-beam excitation. (a-f) Sequential Z-contrast images of the process from random Se vacancies (a) to SL line defect (d), and then to 4|4E GB-like line defect (f). The white dashed circles indicate mono-selenium vacancies, yellow for di-selenium vacancy, and red circles for the new mono-selenium vacancy created by the electron beam or migrated from the nearby region. The white arrows indicate the migration path of the Se vacancy. Scale bars: 0.5 nm.

As more Se vacancies nearby continue to migrate into the SL defect, instead of growing longer in length, I observed the defect complex reconstructs into irregular strings

of 4-fold rings (abbreviated as 4|4E GB-like structure, which is a highly strained 4|4E 60˚ GB, as discussed below) and no longer maintain the hexagonal rings (Figure 4.7b). Such reconstruction is due to the lower formation energy of the 4|4E GB-like structure than the SL defect at certain critical Se vacancy concentration, as demonstrated in the previous study [129]. Therefore, under continuous electron excitation, the SL defects would more likely develop into the 4|4E GB-like structure than continuously grow in length after reaching the critical length (approximately 8 unit cells) [129]. The formation of the 4|4E GB-like structure further contracts the surrounding Mo sub-lattice, as shown by the decreasing Mo-Mo distance (Figure 4.7b). As shown in Figure 4.8, my DFT calculations demonstrate that the presence of the SL and 4|4E GB-like line defect introduces new localized defect states within the band gap. Therefore, both the SL defect and the 4|4E GB-like structure show localized metallic behavior.

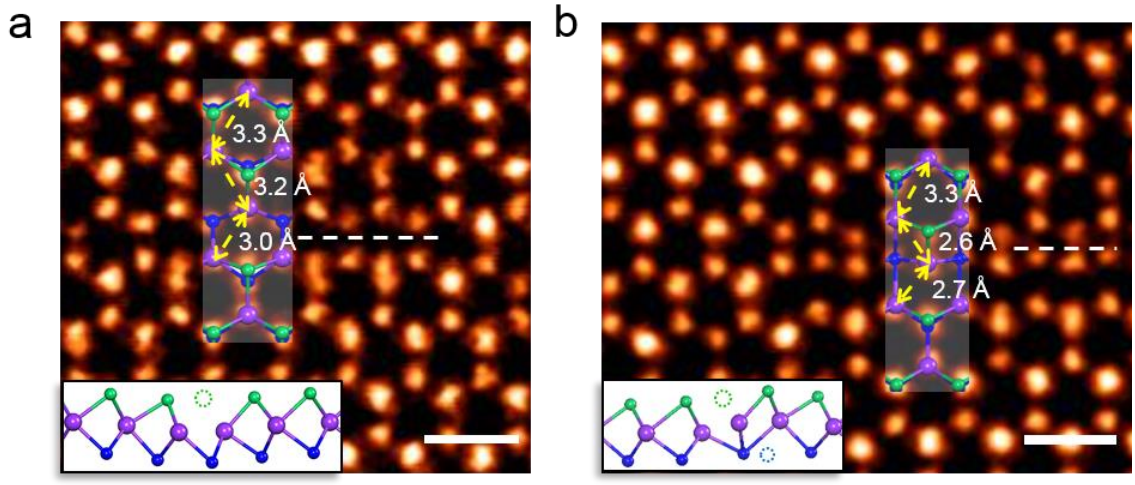

Figure 4.7: Agglomeration of Selenium vacancies into line defects in monolayer $MoSe_2$. (a) STEM Z-contrast image of the SL line defect with the DFT-optimized structure overlaid. Inset: Side view of the structure model. The nearby Se_2 columns are slightly misaligned. (b) STEM Z-contrast image of the 4|4E GB-like structure (highly-strained 4|4E 60˚ GB) evolved from the SL line defect, which contains deformed strings of 4-fold rings. The white dashed lines indicate the centers of these defects and the yellow dashed

arrows highlight the bond length of the Mo sublattice in the defect regions. Scale bars: 0.5 nm.

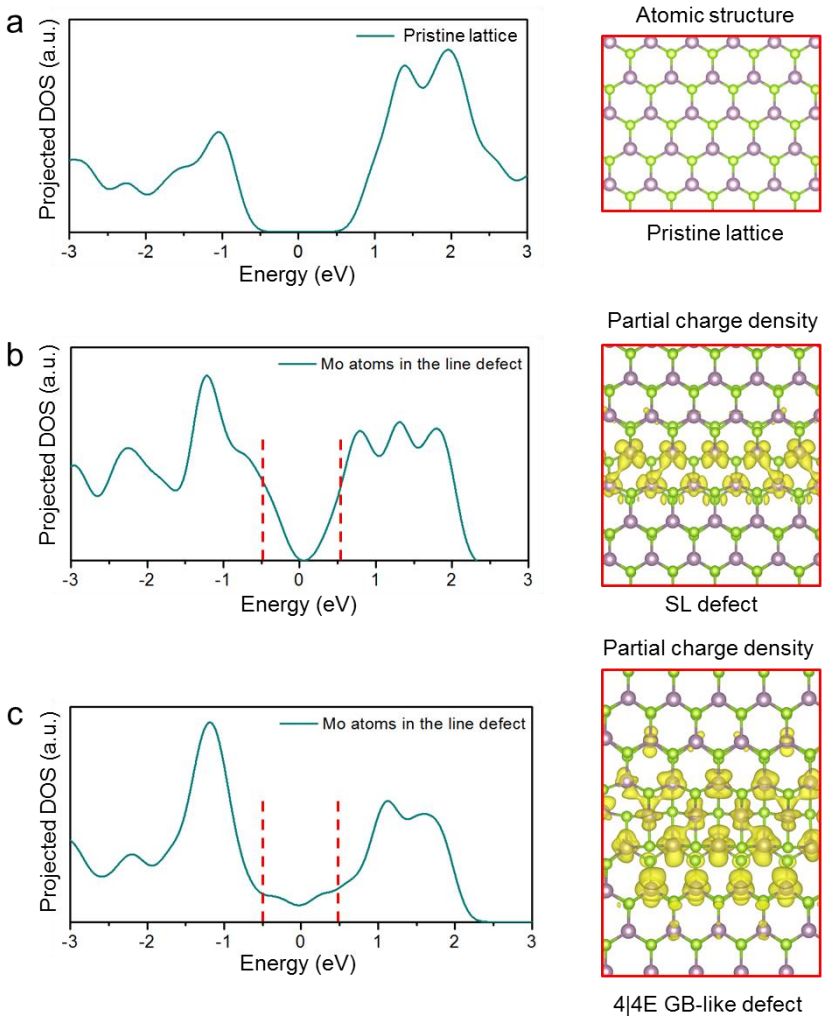

Figure 4.8: Modification of electronic structure in line defects. (a-c) Density of states of the pristine $MoSe_2$ (a), projected density of state of the atoms in the SL line defect (b) and the 4|4E GB-like line defect (c). The figures on the right show the partial charge density of these defect-induced new states (regions highlighted by the dashed red lines in (b) and (c)), indicating the metallic feature are localized around the defect regions.

I find that the nucleation of inversion domain usually occurs after the accumulation of a certain amount of Se vacancies (~15 Se vacancies within the nucleation region, Figure 4.4). Figures 4.9a-4.9c show the nucleation process of the inversion domain from the 4|4E GB-like structure. The nucleation was triggered by the Se vacancies generated,

either by irradiation damage or migration, at one end of the 4|4E GB-like structure. Figure 4.9a highlights the region where three Se atoms were removed. The remaining Mo atoms in this region are, therefore, pulled towards each other due to the absence of Se atoms, as highlighted by the dashed rectangle in Figure 4.9b, leading to local lattice shrinkage. To further estimate such local lattice shrinkage observed in the experiment, I performed DFT calculations in a supercell that contains the defect structure as a function of lattice shrinkage. I used the length ratio ***A/B*** to indicate the lattice shrinkage, where *A* and *B* are the distance between two perpendicular pairs of Mo atoms defined in the deformed regions before and after the nucleation process and the lattice, where the schematic diagrams are shown in the inset of Figure 4.10a. I only considered the lattice shrinkage along the armchair direction since the deformation in the 4|4E GB-like structure mainly contracts the lattice in this direction [129].

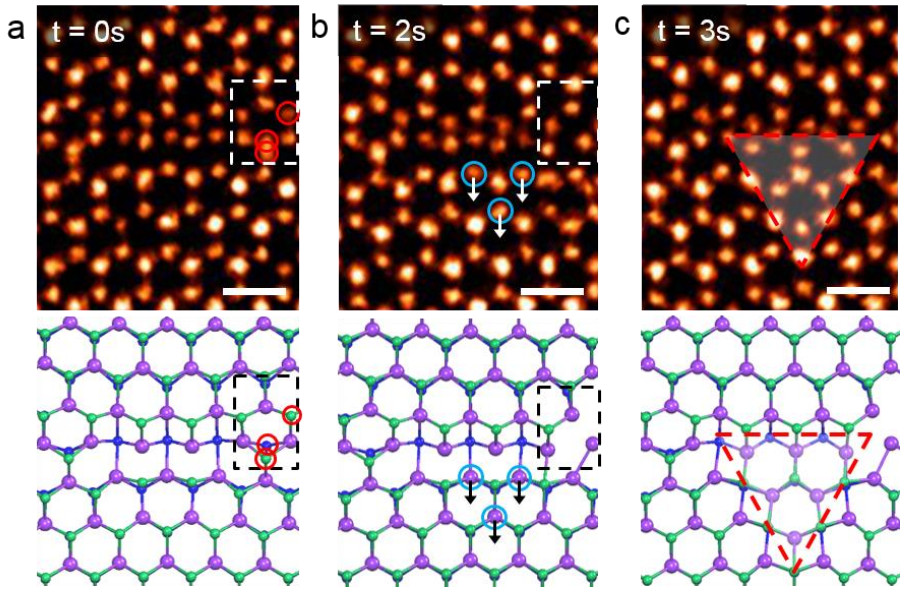

Figure 4.9: Nucleation of the inversion domain from 4|4E GB-like structure. (a-c) Sequential Z-contrast images of the nucleation process. The atomic models are provided below. The dashed rectangles highlight the corner of the defect where Se vacancies are generated, which leads to structural reconstructions. The red circles in (a) highlight the Se atoms that are being removed in the next frame. The arrows in (b) indicate the

displacement direction of the Mo atoms during the nucleation of the inversion domain. Scale bars: 0.5 nm.

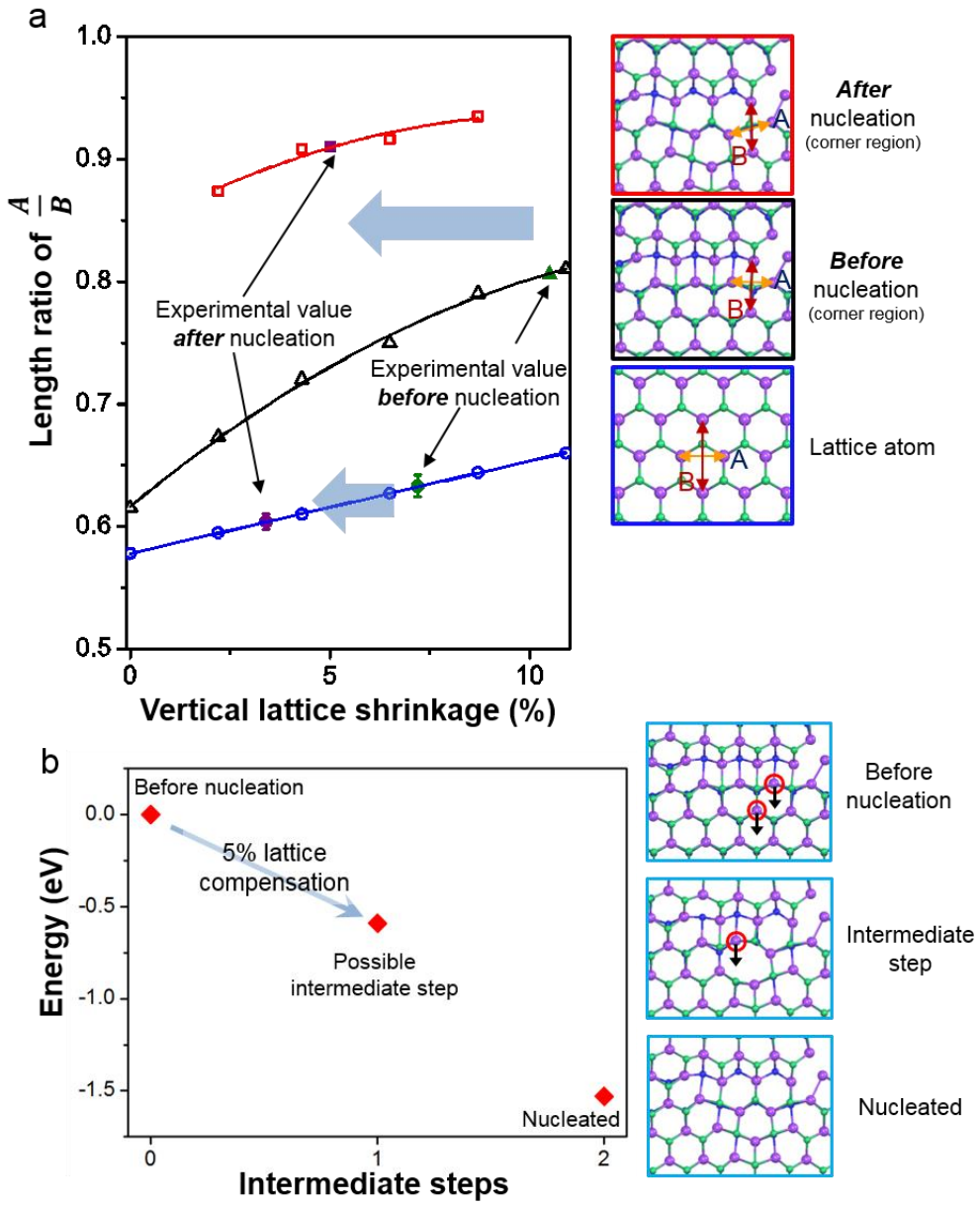

Figure 4.10: DFT calculations of the nucleation process of the inversion domain. (a) **A/B** ratio of Mo sub-lattice in different regions, where *A* and *B* are defined in the corresponding insets, as a function of lattice shrinkage. The blue, black and red open symbols are the DFT calculated values corresponding to the atoms in lattice (blue), near the 4|4E GB-like structure before (black) and after the nucleation (red), respectively. The lines linking the symbols are polynomial fitting of the calculated data points. The experimental values are highlighted in green and purple, respectively. The error bar of the **A/B** ratio of the lattice atoms is the standard deviation from all the Mo sub-lattice close to

the defect structure. (b) Energy landscape of the nucleation process. The nucleation of the inversion domain partially releases the local lattice shrinkage and lowers the system energy. Insets on right: atomic structure of the possible steps of the nucleation process. The atoms that undergo displacements in each step are highlighted in red circles.

Figure 4.10a shows the results from the DFT calculations. By fitting the ***A/B*** ratio obtained from the experimental image (Figure 4.9b and 4.9c), I find that the whole 4|4E GB-like structure and its nearby lattice region undergoes a large compression prior to the nucleation of the inversion domain, presumably induced by the collective out-of-plane structural reconstructions of the Se vacancies [129, 131], which could make the whole structure unstable. In response to being compressed by the nearby defect, the Mo atoms (in this case, three Mo atoms) can undergo displacements to release the strain (blue circles in Figure 4.9b). The subsequent reconstructions form two 4|4P 60˚ GBs and release the strain in the 4|4E GB-like structure, which relaxes into a stable 4|4E 60˚ GB. Due to the 3-fold symmetry of the hexagonal $MoSe_2$ lattice, the inversion domain could only be stably formed in a triangular shape within its original lattice. As a consequence, the nucleation of the inversion domain reduces the shrinkage of the lattice and the strain is relaxed after the nucleation (Figure 4.10a).

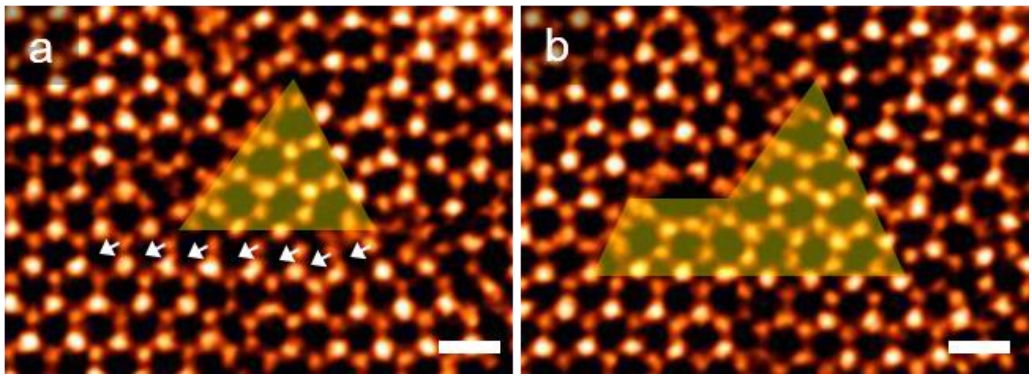

Figure 4.11: Intermediate step of the 60˚ grain boundary migration. (a, b) Z-contrast images of the 60˚ grain boundary before (a) and after migration (b). The migration follows the same procedure as described in the main text. An 8-member-ring serving as a kink in the middle of the grain boundary is observed during the displacements of the atoms, suggesting that the atoms undergo displacements one after another. Scale bars: 0.5 nm.

Figure 4.10b depicts the nucleation of the inversion domain in energy landscape. Although the process happens in a time scale that is much faster than the imaging rate (~1 s per frame), the Mo atoms are expected to undergo displacements one after another. The inset in Figure 4.10b shows a possible intermediate step of the nucleation process. The intermediate step shows two Mo atoms undergo displacements in the same direction to form a stable 8-member ring. Such 8-member ring is indeed observed during the migration of the 60˚ GBs, as indicated in Figure 4.11. My DFT calculations show that such displacement could lower the energy of the system due to the release of the lattice shrinkage. The 5% supercell relaxation for the intermediate state mimics the local relaxation that occurs as indicated in Figure 4.10a. As a result, calculation of the nucleation barrier is not practical in this case. After the displacement of the remaining Mo atom, the inversion domain formed which is more stable than the intermediate state. 4|4P and 4|4E 60˚ GBs (Figure 4.9c) are formed as a result of the nucleation of the

inversion domain. I also find that these two types of 60˚ GBs can indeed transform into each other *via* shifting half of a unit cell with the presence of Se vacancies nearby (Figure 4.12).

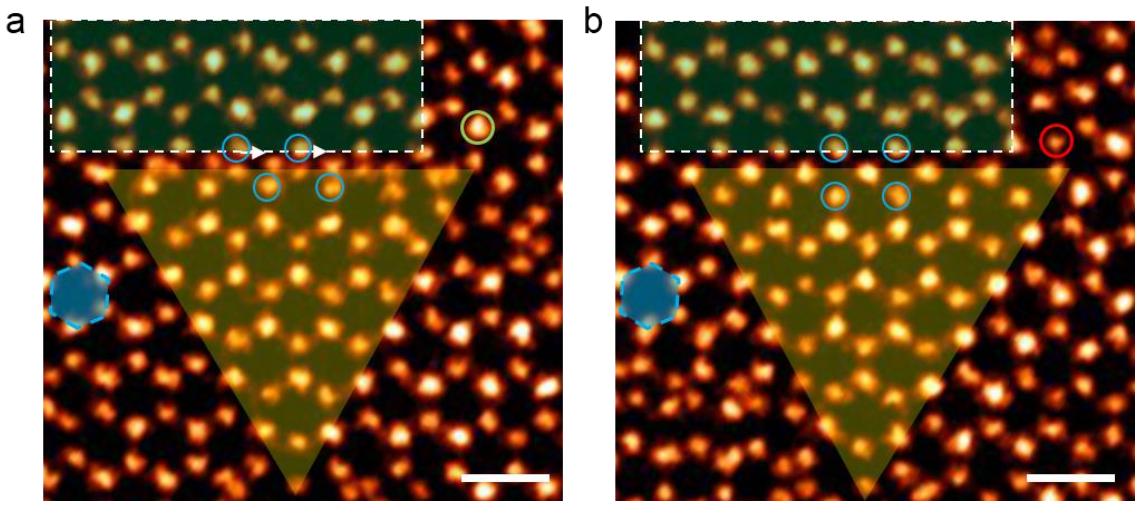

Figure 4.12: Transition between the two types of 60˚ grain boundaries in the presence of nearby Se vacancies. (a, b) Z-contrast images of a 60˚ grain boundary before (a) and after the lattice shifting (b). The light green and red circles highlight the Se_2 column and the subsequent Se vacancy, respectively, which induces lattice shifting due to the lattice reconstruction. The shadowed green rectangles highlight the region being shifted. The blue circles indicate the Mo atoms at the boundary before and after the shifting. The white arrows point out the displacements of the Mo atoms. The blue shadowed hexagons are provided as a reference for the positions between the two images. Scale bars: 0.5 nm.

The 4|4P 60˚ GBs are observed to migrate more frequently than the other type of GBs under electron-beam excitation. Figures 4.13 & 4.14 show a complete migration process of a 4|4P 60˚ GB, which leads to the growth of the triangular inversion domain. Figure 4.13a shows the initial state of a triangular inversion domain with three 60˚ 4|4P GBs. The migration is also found to be initiated by the formation of Se vacancies (highlighted by the green circle in Figure 4.13a and red circles in Figure 4.13b after generation of the vacancies) at the corner region of the triangle, which is needed for the

expansion of the GBs with Se deficiency. The Se deficiency leads to a slight displacement of the nearby Se column, providing necessary space for the highlighted Mo atom to displace, as illustrated by the arrow in Figure 4.13a. Such displacement of the Mo atom could then trigger the neighboring Mo atoms in the GB region to undergo displacements along the same direction one by one (Figure 4.13b). Figure 4.13d shows the final state after the displacements and corresponding reconstructions, where the inversion domain expands *via* the 60˚ GB migration. Figure 4.14c shows an overlapped image between the initial (Figure 4.14a) and final structure (Figure 4.14b) for another 60˚ GB that migrates for one unit cell, elaborating clearly that the expansion of the inversion domain involves a di-selenium vacancy, consistent with the stoichiometry analysis (Figure 4.3). In general, the triangular inversion domain can grow along any of its edges through the same GB migration process (Figure 4.15). Similar vacancy-induced nucleation and growth of inversion domains are also observed on monolayer MoS_2 with lower image quality, as shown in Figure 4.16.

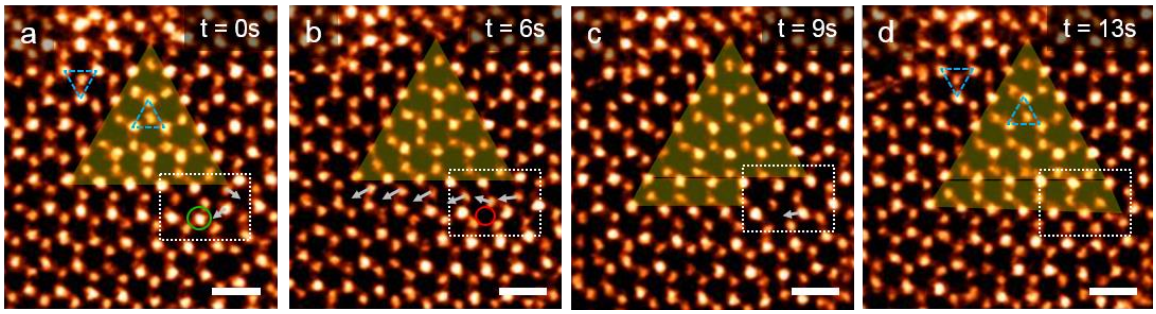

Figure 4.13: Growth of the inversion domain and migration of the 4|4P 60˚ grain boundary. (a-d) Sequential STEM Z-contrast images of the migration of a 60˚ grain boundary which leads to the growth of the inversion domain. The dashed rectangle highlights the corner structure of the triangular inversion domain. The green circle in (a) highlights the Se_2 column that is removed in the next frame. The red circle in (b) indicates the as-formed Se vacancy. The white arrows indicate the displacement direction of the atoms. The overlaid yellow triangles indicate the size of the inversion domain. The two dashed blue triangles represent the mirror symmetric orientations. Scale bars: 0.5 nm.

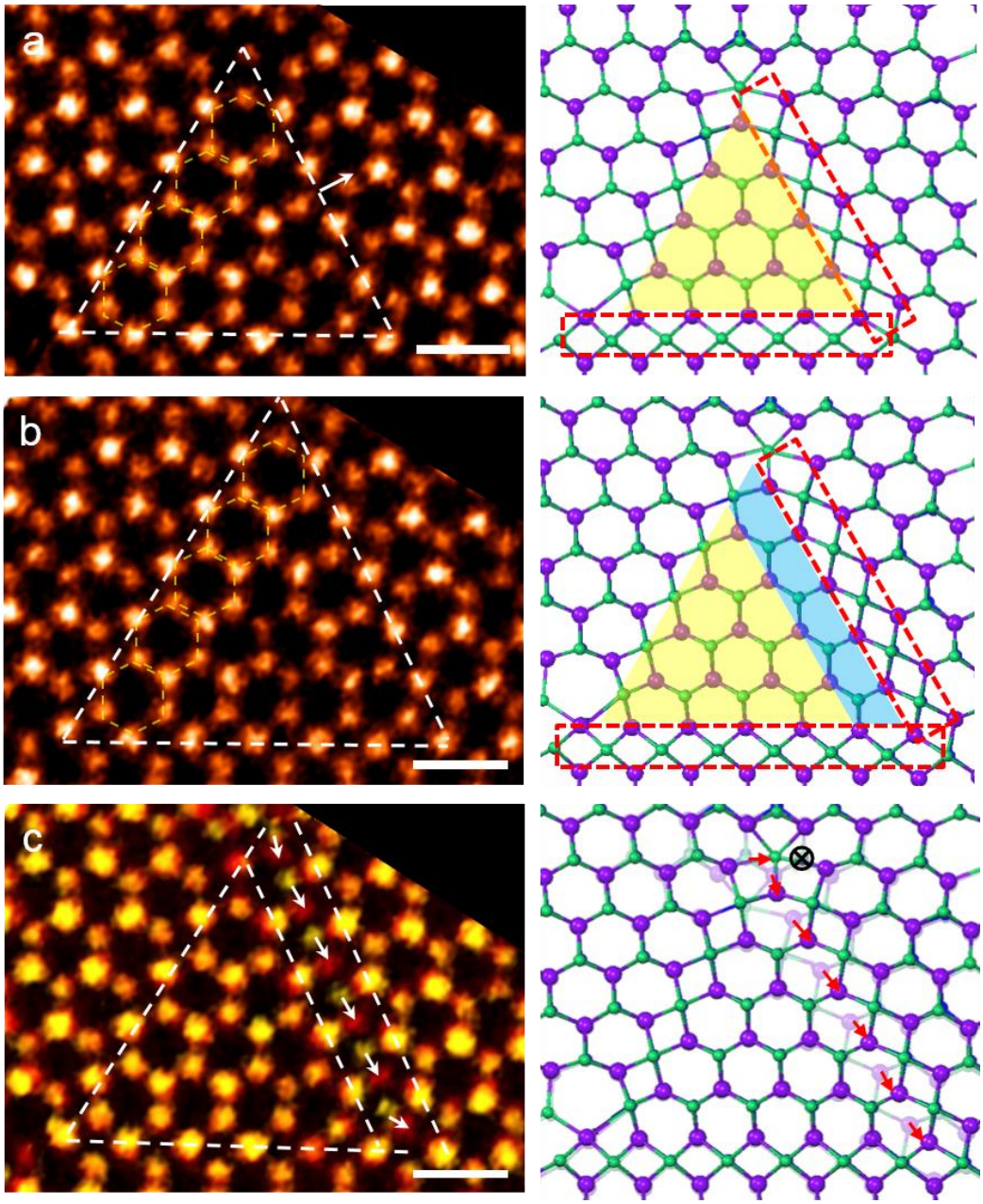

Figure 4.14: Overlapped image between the initial and final structure of a 4|4P 60˚ GB migrating for one unit cell. (a, b) Z-contrast images of a 4|4P 60˚ GB before (a) and after (b) migration. The atomic models are provided next to the images. The white dashed lines in the Z-contrast images and red dashed rectangles in the atomic models highlight the GB regions, respectively. The blue trapezoid in the atomic model indicates the expanded area of the inversion domain. (c) Overlapping of (a) and (b) with different color schemes. The initial image is colorized in yellow while the final one in red. The red arrows represent the displacement of the atoms. A di-selenium vacancy is needed (indicated by the black circle) for the GB to migrate one unit cell within the pristine lattice. Scale bars: 0.5 nm.

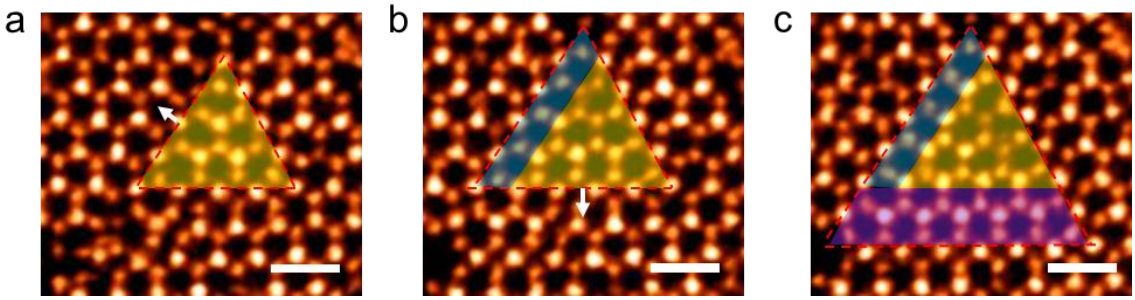

Figure 4.15: Expansion of the inversion domain along different directions. (a-c) Sequential Z-contrast images of an inversion domain expanding along different directions, which is realized by the 4|4P GB migrations. The blue and purple trapezoids indicate the increased area of the inversion domain after the GB migration. In principle, the inversion domain can expand through any one of its three 4|4P GBs, as described in the main text. Scale bars: 0.5 nm.

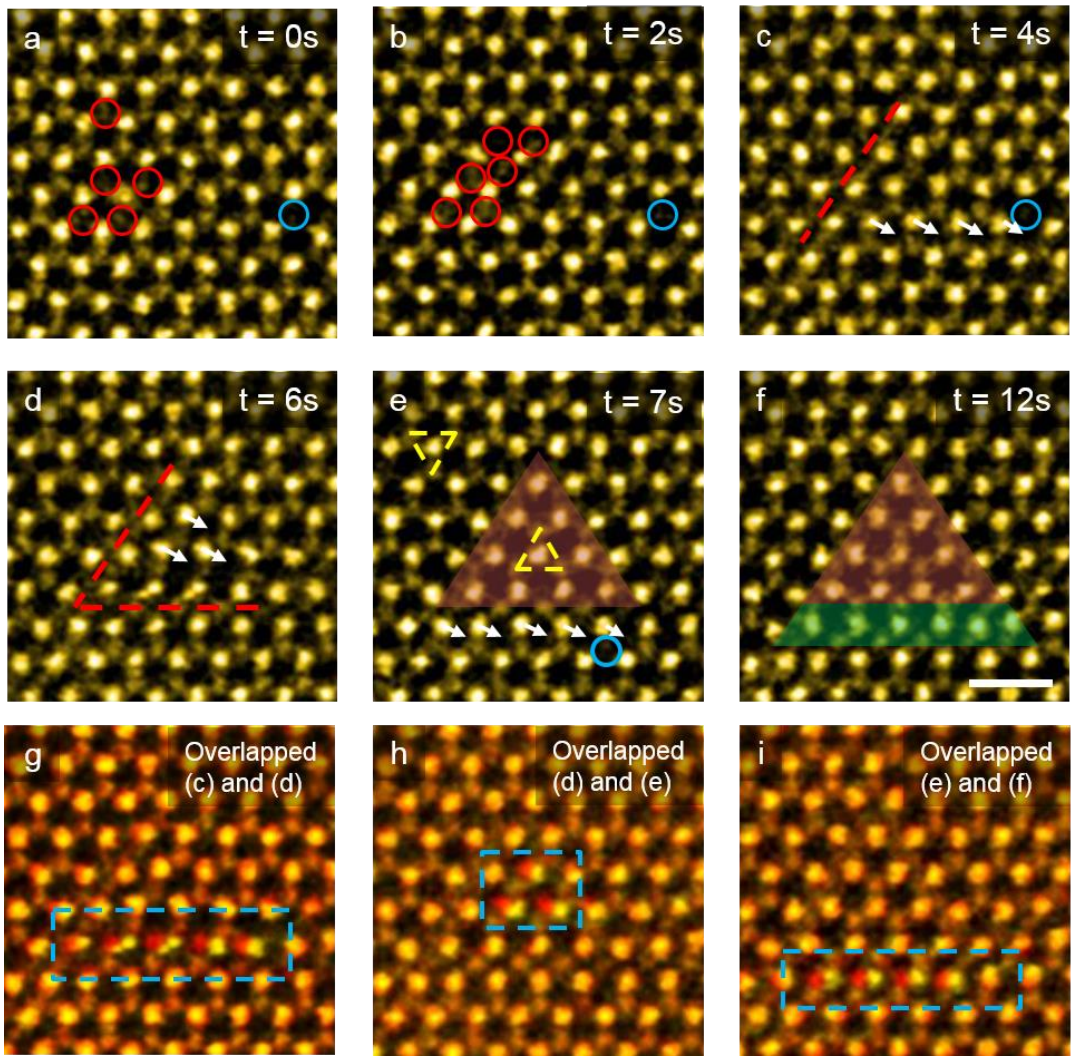

Figure 4.16: Sulphur vacancy-induced nucleation and growth of inversion domain in monolayer MoS_2. This experiment was performed at room temperature on a monolayer MoS_2 sample that has not been annealed at high temperature. (a-f) Sequential Z-contrast imaging of the nucleation and growth of the inversion domain induced by sulphur vacancies, similar to the process observed in monolayer $MoSe_2$. Sulphur vacancies agglomerating into 4|4E GB-like defect structure prior to the nucleation are highlighted by red circles; 60 ºGBs are highlighted by red dashed lines. Sulphur vacancies that trigger the Mo sublattice displacements are highlighted by blue circles, and white arrows indicate the displacement of the Mo atoms. The overlaid red triangles indicate the size of the inversion domain while the green trapezoid highlights the expanded region. The sulphur vacancies are first observed to agglomerate in line defects (a-c), and then nucleate an inversion domain (d, e), which continues to grow (f). (g-i) Overlapping images of (c-f) in order to show the displacements of the Mo sublattice. The initial image is colorized in red while the image taken after is colorized in yellow. All sequential images were acquired at an acceleration voltage of 60 kV with an electron dose rate that

is similar to the experiments on $MoSe_2$ described in the main text (~ 4×10^6 e/nm^2• s). Scale bar: 0.5 nm.

In conclusion, I show that the collective evolution of Se vacancies ultimately leads to the formation and growth of inversion domains and their 60˚ GBs within monolayer $MoSe_2$. I find that Se vacancies tend to first agglomerate into line defect complexes, which subsequently trigger the nucleation of an inversion domain. The growth of such inversion domains occurs *via* the migration of the 60˚ GBs in the presence of additional Se vacancies. The same process can occur during thermal annealing when sufficient thermal energy is supplied to overcome the barrier for the formation and migration of chalcogen vacancies in the TMDC monolayer, as observed in Figure 4.1.

Chalcogen vacancies have been shown to be the most abundant point defect in CVD-grown TMDC monolayers [132] and contribute largely to the transport properties of TMDC-based devices [133, 134]. My study highlights the importance of chalcogen vacancies in the structural stability of TMDC monolayers and the creation of new functional defects. Atomic-level defect engineering in 2D materials is a promising way to tailor the electronic properties of these materials. These presented results demonstrate that inversion domains can be obtained at a relatively large scale *via* vacancy engineering. It should be possible in the future to control the choice of nucleation sites of the inversion domains within the material using electron-beam excitation while the subsequent growth to a specific size is achieved *via* thermal treatment.

CHAPTER V

FLEXIBLE METALLIC NANOWIRES WITH SELF-ADAPTIVE CONTACTS TO SEMICONDUCTING TRANSITION-METAL DICHALCOGENIDE MONOLAYERS

In pursue of ultra-small electronic components [135-139], monolayer electronic devices have been recently fabricated using transition-metal dichalcogenides (TMDC) [59, 140, 141]. While the monolayers are semiconducting, nanowires of these materials with stoichiometry MX (M=Mo or W, X=S or Se) have been predicted to be metallic [142, 143]. Such nanowires have been chemically synthesized [144-146]; however, the controlled connection of individual nanowires to monolayers, an important step towards 2D integrated circuit, has so far remained elusive.

Previous work reported the fabrication of nanoribbons in a MoS_2 monolayer using the electron beam in a transmission electron microscope (TEM) [147]. These nanoribbons were inferred via image simulations and theory to have Mo_5S_4 stoichiometry and then predicted to be semiconducting [147]. Such top-down fabrication of nanostructures within the monolayer shows that electron-beam engineering of the atomic structure of two-dimensional (2D) material is achievable in the nanometre scale. In this project, I show that the focused electron beam of a STEM provides precise and flexible control over the illumination regions where the electrons interact with the sample. The electron beam can be manipulated to controllably drill holes and pattern nanowires within the monolayer. Moreover, nanowires fabricated in different TMDC materials have the same

MX stoichiometry in their final stable forms. By combining theory and experiments, I will also demonstrate that these nanowires are in fact metallic, as needed for applications in nanoelectronics.

To fabricate nanowires at designated positions with nanometre-scale precision, I exploit the ionization etching [6] of the semiconducting TMDC monolayers under a focused low-energy electron beam in a STEM. Figure 5.1 shows a Z-contrast image of the controlled patterning of a nanowire network that is fabricated directly from the $MoSe_2$ monolayer. The centred small $MoSe_2$ patch is connected to the parent monolayer through several nanowires with the same crystal structure.

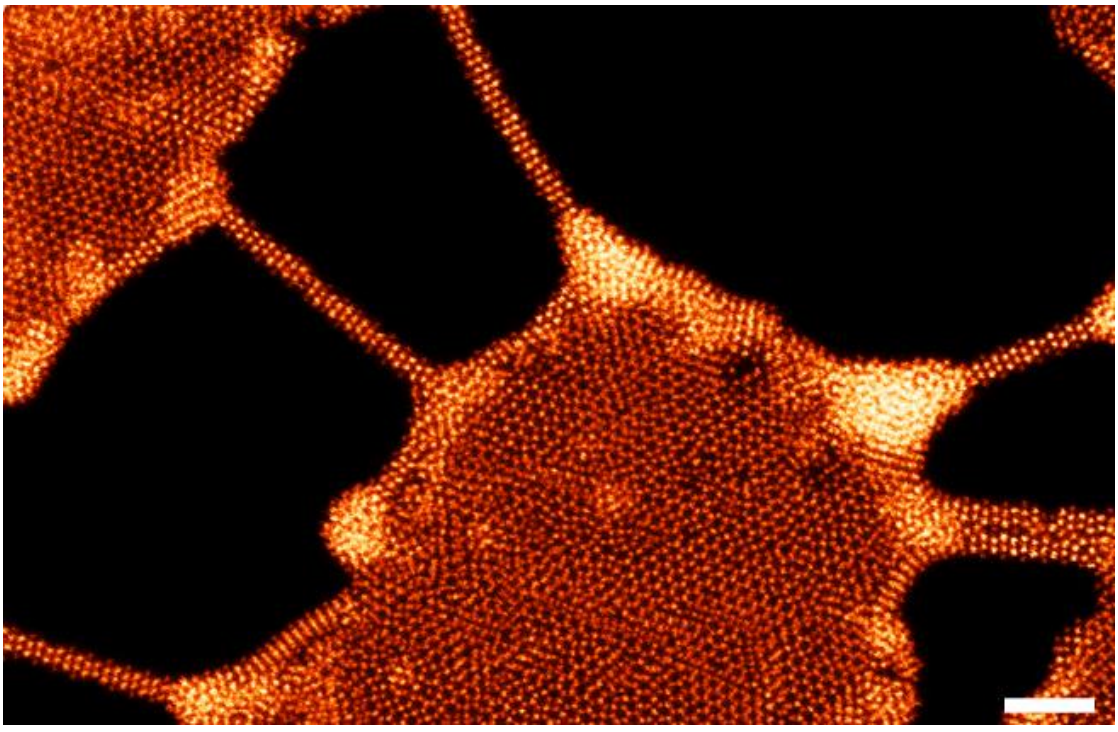

Figure 5.1: Patterning of a MoSe nanowire network with each nanowire sculpted individually. Scale bars: 2 nm

Figure 5.2 shows a detailed schematic of our fabrication process of an individual nanowire with location control. Prolonged exposure of TMDC monolayers to a 60 kV electron beam generates vacancies and vacancy complexes [148] which can expand into relatively large holes in the scanned regions primarily due to ionization effect [148-150]. By focusing the electron beam at selected regions, we drill two holes side-by-side, which confine a ribbon of the monolayer at the designated site as shown in Figure 5.3. Further electron irradiation changes such ribbons of monolayers into thick wires due to the re-deposition of atoms that are etched away from the edges of the ribbons. Figure 5.4 show a few sequential STEM Z-contrast images demonstrating the thinning of these thick wires by either etching away excess atoms from the thick structure (Figure 5.4a-e) with the electron beam or unzipping from the centre of the thick wire with the excess atoms diffusing away to the end junctions (Figure 5.4f-j). When the wire narrows down to a critical width of ~ 5 Å, the centre section self-assembles into a *stable* nanowire structure, as shown in Figure 5.4c and 5.4h. Figures 5.4e and 5.4j show the final results of sculpting an individual nanowire within the scanning window of the electron beam. No significant amount of carbon is incorporated in the wire during the fabrication process, as demonstrated by the electron energy loss spectrum that recorded during the sculpting (Figure 5.5).

I have also controllably fabricated nanowires in other semiconducting TMDC monolayers, such as WSe_2 shown in Figure 5.6. The spatial precision for positioning the nanowire using this method is in the nanometre scale (< 5 nm in the transverse direction of the nanowire), which is mainly determined by the separation of the two patterned holes in the TMDC layer.

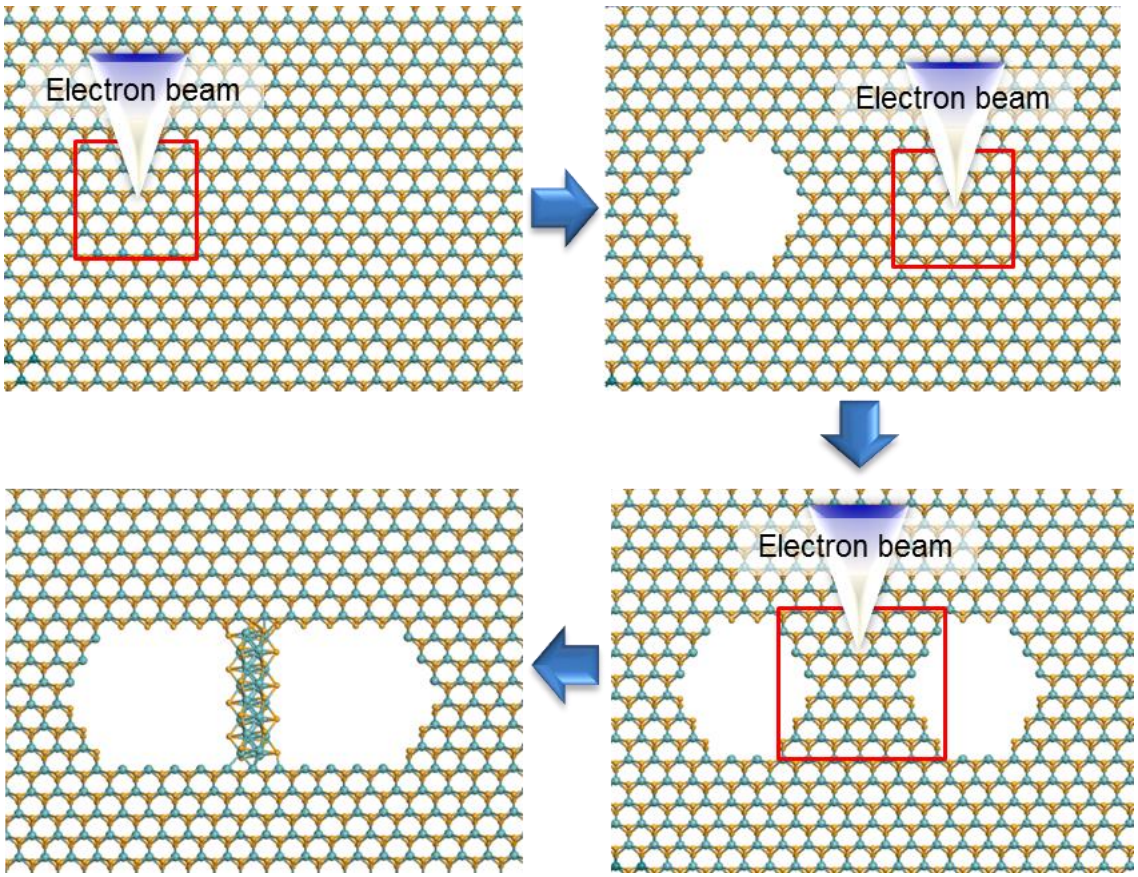

Figure 5.2: Schematic of control formation of nanowires at designated positions via patterning holes by the electron beam. The areas highlighted in red indicate the scanning regions of the electron beam in each step. By controlling the locations of these electron-induced holes, we can pattern the nanowires at designated positions within the monolayer.

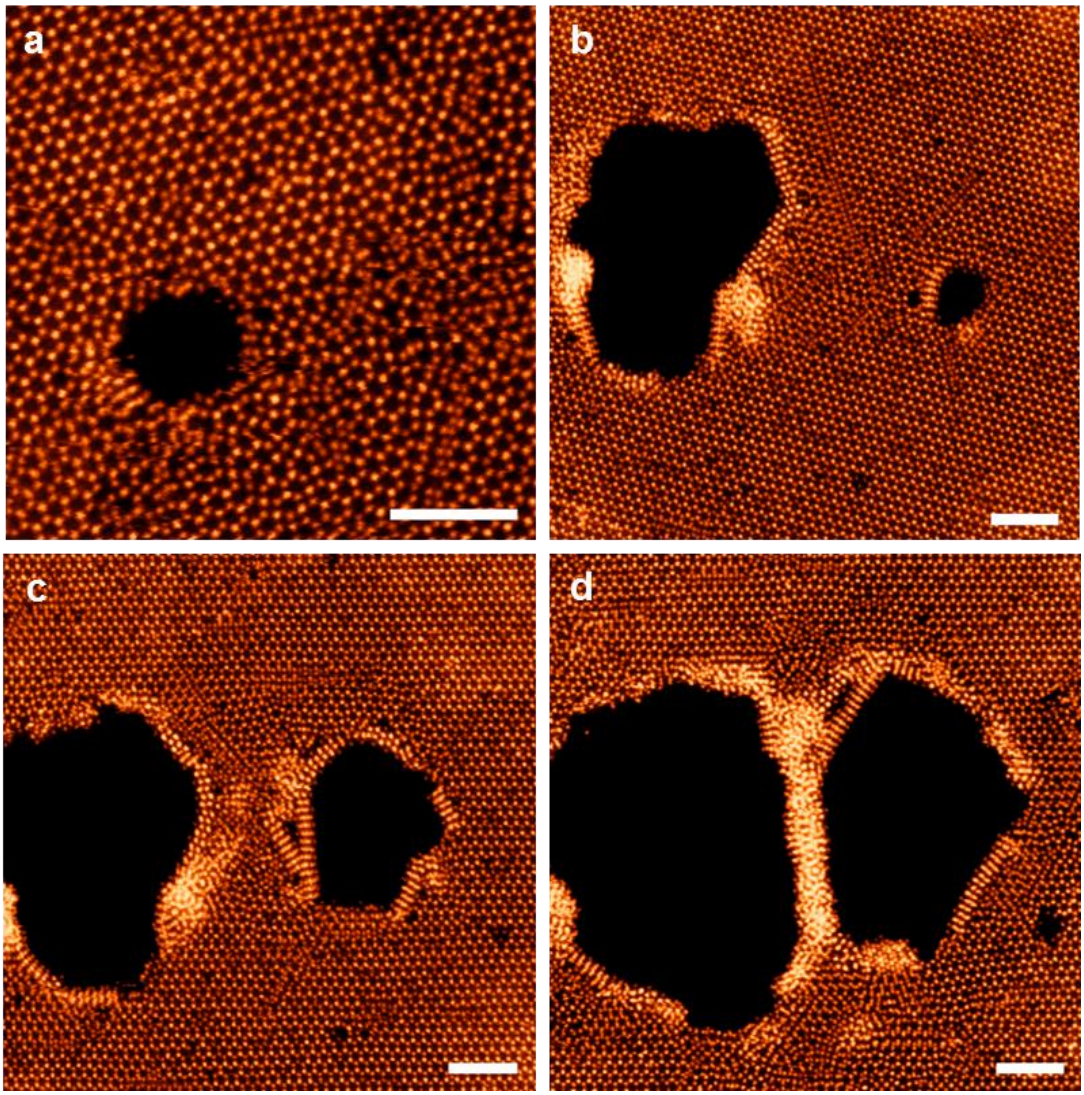

Figure 5.3: Preparing the thick wire for the fabrication of nanowires. The process is shown on a monolayer $MoSe_2$ as an example, which can also be applied to other TMDC monolayers. (a) A hole is created by focusing the electron beam with high current on the designated region of the monolayer. (b) Repeating the same process in (a) on a nearby region, which creates a thin ribbon of monolayer $MoSe_2$ confined by the two holes. We control the orientation of the ribbon by patterning the locations of the holes. (c) The electron beam is kept scanning the ribbon region. The ribbon region begins to reconstruct and shrinks to the centre due to atom diffusion. (d) After iterative electron irradiation, the ribbon becomes a thick wire serving as a reservoir of Mo and Se atoms, which is ready for being fabricated into a nanowire. Scale bars: 2 nm.

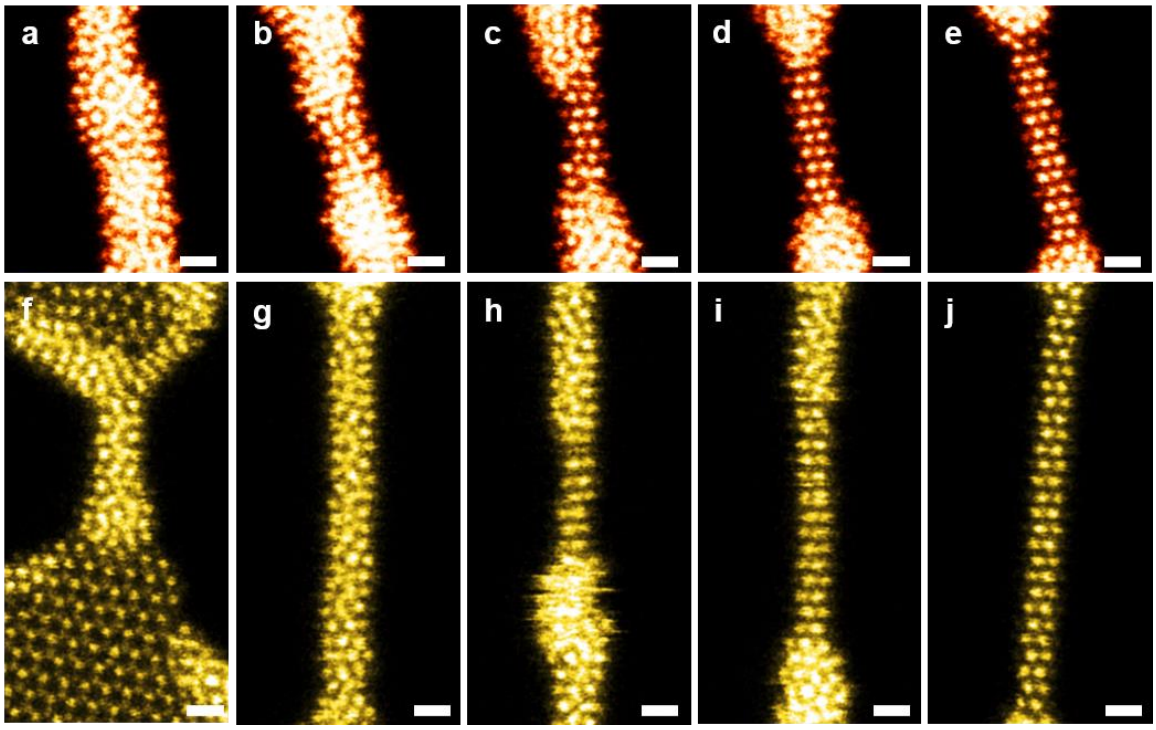

Figure 5.4: (a-j) Extracted serial snapshots for the sculpting process of an individual MoSe (a-e) and MoS (f-j) nanowire. All images are STEM Z-contrast images, false coloured for better visibility. Scale bars: 0.5 nm.

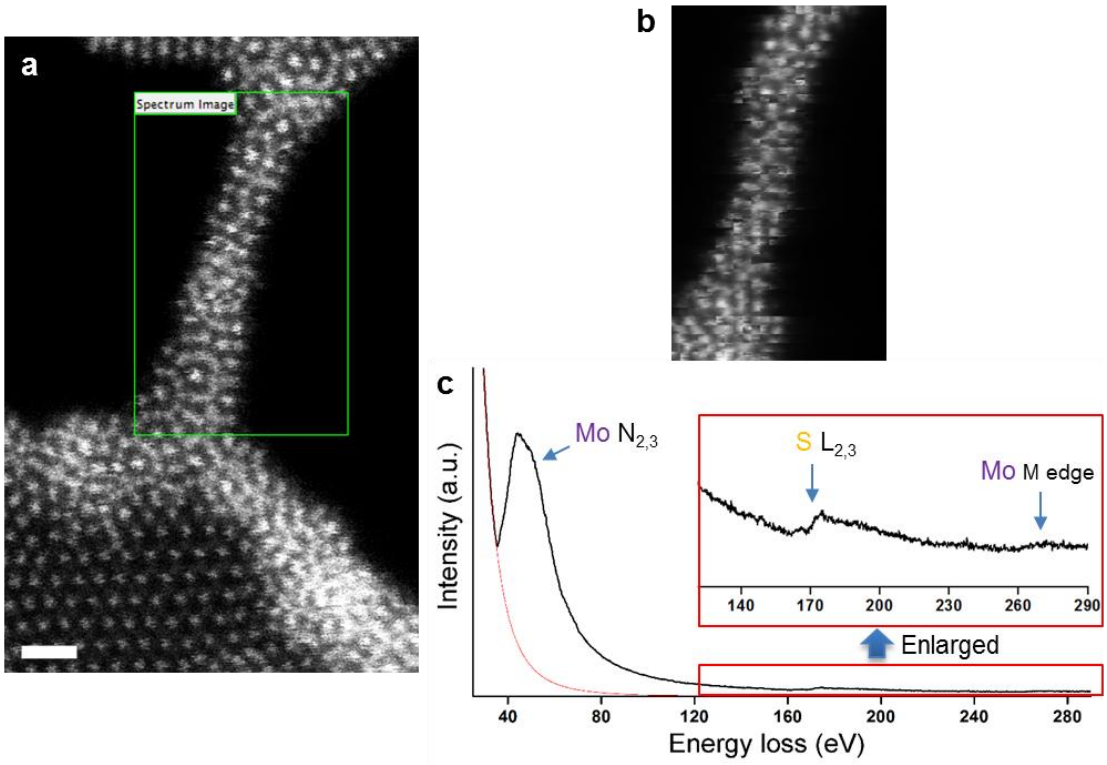

Figure 5.5: Electron energy loss spectrum image of a Mo_xS_y thick wire. (a) ADF survey image. (b) Simultaneously acquired ADF image during spectrum imaging. (c) The sum EELS spectrum from the whole spectrum image. Both Mo and S can be observed while no noticeable carbon is detected. The small bump between 260 and 290 eV comes from Mo. The red curve indicate the background of the Mo $N_{2,3}$ peak. Scale bar: 0.5 nm.

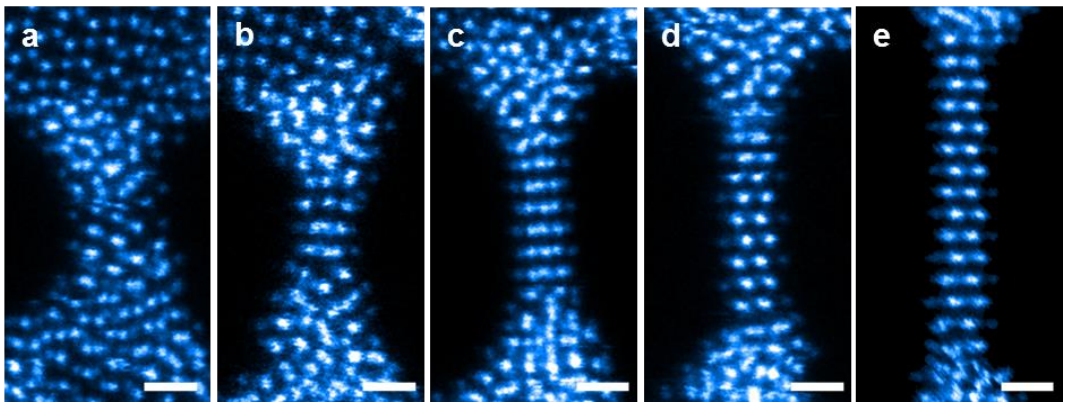

Figure 5.6: Fabrication of a WSe nanowire. (a-e) ADF images showing the fabrication of a WSe nanowire similar to the MoS and MoSe ones reported in the main text. The self-

reconstruction starts from the middle of the thick wire, which is indicated in Movie S3. Scale bars: 0.5 nm.

The length of the nanowire can be controlled by adjusting the size of the holes that confine the monolayer ribbons. I have succeeded in fabricating nanowires as long as ~ 10 nm. It is important to note that, during the fabrication, different initial structures always reconstruct into the same final stable nanowires, *i.e.* the fabrication process is self-regulating, which might be driven by spontaneous phase transition [147]. Meanwhile, these as-formed nanowires are highly robust against the direct knock-on damage from the electron beam, as the thresholds for knocking out atoms from the nanowires is much higher than 60kV, as shown in Table 5.1 and 5.2.

Maximum energy transferred from electrons to atoms under 60kV			
S	Se	Mo	W
4.3 eV	1.8 eV	1.4 eV	0.8 eV

Table 5.1: Maximum energy transferred from electrons to chalcogen and metal atoms under 60kV.

Displacement threshold (eV) and corresponding knock-out voltage on different structures

Composition / Structure	Mo-S		Mo-Se		W-Se	
	Mo vacancy	S vacancy	Mo vacancy	Se vacancy	W vacancy	Se vacancy
Monolayer (MX_2)	18.5	6.8 (90kV)	17.0	6.4 (200kV)	19.5	6.4 (200kV)
Zigzag ribbon	11.5	4.8 (68kV)	10.5	4.6 (150kV)	11.0	4.4 (143kV)
Armchair ribbon	12.5	5.2 (73kV)	11.5	4.8 (155kV)	12.0	4.8 (155kV)
MX nanowire	14.5 (450kV)	6.6 (88kV)	13.0 (410kV)	5.8 (180kV)	17.0 (820kV)	6.0 (190kV)

Table 5.2: Displacement threshold (eV) for metal and chalcogen vacancies in various structures. Note that in the DFT-MD calculations we use 0.5 eV as steps for the metal atoms and 0.2 eV for the chacolgen atoms to increase the initial kinetic energy. The corresponding knock-out voltages are in parentheses.

Occasionally, I observe that the capping S or Se atoms of the nanowire are removed by the electron beam, but recapping occurs rapidly via atomic diffusion due to the low diffusion barrier calculated by DFT (Figure 5.7). These processes impart self-healing characteristics to the nanowires, allowing for simultaneous fabrication of multiple nanowires by drilling multiple holes side-by-side. To connect three (or more) nanowires to create junctions, I pattern the holes in a triangular shape and expose the confined ribbons alternately to the electron beam, as shown in Figure 5.8. A ramified Y-junction connecting three MoSe nanowires is shown in Figure 6.8d, demonstrating the diversity of the building blocks that can be fabricated by steering the focused electron beam of a STEM. In contrast, control over the location of the nanowires and fabrication of such junctions would not be practical using the TEM-based technique reported in Ref. 113.

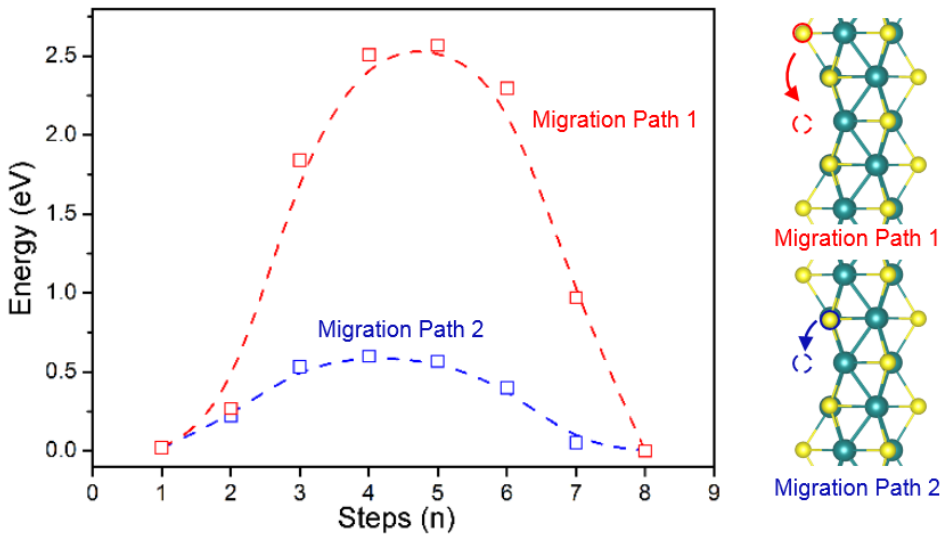

Diffusion barrier of chalcogen atoms	S @ MoS	Se @ MoSe	Se @ WSe
Path 1 barrier (eV)	2.57	2.16	1.93
Path 2 barrier (eV)	0.65	0.60	0.35

Figure 5.7: Diffusion barriers for chalcogen atoms in different types of nanowires. Two possible migration paths are proposed for the chalcogen atoms migrating along the axial direction of the nanowire. Migration path 1 is assumed for the second nearest chalcogen atom while migration path 2 is for the first nearest chalcogen neighbour. The energy vs. steps diagram shown above represents the case for MoS nanowire, while the energy barriers for other types of nanowires are summarized in the table below.

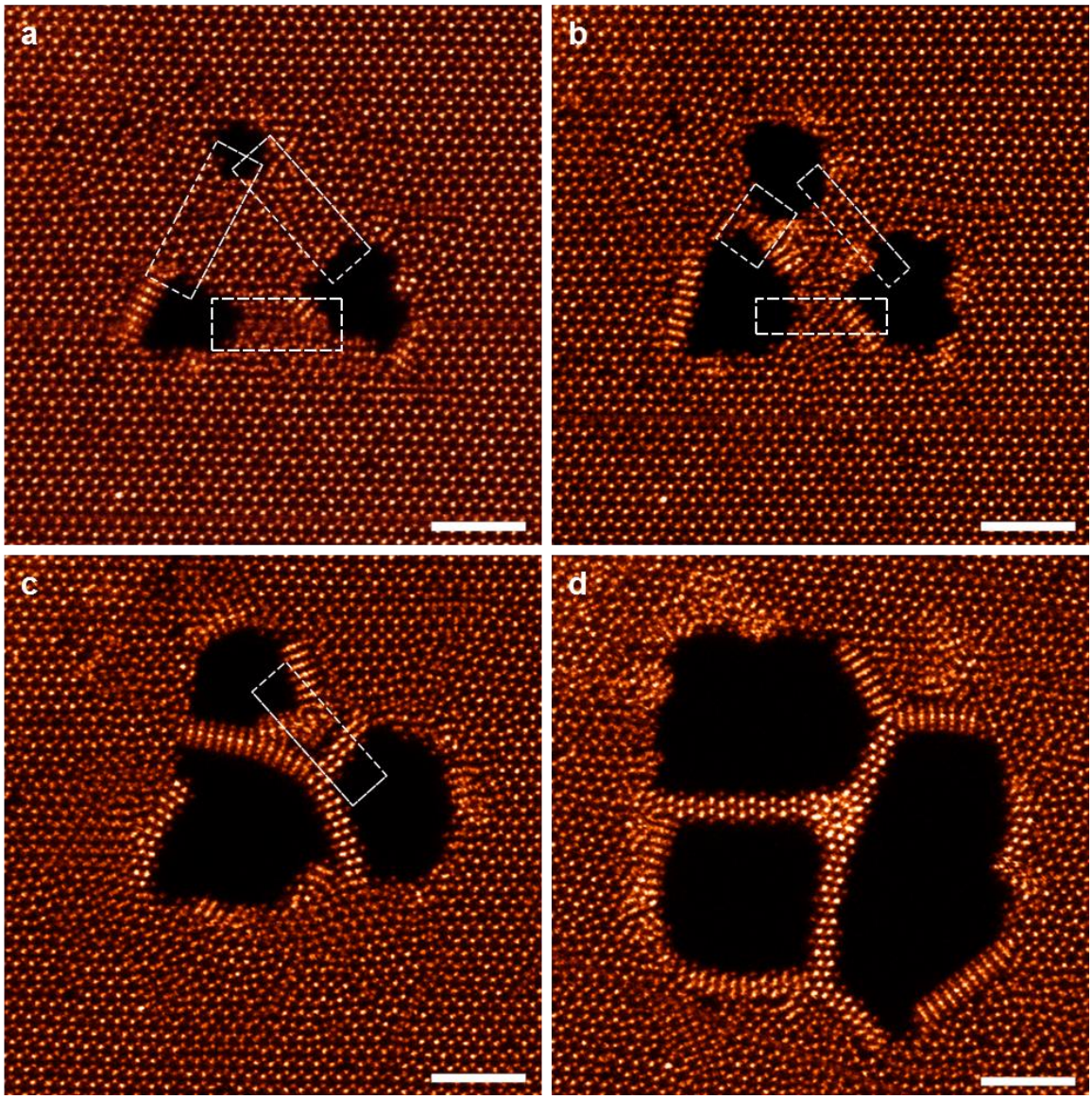

Figure 5.8: Fabrication of a ramified Y-junction of MoSe nanowires. (a-d) Sequential ADF images of the fabrication process. The three holes are patterned using the same method described in the main text. By carefully steering the electron beam to scan only the regions indicated by the white dashed squares in each image, the pre-designed ramified junction can be created controllably. The method can be in general applied to create other shapes of ramified junctions that connect multiple nanowires by patterning the holes in proper positions and using the controlled-scan method. Scale bars: 2 nm.

Since the formation of the nanowire is self-regulating under electron irradiation, it is possible to fabricate the same MoSe nanowires using a TEM that is capable of *in-situ* electrical measurements. My Japanese collaborators performed current-voltage (I-V) measurements at various stages during the *in-situ* fabrication of the MoSe nanowire. The results are summarized in Figure 5.9, where the $MoSe_2$ layer first forms a thick wire (Figure 5.9a, similar to the structure characterized in the STEM and shown in Figure 5.4) and subsequently forms a *stable* MoSe nanowire structure (Figure 5.9b). The corresponding electrical data (Figure 5.9d & Figure 5.9e) shows a substantial increase in electrical conductance as the nanowire forms, direct evidence of the conversion of the semiconducting monolayer to a metallic nanowire. The time evolution of the conductance during the *in-situ* fabrication of another individual MoSe nanowire is plotted in Figure 5.9g. The formation of the nanowire marks approximately 15 times increase in electrical conductance (estimated from the mean values before and after formation of the nanowire), which remained roughly the same throughout the lifetime of the nanowire. Furthermore, the metallic nature of the nanowires is consistent with the fact that they are much more stable under the electron beam than their parent semiconducting TMDC monolayers.

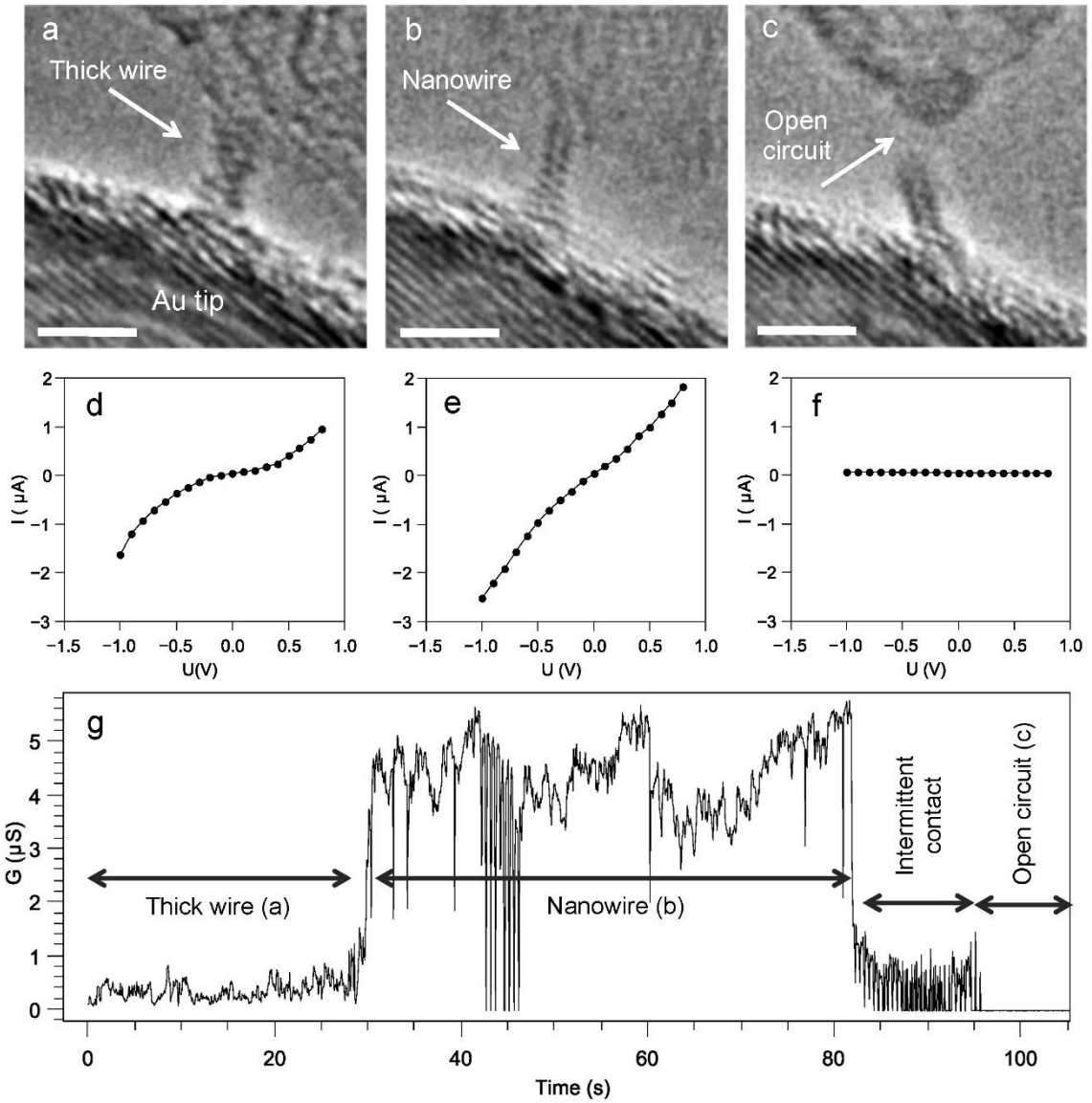

Figure 5.9: *In-situ* electrical measurement of a MoSe nanowire. (a-c) TEM images acquired during *in-situ* fabrication of a MoSe nanowire between the gold contact and the layered $MoSe_2$, showing the initial formation of the MoSe thick wire (a, similar to Fig. 1c), formation of the stable MoSe nanowire (b) and breaking of the nanowire (c). The current-voltage measurements corresponding to those moments are displayed in (d) - (f) respectively. (g) The time-evolution of the conductance for the formation and breaking of another MoSe nanowire (also shown in Movie S5). The labels for different periods in the figure refer to generic stages of formation/destruction of a nanowire, similar to those shown in (a-c). The voltage is kept constant at 1V[6]. The noise is due to mechanical instabilities of the experimental setup. Scale bar: 2 nm.

The non-linear I-V curves (Figure 5.9d & Figure 5.9e) suggest a Schottky-like contact, which may occur at connections between the nanowire, the $MoSe_2$ layers and/or the gold tip. In addition, we found that the gold tip is sometimes covered by a few layers of amorphous material (either carbon or Mo_xSe_y from previous experiments), leading to a slightly lower conductance (about ~ 5 μS, as compared to ballistic conductance in a 1D system [139]). The mechanical instability of the contact between the gold tip and the nanowire also leads to fluctuations in the measured electrical conductance (the fluctuation is about ±19%), as the contact resistance varies when the contact geometry changes. On the other hand, theoretical calculations suggest that the as-fabricated contacts between nanowires and the parent monolayer are Ohmic if the monolayer is doped p-type (Figure 5.10 & Figure 5.11). Such contacts may be possible to achieve in the future when interconnects between devices are fabricated directly by electron beams.

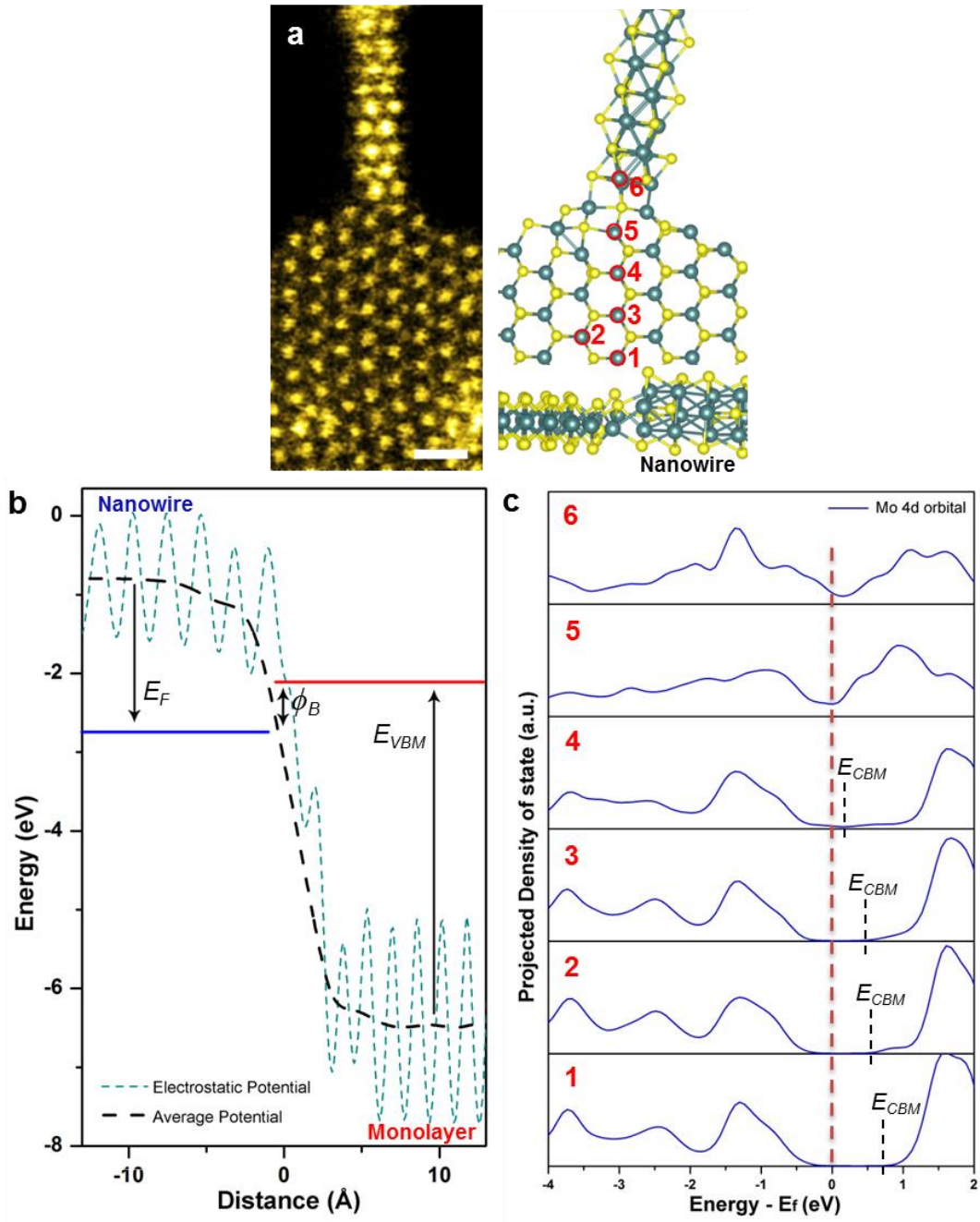

Figure 5.10: Atomic junction between the MoS_2 monolayer and MoS nanowire at 0˚ rotation. (a) STEM image of the atomic junction with the nanowire at 0˚ rotation. The corresponding atomic structure is provided on the right. (b) Band alignment of the metal-semiconductor interface shown in (a) using the average electrostatic potential as a reference. (c) Projected density of states of the Mo 4*d*-electrons along the Mo atoms across the interface. The numbers in each bar correspond to the labelled atoms shown in (a). Scale bars: 0.5 nm.

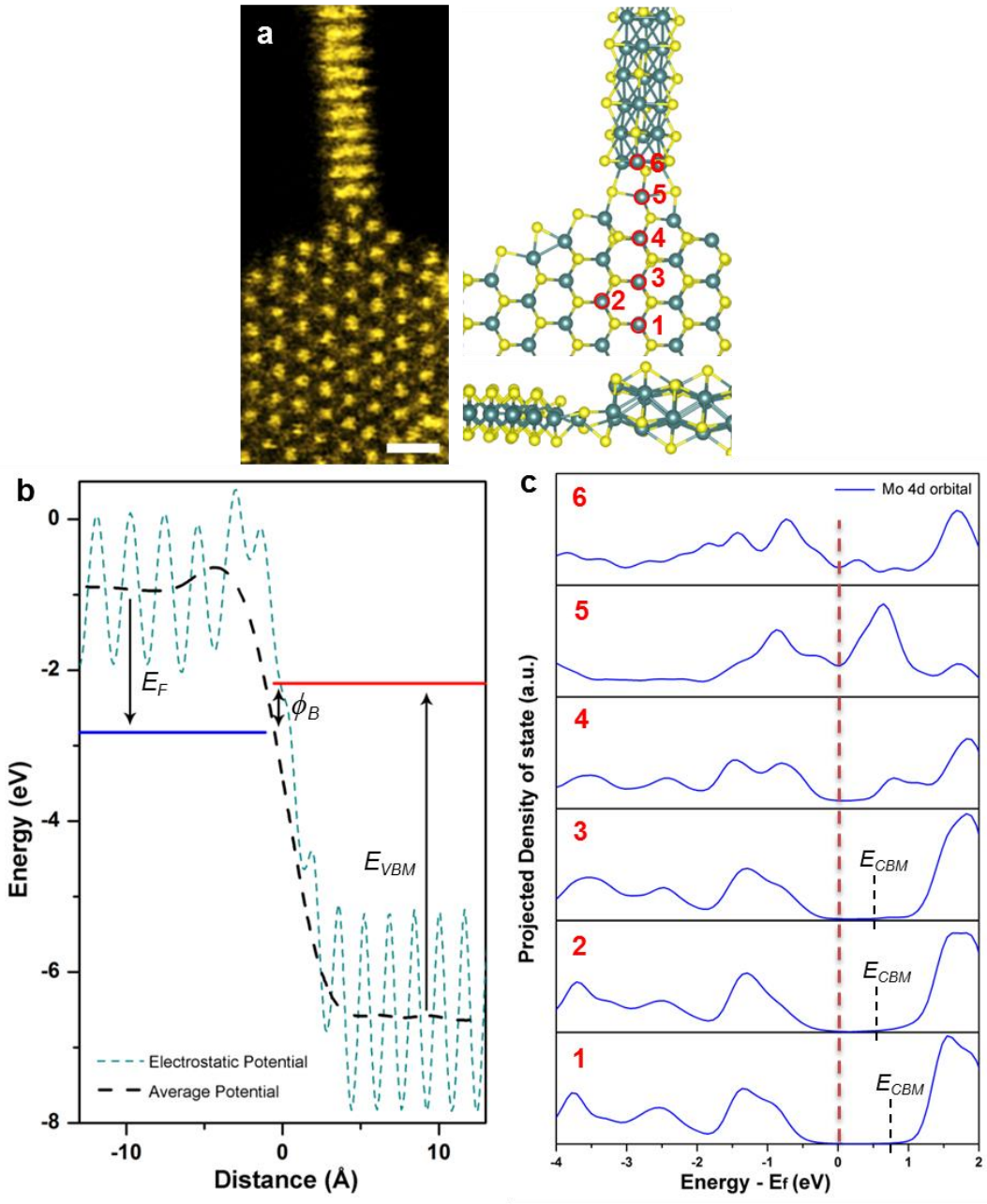

Figure 5.11: Atomic junction between the MoS_2 monolayer and MoS nanowire at 30˚ rotation. (a) STEM image of the self-adaptively reconstructed junction after the nanowire rotate 30˚. The atomic structural model is provided on the right panel. (b) Band alignment of the metal-semiconductor interface. (c) Projected density of states of the Mo 4*d*-electrons along the Mo atoms through the interface. The numbers in each bar correspond to the labelled atoms shown in (a). Scale bar: 0.5 nm.

To understand the observed metallicity of the nanowires, I performed density-functional theory (DFT) calculations based on the STEM Z-contrast images shown in Figure 5.4, which enable us to visualize every atom in the stable nanowires and identify its precise configuration. Figure 5.12a shows the atomic structure of the nanowires, with 1:1 atomic ratio of Mo (W) and S (Se). The Mo (W) and S (Se) atoms in the nanowires are arranged in consecutive stacks of triangular layers rotated 180° along the nanowire axial direction, with three capping S (Se) atoms located at the vertices of the triangles and three Mo (W) atoms located between the S (Se) atoms. Figure 5.12b and Figure 5.12c compare the experimental STEM images of MoSe, MoS and WSe nanowires with simulated images using the atomic model in Figure 5.12a, showing excellent match at all atomic positions. The measured axial lattice constants are also in good agreement with the DFT calculations (Figure 5.13). The width of the conducting nanowire is measured to be 4.4 Å for MoSe, 4.1 Å for MoS and 4.6 Å for WSe, an ultra-small diameter comparable to that of the smallest carbon nanotubes (4 Å)[2]. DFT calculations show that the metallic characteristics of this nanowire family are due to the strong hybridization between the *d* orbitals of the transition-metal atoms with the *p* orbitals of the chalcogen atoms (S or Se), which form free electron-like bands crossing the Fermi level (Figure 5.14) [142, 143].

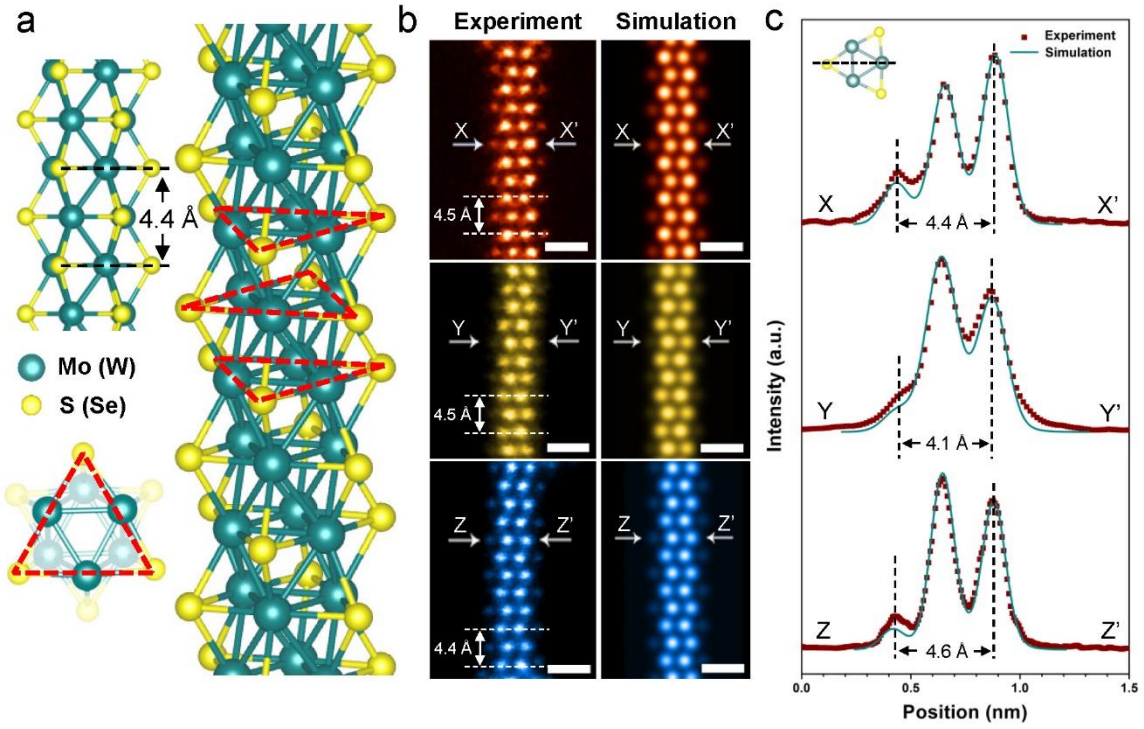

Figure 5.12: Atomic structure of the nanowire. (a) Atomic structural model of the nanowires. The dashed red triangles indicate the orientation of each layer in the nanowire. (b) Experimental (left) and simulated (right) STEM Z-contrast images of an individual MoSe (orange), MoS (yellow) and WSe (blue) nanowire. The axial lattice constant is measured from the experimental images. (c) Normalized intensity line profile along the X-X', Y-Y' and Z-Z' direction in (b), with a side view of the atomic structural model provided in the inset. Scale bar: 0.5 nm.

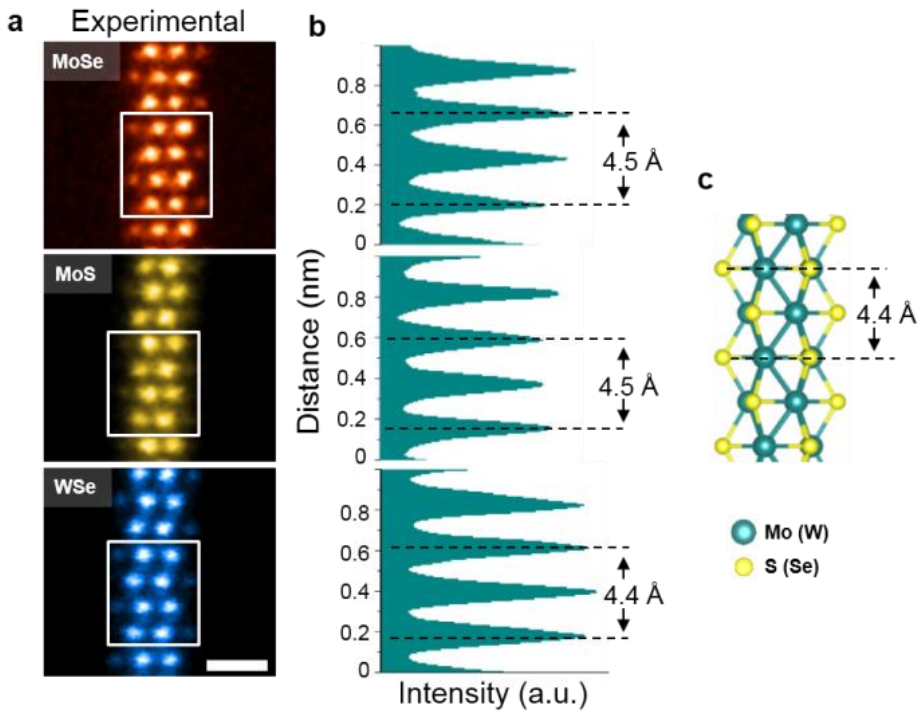

Figure 5.13: Axial lattice constant of the nanowires. (a) Experimental ADF images of different types of nanowires (Fig. 2b, main text). (b) Averaged intensity profiles along the axial directions of the nanowires highlighted by white rectangles in (a). (c) DFT calculated axial lattice constant. All three types of MX nanowires have nearly the same axial lattice constant of 4.4 Å. The experimental values are in excellent agreement with DFT value, within the experimental error.

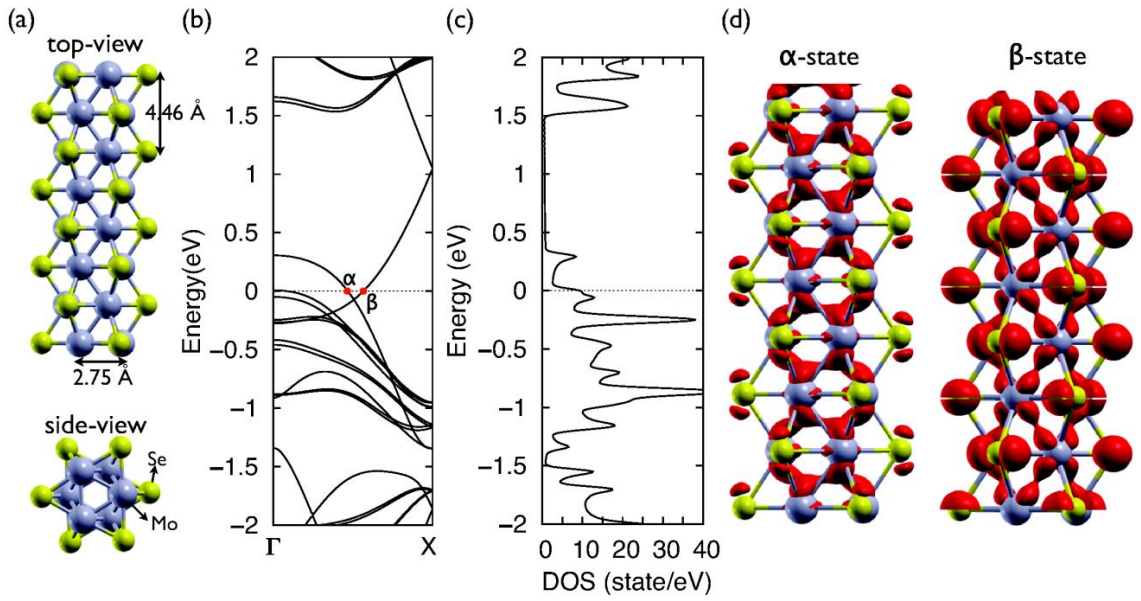

Figure 5.14: Electronic structure of the nanowire calculated by DFT. (a) Structure of the MoSe nanowire with optimized lattice parameters. (b) Band diagram of the nanowire, showing three bands crossing the Fermi energy level. (c) Density of states of the MoSe nanowire. (d) Squared wavefunction distribution of states which are labelled as "α" and "β" at the Fermi level in (b), showing hybridization between the Mo *d*-orbitals with the Se *p*-orbitals along the direction of the nanowire.

The mechanical flexibility of the nanowires are further explored via sequential imaging, where the electron beam acts as a source to excite the deformations of the nanowire. I find the nanowires can rotate, flex and bend continuously under the electron irradiation while maintaining their stable atomic structure, a strong indication of excellent mechanical flexibility. Bending of the nanowires is demonstrated in Figure 5.15, which is recoverable, consistent with previous theoretical studies [151]. Figure 5.16 provide an atomic-scale analysis of the rotation and out-of-plane deflection of the nanowires. The atomic-scale rotations occur at several discrete stable rotation angles, with rapid switching between them. Figure 4a shows a schematic diagram of out-of-plane deflection and rotation along the *c*-axis of the nanowires, with the angles indicated by (α, β),

respectively. A set of discrete stable rotation states, indicated by the corresponding (α, β) of the nanowire observed during the sequential imaging, are shown in Figure 5.16c. A maximum out-of-plane deflection angle of ~ 15˚ was observed. Rotations up to 30˚ can be identified, with ~5˚ accuracy. The 0˚ and 30˚ rotation states are much more stable than others as shown by the histogram in Figure 5.16b.

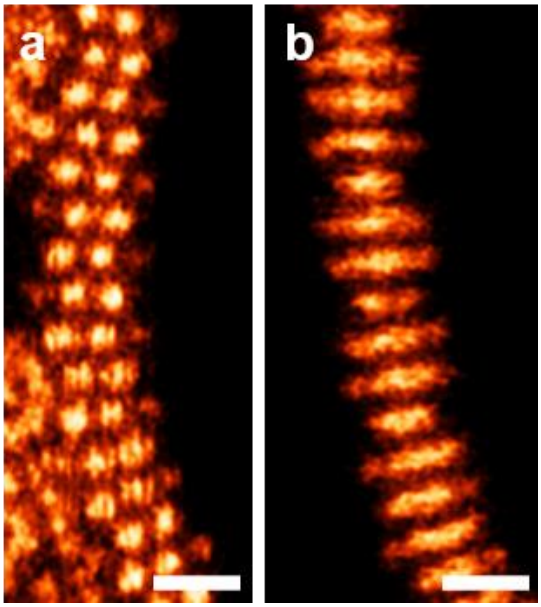

Figure 5.15: (a, b) Experimental STEM images showing bending of MoSe nanowires. Scale bar: 0.5 nm.

The rotation of the nanowires by discrete angles is further demonstrated in Figure 5.17, where the whole nanowire rotates 30˚ while the electron beam is scanning across one atomic layer of the nanowire, as indicated by the dashed line. The fast switching between specific rotation angles is estimated to be in the millisecond range, and was consistently observed under different scanning settings.

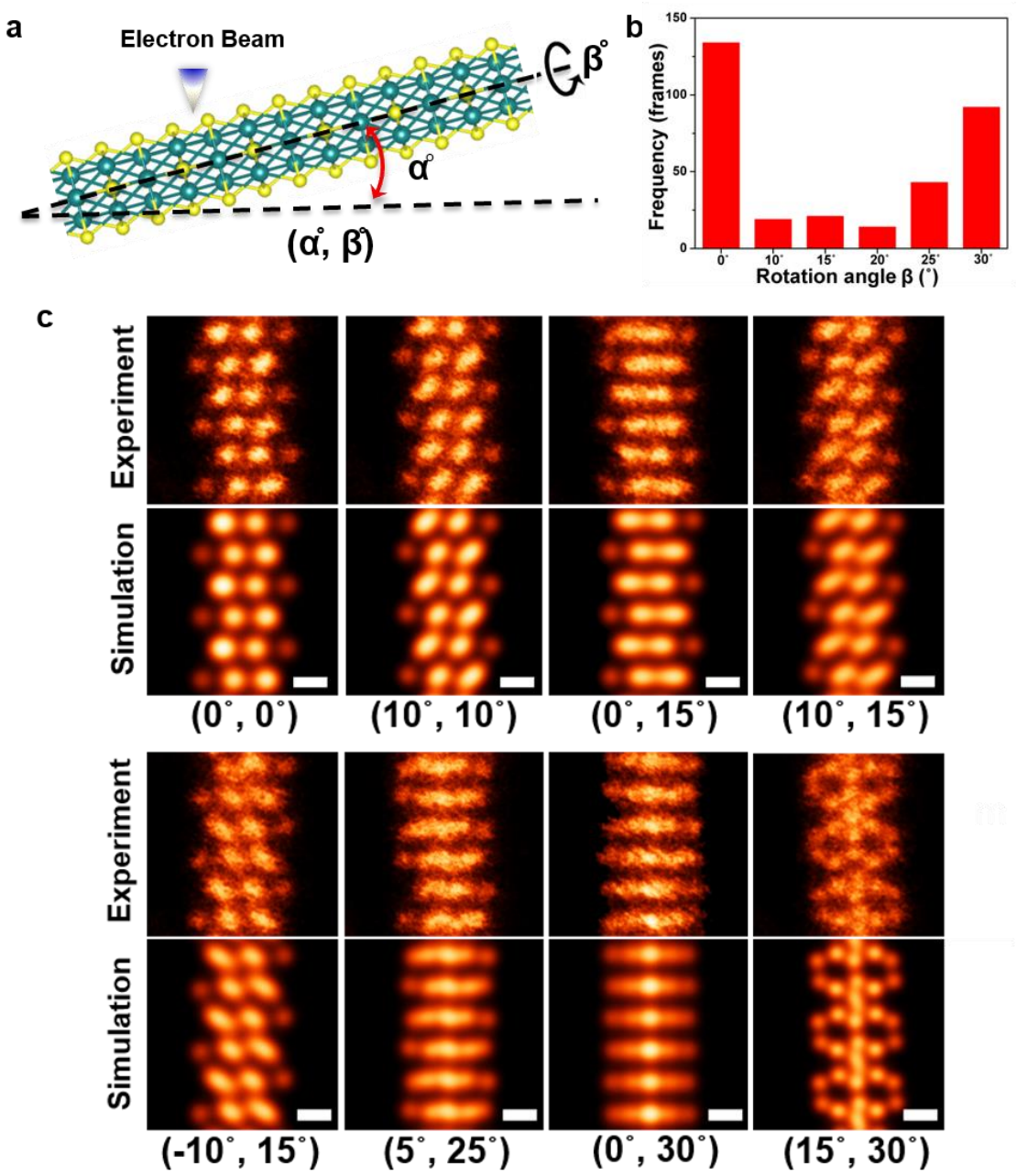

Figure 5.16: Flexing and discrete rotations of a nanowire between the junctions. (a) Schematic of the dynamic movements of the nanowire. α is the out-of-plane deflection angle of the nanowire while β is the rotation angle along the *c*-axis of the nanowire. (b) Statistics of different rotation angles observed on a MoSe nanowire during the sequential STEM imaging. (c) Experimental and simulated STEM images showing different combinations of rotation and deflection of the MoSe nanowire.

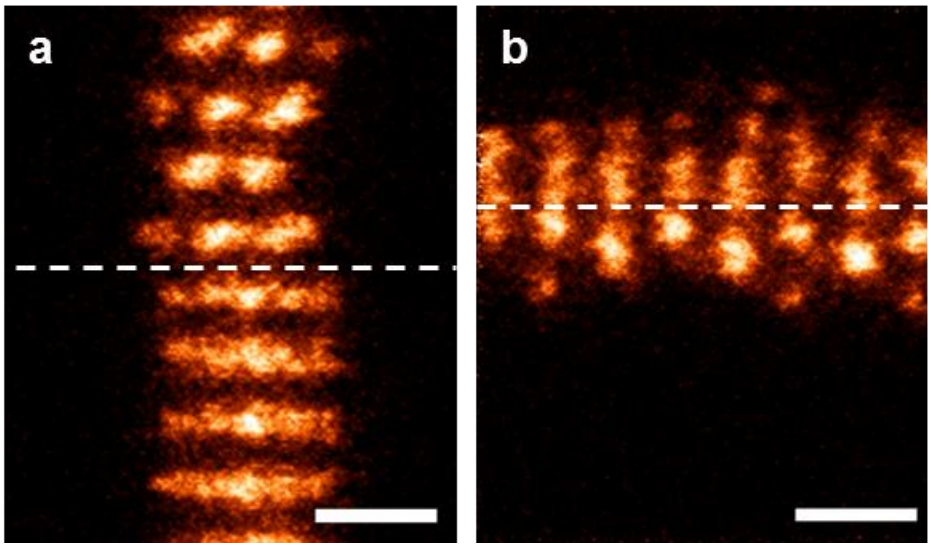

Figure 5.17: Fast switch between different discrete rotation states. The scanning direction is set to be perpendicular (a) or parallel (b) to the nanowire. The white dashed lines indicate the boundary between different discrete rotation states, which can be used to estimate the switching time by counting the dwell time of pixels along the boundary. All the switches happen in the range of milliseconds. Scale bars: 0.2 nm.

The fact that the nanowires can rotate to a large angle without being torn apart suggests that the rotations are accompanied by self-adaptive reconstruction at the atomic junctions between the nanowires and the TMDC monolayers. Figures 5.18a and 5.18e show two stable configurations of the atom-wide junctions, differing by a 30˚ rotation of the nanowire. After the rotation, the nanowire reconnects seamlessly to the MoS_2 monolayer, *i.e.* the junction is self-adaptive (Figure 5.18). The nanowire-monolayer junctions generally form and persistently reconstruct at protrusions of monolayer edges with minimum bonding constraints from neighbouring atoms. Such pivot-like junction structure enables the nanowire to switch between different rotation angles with a minimum energy. DFT calculations based on a shorter nanowire, as shown in Figure 5.19, account for the most stable 0˚ and 30˚ rotation states observed experimentally

(Figure 5.16b), and find a maximum energy barrier of ~3 eV for the whole nanowire to rotate, which can be easily overcome with the energy transferred from the electron beam [152].

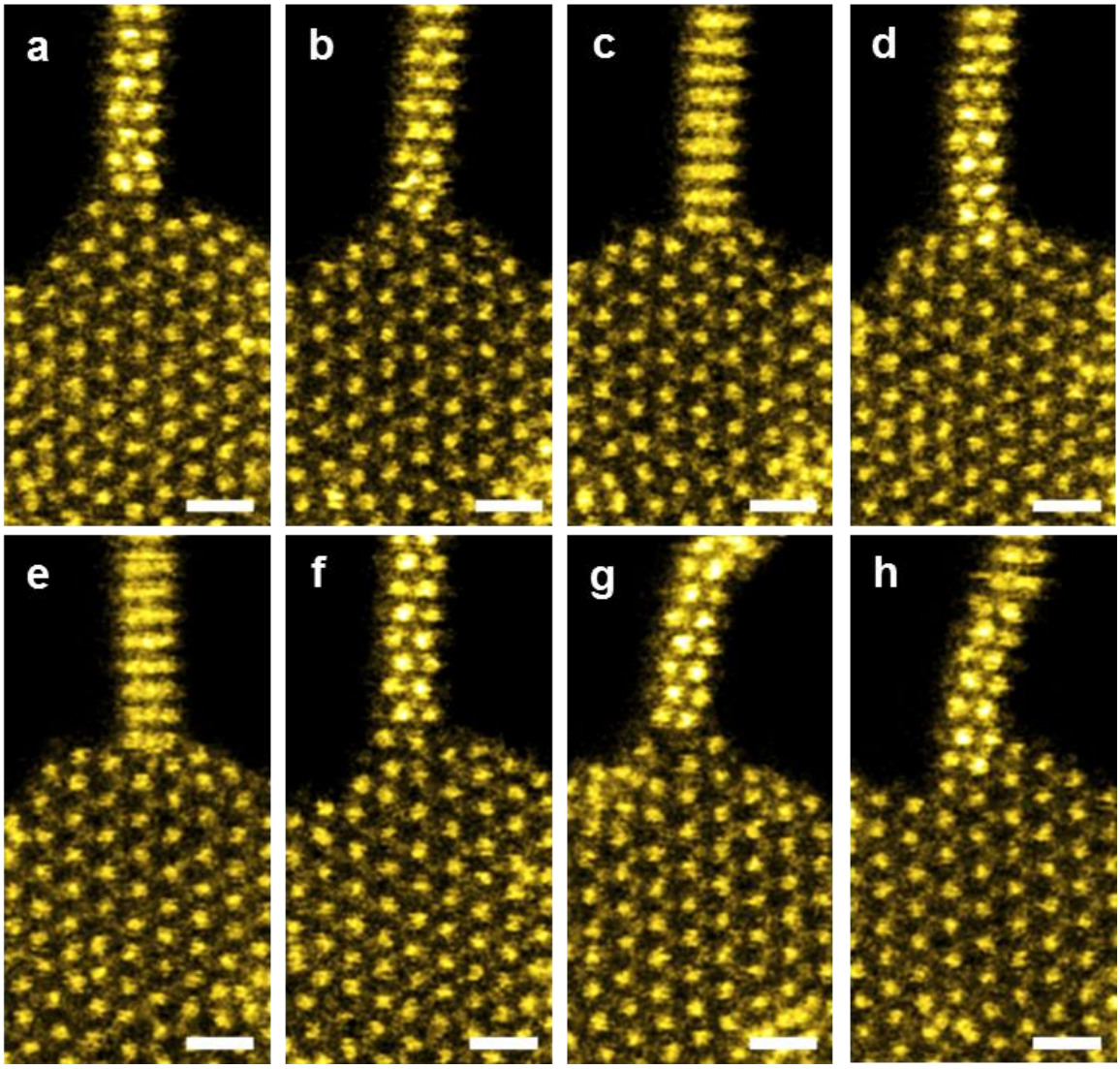

Figure 5.18: Sequential Z-contrast images showing a variety of morphologies of the self-adaptive junctions. (a-h) Diverse configurations of the self-adaptive atomic junctions between the MoS nanowire and the MoS_2 monolayer. Each image was taken sequentially after the nanowire rotated to a different angle. The junction can reconstruct to different stable configurations in response to the rotation of the nanowire and maintain robust connection. Scale bars: 0.5 nm.

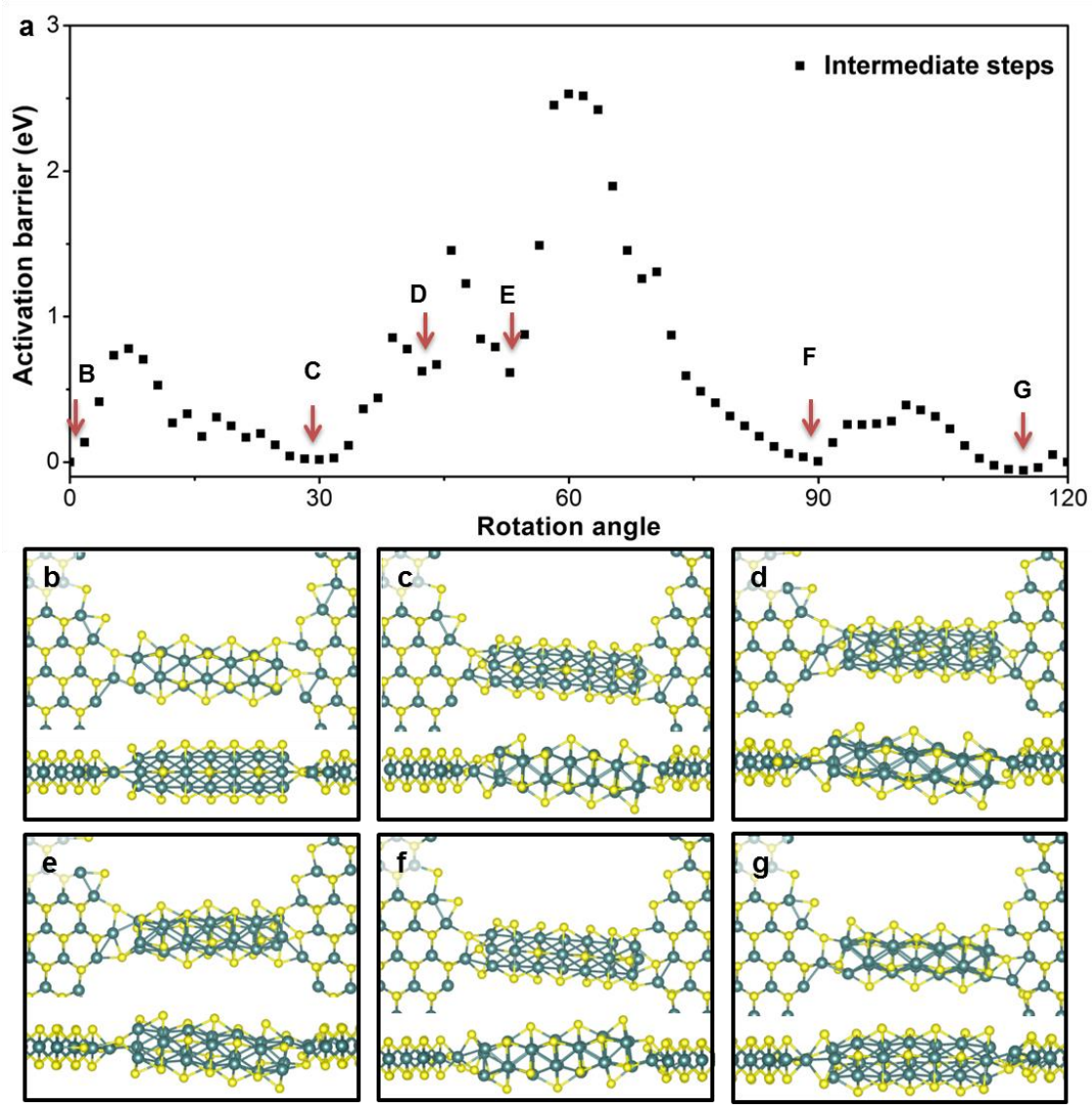

Figure 5.19: Energy map of the stable states of a nanowire between two junctions. (a) DFT calculations show that the nanowire has several discrete metastable states during the rotation. Some states maintain low energy as compared with others, but appear very similarly in STEM images. For instance, the states (b & g) and (c & f) could appear as rotation angle of 0˚ and 30˚, respectively, in the STEM images shown in Fig. 4c (main text). (b-g) Corresponding atomic structures of the states labelled in (a). The relaxed structures also indicate that slight out-of-plane deflection of the nanowire can occur during structure relaxation. The large deflection of ~ 15˚ observed in the experiments (the last panel in Fig. 4c, main text) most likely originates from fluctuation at the two ends of the nanowire, which further demonstrates the flexibility of the system. The activation barrier, the amount of metastable states and their atomic structures depend on the edge structure of the monolayer and the length of the nanowire. Therefore, the model used above only accounts qualitatively for the origins of the discrete rotation observed in our experiment.

Combining the *in-situ* time-evolved conductance measurements (Figure 5.9) and the mechanical flexibility of the nanowire (Figure 5.16), we indeed show that the nanowire remains conductive when it undergoes mechanical deformation (rotations and flexing). This result confirms that the self-adaptive nature of the nanowire-monolayer junction does not change the electronic properties of either the nanowire or the junction, as further confirmed by DFT calculations (Figures 5.10 & 5.11), which would be important for future flexible nanoelectronics.

TMDC-based devices with excellent mechanical flexibility have inspired research on assembling multiple devices into circuits [109, 140]. The pliable metallic nanowires described in this paper, with robust junctions at designated locations, may serve to connect multiple atom-thick nanoelectronic components towards 2D fully integrated flexible nanocircuits. Moreover, together with the pioneering results from Ref. 14, the formation of these nanowires can be achieved in various acceleration voltage and vacuum levels (see *Methods*), suggesting it may be possible in the future to first fabricate devices in a TDMC monolayer and subsequently sculpt high-quality nanowire interconnects using a scanning electron microscope or an electron beam lithography system with optimized fabrication parameters, such as precise dose control of electron irradiation. Furthermore, the production could be scalable because it is insensitive to the initial shape of the monolayer, all nanowires eventually collapse to their stable structures, and the nanowires are self-healing under electron beam irradiation. The smallest separation between nanowires depends on how close the holes can be patterned, which should be achievable in the sub-100 nm regime. Combined with the self-adaptive contacts to the TMDC monolayer, which accommodates the mechanical behaviour of the nanowire,

these ultra-flexible sub-nm-wide conducting nanowires could serve as robust 1D electron channels and provide a new building block for future flexible integrated nanoelectronics [153].

The technical detail of the methods used in this study is described below:

1. Sample preparation: MoS_2, $MoSe_2$ and WSe_2 monolayer samples were exfoliated from bulk crystals. Similar to exfoliating monolayer graphene, we mechanically exfoliated the bulk material onto a Si wafer coated with a 300 nm SiO_2 via the scotch-tape method and identified the monolayers under the optical microscope [46]. We then transferred the monolayer flakes to TEM grids based on a polymer-free method [154] for the nanowire fabrication. Extra care was taken throughout the sample preparation and microscopy experiment in order to avoid carbon contamination. This included storing the samples under vacuum and performing Ion cleaning on the Au tips before each *in-situ* experiment. Moreover, our experiments were performed on carefully selected clean regions of monolayers, which did not show noticeable contaminations in the ADF images.

2. *In-situ* fabrication and imaging of nanowires: The fabrication of the nanowires was performed on a Nion UltraSTEM-100 operated at 60 kV[155] under ultra-high vacuum (~1×10^{-9} Torr). This fabrication process can also be realized at 100 kV with less control on patterning the holes. The beam current is adjustable (up to ~100 pA), which was used to control the sculpting process of the nanowires. The converged electron beam can be controlled to scan selected regions. The dwell time per pixel is set to be 2-4 μs (with repeated scans) for sculpting of the nanowire and 16-24 μs for imaging. All ADF images have been low-passed filtered to reduce random noise.

3. Experimental setup for the *in-situ* electrical measurement of the nanowire: Fabrication of the nanowires for *in-situ* electrical measurement was performed on a JEOL 2010F TEM under a vacuum level of ~10^{-7} Torr. $MoSe_2$ crystals were exfoliated using micromechanical cleavage. Some of the flakes were subsequently transferred to a dedicated sample holder [156], where the exposed flakes at the edge could be contacted with a gold tip prepared by electrochemical etching [157]. A sourcemeter connected to both sample and tip was used in order to collect the electrical data. In order to fabricate the nanowire, a few-layer region located at the end of a $MoSe_2$ flake was contacted with the gold tip. An electrical bias of the order of 2 V was then applied, leading to Joule-heating (electrical annealing) of the region around the contact. Electron irradiation from the 120 kV electron beam lead to the gradual thinning of the area and formation of the nanowire, similar to the fabrication process in STEM. The bias was lowered to around 1 V and kept fixed during the final stages, allowing more control over the process. The time-evolved conductance was derived from the electrical current, which was constantly recorded throughout the fabrication. The bias was interrupted over short periods of time (~1s), in order to allow the acquisition of I-V measurements at different stages of the fabrication.

4. Estimating the rotation angle of the nanowires: The rotation and out-of-plane deflection angles of the experimental images in Figure 5.16 are estimated by comparing experimental and simulated images, using 5˚ per step since it is difficult to distinguish small rotations of the nanowires from the images. Moreover, the rotation angle of 5˚ cannot be distinguished from 0˚, since the difference of projected atomic positions between these two rotation angles is too small to be resolved. Due to the 3-fold symmetry

of the nanowire, the rotation is anti-symmetrical at 60˚. However, the experimental images of 0˚ and 60˚ rotations look practically identical due to the growth of the nanowire and possible image drift between successive frames. Therefore, in our statistical study (Figure 5.16b) the rotation angle is only identified from 0˚ to 30˚.

CHAPTER VI

SUMMARY AND PERSPECTIVES

6.1 Summary of My PhD Research

In summary, all of my projects described in the previous Chapters show that the combination of the atomic resolution STEM Z-contrast imaging and DFT calculations serves as a power tool in revealing the structure-property correlations in materials. STEM Z-contrast imaging provides the insightful information from statistical structural characterizations to dynamical atom-by-atom movement tracking, and it can even be used in controllable fabrication of new nanostructures and simultaneously record the fabrication process. Complemented by DFT calculations, all the underlying physics behind the structures can be explored at single atom level.

In short, the major achievements in specific projects where I applied this combined technique are summarized as follows: (1) Stacking boundaries in bilayer graphene are revealed to be not atomically sharp but continuously strained channels that extend over several nanometers in the form of ripples, forming a low-energy smooth transition between different stacking domains; (2) The atomic structure of an atomically abrupt lateral interface between WS_2 and MoS_2 monolayers is directly visualized at the atomic scale with a prediction of type-II band alignment at the sharp interface; (3) The formation of inversion domains in monolayer $MoSe_2$ is found to be driven by the collective evolution of Se vacancies excited by the electron beam via sequential Z-contrast STEM imaging, where the formation mechanism is explored by DFT calculations; (4)

Controllable fabrication of three-atom-wide metallic nanowires within semiconducting transition-metal dichalcogenide monolayers is developed using electron irradiation, where the mechanical and electronic properties of the nanowires are studied by DFT.

Besides many novel physical phenomena and fascinating properties that emerge in 2D materials due to their atomic thickness, all projects in my PhD research show a common theme in the research of 2D materials: these 2D materials are not necessarily flat as commonly believed, and defects or interfaces within the pristine crystal could have profound influence on the properties and performance in these 2D materials. A large portion of current research interest in 2D materials lays in how to make devices from these materials for real applications. Understanding the structure-property correlations, especially for defects in 2D materials, is the essential step to engineer the functionality in these devices. My PhD research demonstrates a feasible and powerful means to investigate defect structures and their effect to the physical properties of 2D materials, which will continously benefit the community working in this field.

6.2 Perspectives on Future Electron Microscopy Research in 2D Materials

The family of 2D materials havs numerous novel physical phenomenon due to their reduced dimension. Moreover, they also serves as a wonderful platform for high resolution electron microscopy imaging since interpreting the Z-contrast images on these materials becomes much more straightforward: all atoms and their related movements are confined in a reduced dimension, where each atomic column can be unambiguously mapped out based on the image intensity without complicated elemental anaylsis. Such feature actually compliments the well-known insufficiency in high resolution Z-contrast

imaging, i.e., the depth information is missing, due to the intensity is the 2D projection of the convolutions between the probe and the object function of the material. Therefore, for 3D bulk materials, only information in a 2D plane along the zone axis can be obtained in real-time, while for 2D materials the achievable information matches exactly with the dimension of the material.

Since the successful application of aberration correctors and monochromators in transmission electron microscopes, the unprecedented spatial and energy resolution has enabled the imaging and spectroscopy reach singe atom sensitivity, pushing the understanding of the structure-property correlations in a material towards single atom level. Given the as-mentioned advantages in 2D materials, they will continue to serve as one of the most suitable platforms for demonstrations of new techniques that developed in electron microscopy, such as detection of magnetic circular dichroism with atomic-scale spatial resolution.

While the achievments in understanding the structure-property correlations in 2D materials are significant, there are several limitations in transmission electron microscopy characterizations of these materials. One essential problem is the contanmination and damage on 2D materials which prevent their intrinsic structure and property to be revealed. Inevitable contanmination, such as armophous carbon, is introduced during the fabrication of the sample. For the bulk sample, the effect from contanmination is less obvious since they are just thin layers compared to the atomic coloumns which may consist of hundreds of atoms as seen by the electrons. However, when the thickness of the sample reduces to several atoms, the effect of the contanmination becomes prominent. Regions of interest in 2D materials are usually structures other than the pristine crystal,

like dislocations and boundaries, which are more chemically active than its pristine lattice structure. Therefore, contamination usually piles up at those regions, preventing the imaging of the real atomic structure of these defects. This is a huge limitation on structure characterization that we can reach, especially in materials consist of light elements. For instance, there is no direct Z-contrast images showing how the grain boundaries look like in BN-graphene laterally interconnected heterostructure. Therefore, the cleaness of the sample is extremely important to what we can observe. Since the contanmination is mostly hydrocarbon in exfoliated and CVD sample due to the wet chemistry transfer method, a possible solution to such problem is to integrate a high-temperature annealing stage inside the microscope, which allows *in-situ* annealing of the sample in high vacuum inside the chamber to effectively evaporate the hydrocarbon. Dr. Suenaga has shown such scheme is feasible to create large clean region in 2D materials [115, 158]. However, one has to pay attention to the sample drift caused by the thermal instability, where fast acquiring technique is also necessary to overcome the severe sample drift.

Besides contanmination, structural damage from high-energy electrons is another significant issue in (S)TEM characterizations of 2D material. Reconstruction can occur rapidly in unstable structures (defects or edges) in 2D materials during the bombardment of the electrons. For instance, edges in 2D materials are the dominant structures that can substantially modify the property of the 2D matrix. Probing the intrinsic properties of edges serves as an important way to reveal their functionality. However, the unsaturated bonding in the edge regions (also in other unstable structures) makes them “fragile” to the incoming electrons, where reconstructions can easily happen as compared to the atoms in the bulk material. One has to be cautionous on whether the edge or defect structures that

observed are induced by electron irradiation. Graphene sandwich structure may serve as a universal solution for those beam-sensitive 2D materials, such as TMDC monolayers, black phosphorus, GaS, etc. Indeed, a recent research has shown that a monolayer MoS2 sandwiched by two piece of graphene reduce the damage from the electrons substantially, making atom-resovled EEL spectrum become possible [149].

Due to the atomic thickness, the dominant damage mechanism varies depending on the properties of the materials. For instance, knock-on damage is the major damge mechanism in pristine graphene, thus the lower the acceleration voltage, the less damage from the electrons. Chemical assisted etching may also play an important role in graphene oxide or some dirty region of graphene. In contrast, ionization damge plays an important role in TMDC materials. Therefore a moderate voltage that below the knock-on threshold of the imaged species with low-dose imaging setting can minimize the damage induced by the electrons. In fact, graphene and TMDC monolayers are the only 2D materials that has been well-studied. The damge mechanism in most emerging 2D materials, such as black phorphate and 2D GaS or GaSe, is still elusive. Although these electron-induced damage can sometimes be useful in investigating the dynamical behaviors of the crytalline structure, such damage should be minimized or even avoided in structural characterizations, especially in some dedicated experiments in 2D materials, such as atomic tomography, ptychography and *in-situ* experiment which requires a stable material systems. For future study on other type of 2D materials, investigation of the damage mechanism should be the first step in order to find out a proper experimental setting to minimize the damage.

The future research direction in 2D materials, in my opinion, is to directly visualize the link between the atomic structure and properties, which requires *in-situ* measuring capability with atomic resolution inside the microscope. To realize atomic *in-situ* measurements in 2D materials, the above mentioned challengings, i.e., high quality sample with clean surface and minimization of electron-induced damage, are the foundations to such kind of experiments, since we need to exclude the contribution from the electron beam over the entire period of the experiment.

Previous effort focus on developing high-acceleration voltage in transmission electron microscope, since it provides electrons with shorter wavelength and higher kinetic energy, which effectively leads to higher spatial resolution and larger penetration depth of the electrons. Such strategy may need to divert owing to the atomic thickness of 2D materials, where electrons can still penetrate the thin atomic layers even at very low acceleration voltage while minimizing the damage to the beam-sensitive structures.

Low-dose and lose-voltage imaging in STEM are two promising techniques to reduce the damage from electrons in 2D materials. Furthermore, the interplay of the two techniques can also expand our ability to probe the intrinsic property of beam-sensitive structures in 2D material and may provide a universal solution for all 2D materials to avoid irradiation damage. Random sampling of the structure is one way to achieve low-dose imaging, which can be realized by software algorithms that change the scanning behavior of the electron beam. However, one has always to be cationous about the artifacts that can be easily introduced in the reconstructed images based on random sampling. Moreover, random sampling may only work on periodic structures.

On the other side, low-voltage imaging is more likely to be a hardware problem which requires a new design of the electronic optics inside the microscope. Advanced correctors which correct spherical and chromatic aberration may also needed for low-voltage (S)TEM to reach sufficient spatial resolution. Moreover, these "slow" electrons accelerated under lower voltage would have less impacting distant within the sample, resulting in a decreased delocalization. Such reduced delocalization may also benefit for the spatially resovled EELS mapping in low loss energy region.

The ultimate goal is *in-situ* observations of the structure-property correlations with atomic sensitivity. Atomic resolution imaging has become a routine method for material characterizations owing to the commercialization of aberration correctors. Many physical phenomenon can now be correlated with their atomic structures. Nevertheless, materials are interacting with the environment rather than isolating on their own for applications in reality. Little is known on the dynamical process that happens inside the materials when working under their real working environments, especially at the atomic scale. It may be hard to achieve atomic-scale real-time *in-situ* observations of these dynamical process in 3D bulk materials due to the instability caused by the external excitations and insufficient depth resolution. 2D materials provide an exceptional platform for *in-situ* experiments. It is possible to achieve atomic resolution *in-situ* microscopy in 2D materials because of the reduced dimension of the material, where all dynamical movements are confined in a 2D plane during the excitations. Indeed, the *in-situ* electrical measurement of the nanowire carried out by our collaborator has already demonstrated atomic resolution *in-situ* microscopy in TEM [111]. To achieve higher spatial resolution and direct interpretable imaging during the *in-situ* experiments, developing the *in-situ* measuring capacity in

STEM is the promising way to fulfill the goal. A possible and feasible demonstration of atomic *in-situ* microscopy in STEM may be achieved by monitoring the structural evolution of TMDC monolayers when connecting to electrical current. Making contacts to the sample on a conventional TEM grid is the first step, which requires development of the traditional technique in making contacts, including electron lithography, metal deposition and lift-off process, that is compatible with a TEM grid. Moreover, electron irradiation effect on the sample should also be excluded, which can be achieved by using the graphene sandwich scheme mentioned above. Investigations focus on the real-time dynamical structural evolutions when the 2D materials are connected to external excitations, will yield unambiguous understandings for their electrical, optical and catalytic properties in their real working conditions.

REFERENCES

1. Hohenberg, P. and W. Kohn, *Inhomogeneous Electron Gas.* Physical Review, 1964. **136**(3B): p. B864-B871.
2. Kohn, W. and L.J. Sham, *Self-Consistent Equations Including Exchange and Correlation Effects.* Physical Review, 1965. **140**(4A): p. A1133-A1138.
3. Payne, M.C., et al., *Iterative minimization techniques for \textit{ab initio} total-energy calculations: molecular dynamics and conjugate gradients.* Reviews of Modern Physics, 1992. **64**(4): p. 1045-1097.
4. Diebold, U., *The surface science of titanium dioxide.* Surface Science Reports, 2003. **48**(5-8): p. 53-229.
5. Sun, Y.G. and Y.N. Xia, *Shape-controlled synthesis of gold and silver nanoparticles.* Science, 2002. **298**(5601): p. 2176-2179.
6. Egerton, R.F., P. Li, and M. Malac, *Radiation damage in the TEM and SEM.* Micron, 2004. **35**(6): p. 399-409.
7. Pennycook, S.J. and D.E. Jesson, *HIGH-RESOLUTION Z-CONTRAST IMAGING OF CRYSTALS.* Ultramicroscopy, 1991. **37**(1-4): p. 14-38.
8. Crewe, A.V., J. Wall, and J. Langmore, *Visibility of Single Atoms.* Science, 1970. **168**(3937): p. 1338-1340.
9. Krivanek, O.L., N. Dellby, and A.R. Lupini, *Towards sub-Å electron beams.* Ultramicroscopy, 1999. **78**(1–4): p. 1-11.
10. Batson, P.E., N. Dellby, and O.L. Krivanek, *Sub-angstrom resolution using aberration corrected electron optics.* Nature, 2002. **418**(6898): p. 617-620.
11. Kohn, W., *Nobel Lecture: Electronic structure of matter\char22{}wave functions and density functionals.* Reviews of Modern Physics, 1999. **71**(5): p. 1253-1266.
12. Crewe, A.V., M. Isaacson, and D. Johnson, *A Simple Scanning Electron Microscope.* Review of Scientific Instruments, 1969. **40**(2): p. 241-246.
13. Williams, D.B.C., C. B, *Transmission Electron Microscopy: A Textbook for Materials Science. Vol. 2nd (Springer, 2009)*2009.
14. Stemmer, S., *International Summer School on "Semiconductor Interfaces"*, 2014.
15. Zurich, E. *Elastic Scattering of Electrons by Atoms*. 2010; Available from: http://www.microscopy.ethz.ch/elast.htm.
16. Bragg, W.H. and W.L. Bragg, *The Reflection of X-rays by Crystals*. Vol. 88. 1913. 428-438.
17. Cowley, J.M., *Diffraction physics*1975, North-Holland, Amsterdam: North-Holland, Amsterdam.

18. Pennycook, S.J. and P.D. Nellist, *Scanning Transmission Electron Microscopy*, ed. S.J. Pennycook and P.D. Nellist2010: Springer.

19. Cowley, J.M., *Image contrast in a transmission scanning electron microscope.* Appl. Phys. Lett., 1969. **15**: p. 58-59.

20. Zeitler, E. and M.G.R. Thomson, *Scanning transmission electron microscopy.* Optik, 1970. **31**: p. 258-280 and 359-366.

21. Ade, G., *On the incoherent imaging in the scanning transmission electron microscope.* Optik, 1977. **49**: p. 113-116.

22. Treacy, M.M.J., A. Howie, and C.J. Wilson, *Z contrast imaging of platinum and palladium catalysts.* Philos. Mag. A, 1978. **38**: p. 569-585.

23. Nellist, P.D. and S.J. Pennycook, *The principles and interpretation of annular dark-field Z-contrast imaging.* Adv. Imag. Electron Phys., 2000. **113**: p. 148-203.

24. Hartel, P., H. Rose, and C. Dinges, *Conditions and reasons for incoherent imaging in STEM.* Ultramicroscopy, 1996. **63**(2): p. 93-114.

25. Wang, Z.L., *Elastic and Inelastic Scattering in Electron Diffraction and Imaging*, ed. Z.L. Wang1995: Plenum Press.

26. Colliex, C., et al., *Contribution of electron energy loss spectroscopy to the development of analytical electron microscopy.* Ultramicroscopy, 1976. **1**(3–4): p. 301-315.

27. Pennycook, T.J., *DENSITY FUNCTIONAL THEORY AND SCANNING TRANSMISSION ELECTRON MICROSCOPY: SYNERGISTIC TOOLS FOR MATERIALS INVESTIGATION*, in *Physics and Astronomy*2012, Vanderbilt University. p. 126.

28. Nellist, P.D., et al., *Direct Sub-Angstrom Imaging of a Crystal Lattice.* Science, 2004. **305**(5691): p. 1741.

29. Ronchi, V., *Forty Years of History of a Grating Interferometer.* Applied Optics, 1964. **3**(4): p. 437-451.

30. Muller, D. and P. Batson. *Lecture notes on the practical details of STEM imaging*. 2006; Available from: http://muller.research.engineering.cornell.edu/sites/WEELS/summer06/index.html.

31. Scherzer, O., *The theoretical resolution limit of the electron microscope.* J. Appl. Phys., 1949. **20**: p. 20-29.

32. Kirkland, E.J., *Advanced Computing in Electron Microscopy*2010: Springer.

33. Zemlin, F., *A practical procedure for alignment of a high resolution electron microscope.* Ultramicroscopy, 1979. **4**(2): p. 241-245.

34. Lin, J.A. and J.M. Cowley, *Calibration of the operating parameters for an HB5 stem instrument.* Ultramicroscopy, 1986. **19**(1): p. 31-42.

35. James, E.M. and N.D. Browning, *Practical aspects of atomic resolution imaging and analysis in STEM.* Ultramicroscopy, 1999. **78**(1–4): p. 125-139.

36. Batson, P.E., *Simultaneous STEM imaging and electron energy-loss spectroscopy with atomic-column sensitivity*. Nature, 1993. **366**(6457): p. 727-728.

37. Browning, N.D., M.F. Chisholm, and S.J. Pennycook, *Atomic-resolution chemical analysis using a scanning transmission electron microscope.* Nature, 1993. **366**(6451): p. 143-146.

38. !!! INVALID CITATION !!!

39. Dirac, P.A.M., *The Principles of Quantum Mechanics (4th ed.).*1958: Oxford University Press.

40. Hafner, J., *Ab-initio simulations of materials using VASP: Density-functional theory and beyond.* Journal of Computational Chemistry, 2008. **29**(13): p. 2044-2078.

41. Martin, R.M., *Electronic Structure: Basic Theory and Practical Methods*2004: Cambridge University Press, Cambridge.

42. Himmetoglu, B., et al., *Hubbard-corrected DFT energy functionals: The LDA+U description of correlated systems.* International Journal of Quantum Chemistry, 2014. **114**(1): p. 14-49.

43. Marini, A., G. Onida, and R. Del Sole, *Quasiparticle Electronic Structure of Copper in the GW Approximation.* Physical Review Letters, 2001. **88**(1): p. 016403.

44. Phillips, J.C., *Energy-Band Interpolation Scheme Based on a Pseudopotential.* Physical Review, 1958. **112**(3): p. 685-695.

45. Geim, A.K. and I.V. Grigorieva, *Van der Waals Heterostructures.* Nature, 2013. **499**(7459): p. 419-425.

46. Novoselov, K.S., et al., *Electric field effect in atomically thin carbon films.* Science, 2004. **306**(5696): p. 666-669.

47. Wallace, P.R., *The Band Theory of Graphite.* Physical Review, 1947. **71**(9): p. 622-634.

48. McClure, J.W., *Band Structure of Graphite and de Haas-van Alphen Effect.* Physical Review, 1957. **108**(3): p. 612-618.

49. Slonczewski, J.C. and P.R. Weiss, *Band Structure of Graphite.* Physical Review, 1958. **109**(2): p. 272-279.

50. Castro Neto, A.H., et al., *The electronic properties of graphene.* Reviews of Modern Physics, 2009. **81**(1): p. 109-162.

51. Bolotin, K.I., et al., *Ultrahigh electron mobility in suspended graphene.* Solid State Communications, 2008. **146**(9–10): p. 351-355.

52. Guinea, F., A.H. Castro Neto, and N.M.R. Peres, *Electronic states and Landau levels in graphene stacks.* Physical Review B, 2006. **73**(24): p. 245426.

53. Perera, M.M., et al., *Improved Carrier Mobility in Few-Layer MoS2 Field-Effect Transistors with Ionic-Liquid Gating.* Acs Nano, 2013. **7**(5): p. 4449-4458.

54. Pu, J., et al., *Highly Flexible MoS2 Thin-Film Transistors with Ion Gel Dielectrics.* Nano Lett, 2012. **12**(8): p. 4013-4017.

55. Korn, T., et al., *Low-temperature photocarrier dynamics in monolayer MoS2.* Applied Physics Letters, 2011. **99**(10): p. -.

56. Mak, K.F., et al., *Atomically thin MoS_2: a new direct-gap semiconductor.* Physical Review Letters, 2010. **105**(13).

57. Kam, K.K. and B.A. Parkinson, *Detailed photocurrent spectroscopy of the semiconducting group VIB transition metal dichalcogenides.* The Journal of Physical Chemistry, 1982. **86**(4): p. 463-467.

58. Splendiani, A., et al., *Emerging Photoluminescence in Monolayer MoS2.* Nano Lett, 2010. **10**(4): p. 1271-1275.

59. Radisavljevic, B., et al., *Single-layer MoS2 transistors.* Nature Nanotechnology, 2011. **6**(3): p. 147-150.

60. Lopez-Sanchez, O., et al., *Ultrasensitive photodetectors based on monolayer MoS2.* Nature Nanotechnology, 2013. **8**(7): p. 497-501.

61. Zeng, H., et al., *Valley polarization in MoS2 monolayers by optical pumping.* Nat Nano, 2012. **7**(8): p. 490-493.

62. Castro, E.V., et al., *Biased bilayer graphene: Semiconductor with a gap tunable by the electric field effect.* Physical Review Letters, 2007. **99**(21).

63. Zhang, Y., et al., *Direct observation of a widely tunable bandgap in bilayer graphene.* Nature, 2009. **459**(7248): p. 820-823.

64. Tian, J., et al., *Direct Imaging of Graphene Edges: Atomic Structure and Electronic Scattering.* Nano Letters, 2011. **11**(9): p. 3663-3668.

65. Yazyev, O.V. and S.G. Louie, *Electronic transport in polycrystalline graphene.* Nat Mater, 2010. **9**(10): p. 806-809.

66. Yu, Q., et al., *Control and characterization of individual grains and grain boundaries in graphene grown by chemical vapour deposition.* Nat Mater, 2011. **10**(6): p. 443-449.

67. Tsen, A.W., et al., *Tailoring Electrical Transport Across Grain Boundaries in Polycrystalline Graphene.* Science, 2012. **336**(6085): p. 1143-1146.

68. Hibino, H., et al., *Stacking domains of epitaxial few-layer graphene on SiC(0001).* Physical Review B, 2009. **80**(8).

69. Liu, L., et al., *High-Yield Chemical Vapor Deposition Growth of High-Quality Large-Area AB-Stacked Bilayer Graphene.* Acs Nano, 2012. **6**(9): p. 8241-8249.

70. Park, H.J., et al., *Growth and properties of few-layer graphene prepared by chemical vapor deposition.* Carbon, 2010. **48**(4): p. 1088-1094.

71. Fang, W., et al., *Rapid Identification of Stacking Orientation in Isotopically Labeled Chemical-Vapor Grown Bilayer Graphene by Raman Spectroscopy.* Nano Letters, 2013. **13**(4): p. 1541-1548.

72. Krivanek, O.L., et al., *Atom-by-atom structural and chemical analysis by annular dark-field electron microscopy.* Nature, 2010. **464**(7288): p. 571-574.

73. Newaz, A.K.M., et al., *Probing charge scattering mechanisms in suspended graphene by varying its dielectric environment.* Nature Communications, 2012. **3**.

74. Guinea, F., M.I. Katsnelson, and A.K. Geim, *Energy gaps and a zero-field quantum Hall effect in graphene by strain engineering.* Nature Physics, 2010. **6**(1): p. 30-33.

75. Pereira, V.M. and A.H.C. Neto, *Strain Engineering of Graphene's Electronic Structure.* Physical Review Letters, 2009. **103**(4).

76. Kroemer, H., *Heterostructure bipolar-transistors and integrated-circuits.* Proceedings of the Ieee, 1982. **70**(1): p. 13-25.

77. Ohno, Y., et al., *Electrical spin injection in a ferromagnetic semiconductor heterostructure.* Nature, 1999. **402**(6763): p. 790-792.

78. Novoselov, K.S., et al., *Two-dimensional gas of massless Dirac fermions in graphene.* Nature, 2005. **438**(7065): p. 197-200.

79. Dean, C.R., et al., *Boron nitride substrates for high-quality graphene electronics.* Nature Nanotechnology, 2010. **5**(10): p. 722-726.

80. Song, L., et al., *Large scale growth and characterization of atomic hexagonal boron nitride layers.* Nano Letters, 2010. **10**(8): p. 3209-3215.

81. Gutierrez, H.R., et al., *Extraordinary room-temperature photoluminescence in triangular WS_2 monolayers.* Nano Letters, 2013. **13**(8): p. 3447-3454.

82. Najmaei, S., et al., *Vapour phase growth and grain boundary structure of molybdenum disulphide atomic layers.* Nat Mater, 2013.

83. van der Zande, A.M., et al., *Grains and grain boundaries in highly crystalline monolayer molybdenum disulphide.* Nature Materials, 2013. **12**(6): p. 554-561.

84. Britnell, L., et al., *Field-effect tunneling transistor based on vertical graphene heterostructures.* Science, 2012. **335**(6071): p. 947-950.

85. Gannett, W., et al., *Boron nitride substrates for high mobility chemical vapor deposited graphene.* Applied Physics Letters, 2011. **98**(24).

86. Georgiou, T., et al., *Vertical field-effect transistor based on graphene-WS_2 heterostructures for flexible and transparent electronics.* Nature Nanotechnology, 2013. **8**(2): p. 100-103.

87. Yu, W.J., et al., *Highly efficient gate-tunable photocurrent generation in vertical heterostructures of layered materials.* Nature Nanotechnology, 2013. **8**(12): p. 952-958.

88. Pospischil, A., M.M. Furchi, and T. Mueller, *Solar-energy conversion and light emission in an atomic monolayer p-n diode.* Nature Nanotechnology, 2014. **9**(4): p. 257-261.

89. Baugher, B.W., et al., *Optoelectronic devices based on electrically tunable p-n diodes in a monolayer dichalcogenide.* Nature Nanotechnology, 2014. **9**(4): p. 262-267.

90. Ross, J.S., et al., *Electrically tunable excitonic light-emitting diodes based on monolayer WSe2 p-n junctions.* Nature Nanotechnology, 2014. **9**(4): p. 268-272.

91. Haigh, S.J., et al., *Cross-sectional imaging of individual layers and buried interfaces of graphene-based heterostructures and superlattices.* Nature Materials, 2012. **11**(9): p. 764-767.

92. Yang, W., et al., *Epitaxial growth of single-domain graphene on hexagonal boron nitride.* Nature Materials, 2013. **12**(9): p. 792-797.

93. Levendorf, M.P., et al., *Graphene and boron nitride lateral heterostructures for atomically thin circuitry.* Nature, 2012. **488**(7413): p. 627-632.

94. Liu, L., et al., *Heteroepitaxial growth of two-dimensional hexagonal boron nitride templated by graphene edges.* Science, 2014. **343**(6167): p. 163-167.

95. Liu, Z., et al., *In-plane heterostructures of graphene and hexagonal boron nitride with controlled domain sizes.* Nature Nanotechnology, 2013. **8**(2): p. 119-124.

96. Miyata, Y., et al., *Fabrication and characterization of graphene/hexagonal boron nitride hybrid sheets.* Applied Physics Express, 2012. **5**(8).

97. Okamoto, H., *Tellurium-Tungsten Binary Diagram.* ASM Alloy Phase Diagrams Center, P. Villars, editor-in-chief; H. Okamoto and K. Cenzual, section editors; http://www1.asminternational.org/AsmEnterprise/APD,, 1900.

98. Zhou, W., et al., *Intrinsic structural defects in monolayer molybdenum disulfide.* Nano Lett, 2013. **13**(6): p. 2615-22.

99. Gong, Y.J., et al., *Band gap engineering and layer-by-layer mapping of selenium-doped molybdenum disulfide.* Nano Letters, 2014. **14**(2): p. 442-449.

100. Gong, Y., et al., *Band gap engineering and layer-by-layer mapping of selenium-doped molybdenum disulfide.* Nano Lett, 2013.

101. Zhao, W.J., et al., *Evolution of electronic structure in atomically thin sheets of WS_2 and WSe_2.* Acs Nano, 2013. **7**(1): p. 791-797.

102. Berkdemir, A., et al., *Identification of individual and few layers of WS_2 using Raman spectroscopy.* Scientific Reports, 2013. **3**.

103. Kosmider, K. and J. Fernandez-Rossier, *Electronic properties of the MoS_2-WS_2 heterojunction.* Physical Review B, 2013. **87**(7).

104. Peimyoo, N., et al., *Nonblinking, Intense two-dimensional light emitter: monolayer WS_2 triangles.* Acs Nano, 2013. **7**(12): p. 10985-10994.

105. Wang, Z., et al., *Mixed low-dimensional nanomaterial: 2D ultranarrow MoS_2 inorganic nanoribbons encapsulated in quasi-1D carbon nanotubes.* Journal of the American Chemical Society, 2010. **132**(39): p. 13840-13847.

106. Delaney, K.T., N.A. Spaldin, and C.G. Van de Walle, *Theoretical study of Schottky-barrier formation at epitaxial rare-earth-metal/semiconductor interfaces.* Physical Review B, 2010. **81**(16): p. 165312.

107. Kang, J., et al., *Band offsets and heterostructures of two-dimensional semiconductors.* Applied Physics Letters, 2013. **102**(1): p. -.

108. Mak, K.F., et al., *Atomically Thin MoS_2: A New Direct-Gap Semiconductor.* Phys. Rev. Lett., 2010. **105**(13): p. 136805.

109. Radisavljevic, B., M.B. Whitwick, and A. Kis, *Integrated Circuits and Logic Operations Based on Single-Layer MoS_2.* Acs Nano, 2011. **5**(12): p. 9934-9938.

110. Splendiani, A., et al., *Emerging Photoluminescence in Monolayer MoS_2.* Nano Lett., 2010. **10**(4): p. 1271-1275.

111. Lin, J., et al., *Flexible metallic nanowires with self-adaptive contacts to semiconducting transition-metal dichalcogenide monolayers.* Nat Nano, 2014. **9**(6): p. 436-442.

112. Najmaei, S., et al., *Vapour Phase Growth and Grain Boundary Structure of Molybdenum Disulphide Atomic Layers.* Nat. Mater., 2013. **12**(8): p. 754-759.

113. van der Zande, A.M., et al., *Grains and Grain Boundaries in Highly Crystalline Monolayer Molybdenum Disulphide.* Nat. Mater., 2013. **12**(6): p. 554-561.

114. Najmaei, S., et al., *Electrical Transport Properties of Polycrystalline Monolayer Molybdenum Disulfide.* Acs Nano, 2014. **8**(8): p. 7930-7937.

115. Lin, Y.-C., et al., *Atomic Mechanism of the Semiconducting-To-Metallic Phase Transition in Single-Layered MoS_2.* Nat. Nanotechnol., 2014. **9**(5): p. 391-396.

116. Kan, M., et al., *Structures and Phase Transition of a MoS_2 Monolayer.* The Journal of Physical Chemistry C, 2014. **118**(3): p. 1515-1522.

117. Lee, J., et al., *Direct Visualization of Reversible Dynamics in a Si_6 Cluster Embedded in a Graphene Pore.* Nat. Commun., 2013. **4**: p. 1650.

118. Susi, T., et al., *Silicon-Carbon Bond Inversions Driven by 60-keV Electrons in Graphene.* Phys. Rev. Lett., 2014. **113**(11): p. 115501.

119. Komsa, H.-P., et al., *Two-Dimensional Transition Metal Dichalcogenides under Electron Irradiation: Defect Production and Doping.* Phys. Rev. Lett., 2012. **109**(3): p. 035503.

120. Cretu, O., et al., *Migration and Localization of Metal Atoms on Strained Graphene.* Phys. Rev. Lett., 2010. **105**(19): p. 196102.

121. Kotakoski, J., et al., *From Point Defects in Graphene to Two-Dimensional Amorphous Carbon.* Phys. Rev. Lett., 2011. **106**(10): p. 105505.

122. Cretu, O., et al., *Experimental Observation of Boron Nitride Chains.* Acs Nano, 2014. **8**(12): p. 11950-11957.

123. Girit, Ç.Ö., et al., *Graphene at the Edge: Stability and Dynamics.* Science, 2009. **323**(5922): p. 1705-1708.

124. Chen, J.H., et al., *Controlled Growth of a Line Defect in Graphene and Implications for Gate-Tunable Valley Filtering.* Physical Review B, 2014. **89**(12): p. 121407.

125. Zou, X. and B.I. Yakobson, *An Open Canvas—2D Materials with Defects, Disorder, and Functionality.* Accounts of Chemical Research, 2015. **48**(1): p. 73-80.

126. Liu, H., et al., *Dense Network of One-Dimensional Midgap Metallic Modes in Monolayer $MoSe_2$ and Their Spatial Undulations.* Phys. Rev. Lett., 2014. **113**(6): p. 066105.

127. Najmaei, S., et al., *Vapour phase growth and grain boundary structure of molybdenum disulphide atomic layers.* Nat Mater, 2013. **12**(8): p. 754-759.

128. Lin, J., et al., *Flexible Metallic Nanowires with Self-Adaptive Contacts to Semiconducting Transition-Metal Dichalcogenide Monolayers.* Nat. Nanotechnol., 2014. **9**(6): p. 436-442.

129. Komsa, H.-P., et al., *From Point to Extended Defects in Two-Dimensional MoS_2: Evolution of Atomic Structure under Electron Irradiation.* Physical Review B, 2013. **88**(3): p. 035301.

130. Kotakoski, J., C. Mangler, and J.C. Meyer, *Imaging Atomic-Level Random Walk of a Point Defect in Graphene.* Nat. Commun., 2014. **5**: p. 3991.

131. Azizi, A., et al., *Dislocation Motion and Grain Boundary Migration in Two-Dimensional Tungsten Disulphide.* Nat. Commun., 2014. **5**: p. 4867.

132. Hong, J., et al., *Exploring Atomic Defects in Molybdenum Disulphide Monolayers.* Nat. Commun., 2015. **6**: p. 6293.

133. Yuan, S., et al., *Effect of Point Defects on the Optical and Transport Properties of MoS_2 and WS_2.* Physical Review B, 2014. **90**(4): p. 041402.

134. Qiu, H., et al., *Hopping Transport through Defect-induced Localized States in Molybdenum Disulphide.* Nat. Commun., 2013. **4**: p. 2642.

135. Kondo, Y. and K. Takayanagi, *Synthesis and characterization of helical multi-shell gold nanowires.* Science, 2000. **289**(5479): p. 606-608.

136. Qin, L.C., et al., *Materials science - The smallest carbon nanotube.* Nature, 2000. **408**(6808): p. 50-50.

137. Xiang, J., et al., *Ge/Si nanowire heterostructures as high-performance field-effect transistors.* Nature, 2006. **441**(7092): p. 489-493.

138. Yanson, A.I., et al., *Formation and manipulation of a metallic wire of single gold atoms.* Nature, 1998. **395**(6704): p. 783-785.

139. Ohnishi, H., Y. Kondo, and K. Takayanagi, *Quantized conductance through individual rows of suspended gold atoms.* Nature, 1998. **395**(6704): p. 780-783.

140. Wang, Q.H., et al., *Electronics and optoelectronics of two-dimensional transition metal dichalcogenides.* Nature Nanotechnology, 2012. **7**(11): p. 699-712.

141. Yin, Z., et al., *Single-Layer MoS2 Phototransistors.* Acs Nano, 2012. **6**(1): p. 74-80.

142. Cakir, D., et al., *First principles study of electronic and mechanical properties of molybdenum selenide type nanowires.* Physical Review B, 2006. **74**(23): p. 235433.

143. Murugan, P., et al., *Assembling nanowires from Mo-S clusters and effects of iodine doping on electronic structure.* Nano Letters, 2007. **7**(8): p. 2214-2219.

144. Kibsgaard, J., et al., *Atomic-scale structure of Mo_6S_6 nanowires.* Nano Letters, 2008. **8**(11): p. 3928-3931.

145. Venkataraman, L., Y.S. Hong, and P. Kim, *Electron transport in a multichannel one-dimensional conductor: Molybdenum selenide nanowires.* Physical Review Letters, 2006. **96**(7): p. 076601.

146. Venkataraman, L. and C.M. Lieber, *Molybdenum selenide molecular wires as one-dimensional conductors.* Physical Review Letters, 1999. **83**(25): p. 5334-5337.

147. Liu, X., et al., *Top down fabrication of sub-nanometre semiconducting nanoribbons derived from molybdenum disulfide sheets.* Nat Commun, 2013. **4**: p. 1776.

148. Zhou, W., et al., *Intrinsic structural defects in monolayer molybdenum disulfide.* Nano Lett, 2013. **13**: p. 2615-2522.

149. Zan, R., et al., *Control of Radiation Damage in MoS2 by Graphene Encapsulation.* Acs Nano, 2013. **7**(11): p. 10167-10174.

150. Komsa, H.-P., et al., *Two-Dimensional Transition Metal Dichalcogenides under Electron Irradiation: Defect Production and Doping.* Physical Review Letters, 2012. **109**(3): p. 035503.

151. Popov, I., et al., *Electromechanical switch based on Mo_6S_6 nanowires.* Nano Letters, 2008. **8**(12): p. 4093-4097.

152. Lee, J., et al., *Direct visualization of reversible dynamics in a Si_6 cluster embedded in a graphene pore.* Nat Commun, 2013. **4**: p. 1650.

153. Chau, R., et al., *Integrated nanoelectronics for the future.* Nature Materials, 2007. **6**(11): p. 810-812.

154. Regan, W., et al., *A direct transfer of layer-area graphene.* Applied Physics Letters, 2010. **96**(11).

155. Krivanek, O.L., et al., *An electron microscope for the aberration-corrected era.* Ultramicroscopy, 2008. **108**(3): p. 179-195.

156. Svensson, K., et al., *Compact design of a transmission electron microscope-scanning tunneling microscope holder with three-dimensional coarse motion.* Review of Scientific Instruments, 2003. **74**(11): p. 4945-4947.

157. Ren, B., G. Picardi, and B. Pettinger, *Preparation of gold tips suitable for tip-enhanced Raman spectroscopy and light emission by electrochemical etching.* Review of Scientific Instruments, 2004. **75**(4): p. 837-841.

158. Liu, Z., et al., *In situ observation of step-edge in-plane growth of graphene in a STEM.* Nat Commun, 2014. **5**.